AMERICAN UNIVERSITY OF BEIRUT

A NUMERICAL AND EXPERIMENTAL METHODOLOGY
FOR OVERCOMING CHALLENGES ARISING FROM
FRICTION STIR WELDING OF DISSIMILAR METALS

by

ZEINA GHASSAN EL CHLOUK

A thesis
submitted in partial fulfillment of the requirements
for the degree of Doctor of Philosophy
to the Department of Mechanical Engineering
of the Maroun Semaan Faculty of Engineering and Architecture
at the American University of Beirut
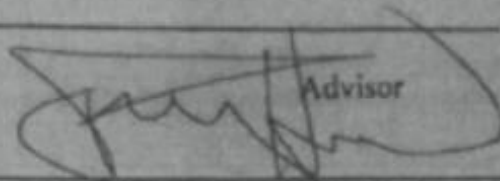
Beirut, Lebanon
November 2020

AMERICAN UNIVERSITY OF BEIRUT

A NUMERICAL AND EXPERIMENTAL METHODOLOGY FOR OVERCOMING CHALLENGES ARISING FROM FRICTION STIR WELDING OF DISSIMILAR METALS
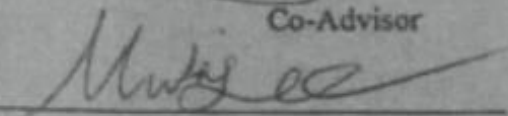
by
ZEINA GHASSAN EL CHLOUK

Approved by:
Signatures

Dr. Ramsey Hamade, Professor
Mechanical Engineering Department, AUB   Advisor
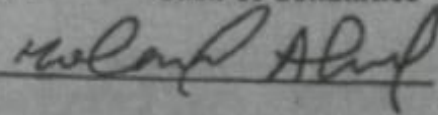
Dr. Mutasem Shehadeh, Associate Professor
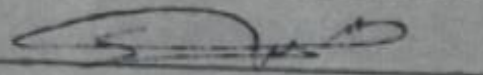Mechanical Engineering Department, AUB   Co-Advisor

Dr. Mohammad Ahmad, Professor
Chemical and Petroleum Engineering Department, AUB   Chair of Committee
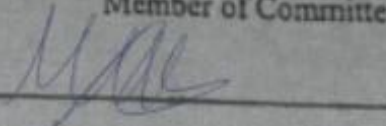
Dr. Samir Mustapha, Assistant professor
Mechanical Engineering Department, AUB   Member of Committee

Dr. Michel Kazan, Associate Professor
Physics Department, AUB   Member of Committee
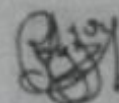
Dr. Ghassan Kridli, Professor
Industrial and Manufacturing Systems Engineering   Member of Committee
University of Michigan-Dearborn

Dr. Georges Ayoub, Assistant Professor
Industrial and Manufacturing Systems Engineering   Member of Committee
University of Michigan-Dearborn

Date of thesis/dissertation defense: November 23, 2020

AMERICAN UNIVERSITY OF BEIRUT

DISSERTATION RELEASE FORM

Student Name: ___EL CHLOUK_____Zeina_____ __Ghassan_____
                             Last   First   Middle

I authorize the American University of Beirut, to: (a) reproduce hard or electronic copies of my dissertation; (b) include such copies in the archives and digital repositories of the University; and (c) make freely available such copies to third parties for research or educational purposes:

☐ As of the date of submission

☐ One year from the date of submission of my dissertation.

☒ Two years from the date of submission of my dissertation.

☐ Three years from the date of submission of my dissertation.

December 28, 2020

Signature   Date

ACKNOWLEDGMENTS

AN ABSTRACT OF THE THESIS OF

Name: Zeina Ghassan El Chlouk   for   Doctor of Philosophy
                                                    Major: Mechanical Engineering

Title: A numerical and experimental methodology for overcoming challenges arising from friction stir welding of dissimilar metals

Friction stir welding is a rather recent solid state welding technique which presents several advantages over conventional fusion welding techniques. Different aspects of this process are thoroughly investigated in this work; experimentally the effect of the several process parameters on the resultant joint quality and strength is analyzed and it was found that placing the softer material in the advancing side could result in better mixing between the two sides. Additionally, intermetallic compounds were detected at the abutting interface between dissimilar materials through SEM/EDX analysis. The increase in the quantity of these intermetallic compounds is found to decrease the strength of the joints drastically.

Moreover, this process was reproduced using finite elements modelling software Deform in efforts to save long and costly experiments and measure state variables in the bulk of the welded nugget. Temperature profiles at specific points in the system are compared between the experiments and the ones resulting from the FEM. After testing several friction coefficients, a best fit was chosen in order to minimize the error between the maximum temperature measured at these specific points. Additionally, the volume fraction of the welded interface also compared favorably to the experimental volume fraction as obtained from EDX/SEM. Improvements to the results of the proposed model can be achieved by changing the flow stress models of the materials or by finding answers to allow the solution of the simulation to converge when the workpiece is modelled as two separate entities (each representing one material) or eventually by creating a user-sub routine that includes the temperature-time transformation plots to better reproduce the resultant structure between the dissimilar materials.

In an effort to understand the mechanisms that guides the deformation mechanism at an incoherent interface, molecular dynamics simulations are conducted using LAMMPS. In the first simulations, a pristine Al/Fe interface was created and compressed at constant strain rate of $5.10^7 s^{-1}$. A remarkable mixing was found at the advanced stages of the simulations, at temperatures starting as low at 150K and going up to 900K. The RDF suggests that the created intermetallic compound has the structure of AlFe also known as the CsCl crystalline structure. In other simulations, different strain rates were tested and the nucleation of dislocations was observed across the incoherent interface. It was noticed that the first dislocations appeared in the bulk of the aluminum region. After that the dislocations pile up at the interface from the aluminum region and thus constitute a favorable nucleation site for the dislocations in the iron region. Two yield points were discerned on the stress strain plots at different temperatures corresponding

to the nucleation of dislocations in the two regions Al and Fe respectively. The flow and yield stresses were then fitted into thermally activated equations as a function of temperature and strain rates. Finally, the valuable information obtained from these developed simulations were used for comparison in a different loading stress type; this type the mixing and resultant composition of the interface were analyzed following mixing from a nanometric tool rotating and feeding at the Al/Fe interface. Such a process did not yield a variation in the RDF before and after the passage of the tool which could be due to the extremely fast speeds of the tool out of other reasons.

TABLE OF CONTENT

LIST OF ILLUSTRATIONS

9

11

LIST OF TABLES

CHAPTER I

PREAMBLE

The work presented in this manuscript targets the many challenges arising from Friction Stir Welding (FSW) of dissimilar materials. This technique is a rather recent joining process elaborated in the United Kingdom in 1991 and developed later on for similar and dissimilar materials. It presents many advantages over conventional welding methods due to the joining of the materials that occurs, in theory, in solid state. However, it still gives rise to a number of defects in the joints such as cooling cracks and intermetallic compounds (IMC), sometimes formed as precipitates and other times as homogeneous layers. These compounds are thought to contribute to the weakening of the weldment and deteriorating of its mechanical properties. The FSW process is based on a multitude of parameters making it necessary to optimize the combination in order to obtain a reliable weldment. When two different materials are considered, especially when their mechanical and physical properties are largely distinct, the entire set of parameters needs to be re-evaluated and the notion of IMCs taken into account as a main factor to be minimized.

Following a vast literature review in the following chapter of the dissertation, this work addresses, in Chapter I, the issues arising from experimental FSW in the case of dissimilar materials. The parametric study employed in the first stages is presented following which an optimized set of parameters is proposed. The soundest and most reliable Aluminum-Low Carbon steel joints are then mechanically and chemically examined based on their content in IMC and the analysis of the material flow between

the advancing and retreating sides. The scientific limitations often faced during such processes and the time and means consuming experiments redirected the efforts towards simulating FSW using finite elements software such as Deform. This method, detailed in Chapter II of the dissertation, allows an irreplaceable understanding of several variables belonging to the stirred material in the weld line. The importance of this method doesn't come however without its challenges and complications; validating the designed simulation is achieved through comparison of temperature and volume fraction data against experiments. The optimization of the tool to workpiece (WP) friction coefficient yielded improved temperature readings and thus a preliminary model is proposed to reproduce the FSW process using finite element simulations. Ideally, the proposed FE model requires additional adjustments, which could not be achieved through the optimization of the friction coefficient, in order to perfectly fit the experimental data. The adjustments required at this stage must be done to the constitutive equations which govern the response of the WP materials in terms of flow stress with respect to strain, strain rate and temperature. In hopes of developing a constitutive equation that reflects the response of a dissimilar interface under extreme conditions of temperature and strain rate, such as those faced during the FSW process, a Molecular Dynamics (MD) model is pursued. For this, pure Aluminum and pure Iron regions are put together, at a specific orientation, to form a pristine interface, which is subsequently investigated under different loading and surrounding conditions; in Chapter III, the probability of creating an IMC after uniaxial compression of this dissimilar interface is presented and its chemical composition is proposed for a temperature between 150K and 900K and a strain rate of $5*10^7$/s. In Chapter IV, this same interface is loaded again in compression but at a wide range of temperature and

strain rate and flow and yield stress models are estimated based on its mechanical response. During these deformations, the dislocation nucleation and growth are also closely examined and analyzed. Finally, in Chapter V, and based on the preliminary Molecular Dynamics Simulations (MDS), a rigid tool is implemented at the interface between Aluminum and Iron to study the mixing between the dissimilar materials and the eventual resultant structure following the rotating and advancing movement of the tool and to investigate the detailed deformation mechanism at the molecular level under such a mixed loading condition.

This multiscale analysis obtained simultaneously from experiment, from FEM and from MD connects the resultant mechanical properties of the FSW joints to the several reasons behind it at the elemental and atomic scales. The rather low strength of the welded joints is explained in the literature by the presence of brittle IMC and in this work the conditions found in the FSW are reproduced to verify the creation of such compounds. Moreover, the proposed flow stress equation elaborated in MD for the conditions abovementioned, pave new ways for the FEM of the FSW process in Deform software; developing of a new user sub-routine in which this flow stress is implemented as the effective constitutive equation for the WP materials would very likely improve the currently available simulation models. Additional analysis of the IMC can eventually be pursued by producing and characterizing them experimentally and in MD. Once their modelling validated, and their properties theoretically extracted, the prospect of improving the FEM would again rise such that a third phase, namely the IMC, would be taken into account in the simulations as an initially present or a post processed phase of the system.

The research objectives that were answered in this work could be summarized in the following clear and concise points:

- The creation of dissimilar Al/Low carbon steel joints in friction stir welding with a strength of approximately 55% of that of the original material.

- Increasing the speed/feed ratio results in the increasing of intermetallic compounds and thus in the decrease of the joint strength.

- The tapering and threading of the FSW tool results in improved mixing between the welded alloys.

- The FSW process of similar and dissimilar materials was reproduced in a FE simulation under Deform and the temperature profiles as well as the mixing patterns compared favorably to those obtained in experiments.

- AlFe intermetallic compound is identified experimentally following FSW of different types of aluminum alloys to low carbon steel and verified in molecular dynamics simulations of the compression of Al/Fe pristine interface at different temperatures.

- The deformation of the pristine interface first took place in the bulk of the "weaker" material, in the case of Al/Fe it was the aluminum that first yielded. After the first dislocations from the bulk, they migrated to the interface where they accumulated and thus constitute a favorable site to the nucleation of dislocation in Fe which then takes place at the interface.

- Verify the creation of the AlFe intermetallic compound at all tested temperatures going from T=150K to T=900K and different strain rate.

- Investigate two different crystal orientations and visually follow the formation of misfit dislocations for the KS orientation where the atomic spacing

18

difference between the Al and Fe crystals is large. When the Al crystal is reoriented

such that the atomic spacing difference with Fe is reduced to 0.11% misfit dislocations

were not created in the system.

• The flow and yield stresses of the interface system were fitted into thermally

activated equations as a function of temperature and strain rate applicable over a wide

range of these two variables.

CHAPTER II

LITERATURE REVIEW

The fundamental science and underlying physics behind every engineering application offers crucial information to the understanding of the overall macro-scale behavior and the physical and mechanical properties of the materials constituting this process. One such application is FSW, a solid state joining technique based on the friction and heat generated by a tool placed at the faying surfaces of two materials. High levels of plastic deformations at increased strain rates and temperatures induced in this process are thought to be behind the creation of the brittle IMCs which tend to weaken and compromise the integrity the joints. The process of FSW has been extensively investigated in the literature however relating the macro scale strength of the joints and their content in IMCs to the physical basis found at the elemental and molecular levels has not been tackled.

A. THE EXPERIMENTAL APPROACH TO THE FSW PROCESS

FSW, a recent alternative to fusion welding techniques invented in December 1991 at The Welding Institute (TWI) in the UK [1–3], uses a non-consumable probe, more commonly known as the tool, to join two materials using heat generated by friction between the tool and the WP (Fig. 1 [4]). The tool typically constitutes of a pin and a shoulder the geometries of which greatly impact weld quality. The side to which the welding direction and the rotation of the tool are the same (left side in Fig 1) is called the advancing side (AS) and the one where they are opposed (right side on Fig 1) is the retreating side (RS). The heat generated by the movement of the tool and the

friction between the constituents of the system gradually softens the adjacent material which increases flow between the AS and RS. The temperature increase in two sides should in no way surpass their melting temperature, making this welding technique take place in solid state. As the use and need for FSW is increasing in the engineering applications, a better understanding of the underlying scientific ambiguities is becoming more important and crucial.
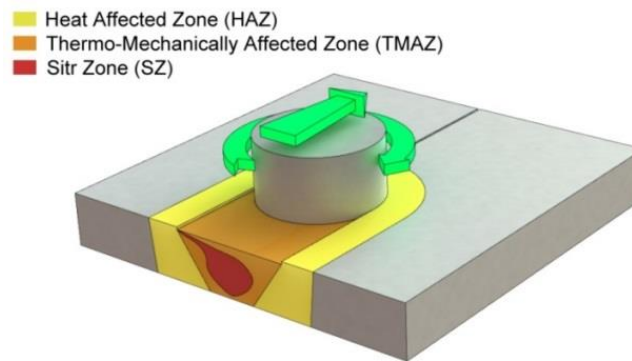
Figure 1 FSW setup illustration [4]

Many studies in the recent years have focused on friction stir welding of similar materials such as aluminum, magnesium or steel. A.H. Ammouri et al.[5] and Dorbane et al. [6] fully characterized friction stir welded Mg-Mg (AZ31B) joints. It was found that the best ultimate tensile strength was obtained for a combination of process parameters of 1200RPM and 150mm/min and was equal to 94% of the parent metals' strength. Additionally, a mechanical dependence was observed to the temperature and to the welding direction with respect to the machining direction. Ugender et al.[7] have worked on the characterization of AZ31B friction stir welded magnesium alloys under impact loading with respect to process parameters and tool material; the best results were obtained for 1120RPM and stainless steel tool material with approximately 75% of the toughness of the un-welded metal recovered.

Dissimilar friction stir welding (DFSW), a variation of FSW where two dissimilar materials are joined, presents new challenges that may affect the overall quality of the weld due to the large difference in the properties of the welded materials. As the use of lightweight materials is increasing in engineering applications around the world, aluminum alloys are finding their way more and more especially in the automotive industry. However, some structural parts could not yet be replaced by aluminum and are still conventionally made of different grades of steel or other common alloys such as magnesium or brass. Esmaeili et al [8] studied the effect of the tool's rotational speed on the mechanical properties and the formation of intermetallic at the welding interface between brass and aluminum 1050. It was found that at an optimum rotational speed the intermetallic layer is very thin and the tensile properties are high. At low RPM values of rotational speed, low friction led to the absence of intermetallic. A hardness profile and an XRD analysis completed their mechanical study of the welded joints. On another hand, Aluminum to magnesium joining is one of the top priorities in materials joining technology for the weight reduction. However, many authors have reported the creation of an intermetallic layer, such as the α-$Al_{12}Mg_{17}$ and β-Al_3Mg_2 shown in the phase Al-Mg phase diagram in Figure 2 [9], between the two materials with detrimental effect on the weld strength and quality.
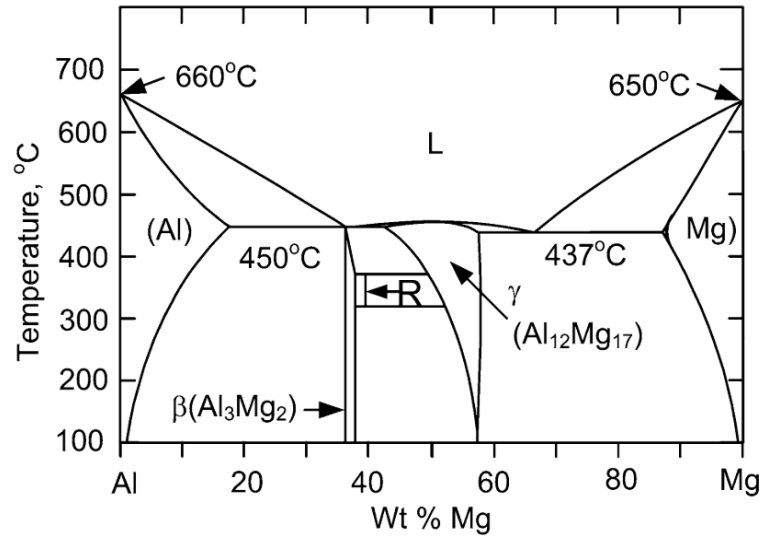
Figure 2 Al-Mg phase diagram [9]

Firouzdor and Kou [9] investigated the effect of the process parameters on the heat input and the resulting joint condition of butt welded AA6061 aluminum to AZ31 magnesium. At low travel speed, placing the Mg alloy to the AS may improve the strength of the joints by reducing heat and thus reducing the intermetallic formation. However, at fast travel speeds this would no longer apply. Moreover, the window of process parameters combination is found to be much larger in the case of this arrangement and even larger when the tool is offset to this same side. In a more general approach, Pourahmad et al.[10] found that in order to get a defect free aluminum magnesium weld, the harder material should be placed to the advancing side. Sato et al.[11] welded AA1050 to Mg AZ31 and found that $Al_{12}Mg_{17}$ had formed at the weld center and was associated with significant hardness increase. Somasekharan and Murr [12] studied the microstructure of a dissimilar friction stir weld formed between AA6061-T6 and AZ91D where evidence of dynamic recrystallization was found in the weld region causing the grain size to decrease and resulting in joints of higher hardness. Mofid et al.[13] investigated the effect of water cooling on the quality of the weld between aluminum and magnesium and the resultant microstructure.

Similarly, the use of FSW to join different aluminum alloys to different types of steel alloys is investigated by many researchers due to the numerous applications using these two materials. Dehghani et al [14] welded mild steel to aluminum whereas Liu et al. [15] concentrated on high strength steel. In the former, an IMC layered was reportedly formed for a specific combination of process parameters and in the latter, the properties of these possible IMCs were focused on; the Al-rich compounds (such as Fe_2Al_5, $FeAl_2$, Fe_2Al_7 and $FeAl_3$) are hard and brittle and cause detrimental effects on the mechanical properties of the joints whereas the Fe rich compounds have a less pronounced effect. Similarly, Chen et al [16] also reported the creation of many IMC following experimental FSW of aluminum to mild steel and Liu et al [17] investigated the effect of the process parameters on their formation during welding of high strength steel to aluminum where two IMC were identified, namely FeAl and Fe_3Al, in the form of a 1μm thick layer. Other results of dissimilar FSW [18] of aluminum to mild steel showed that IMC formed at the interface between the scattered steel found in the aluminum matrix. The Al-Fe phase diagram in Figure 3 shows the different intermetallic phases that could be created under different conditions of temperature and composition.
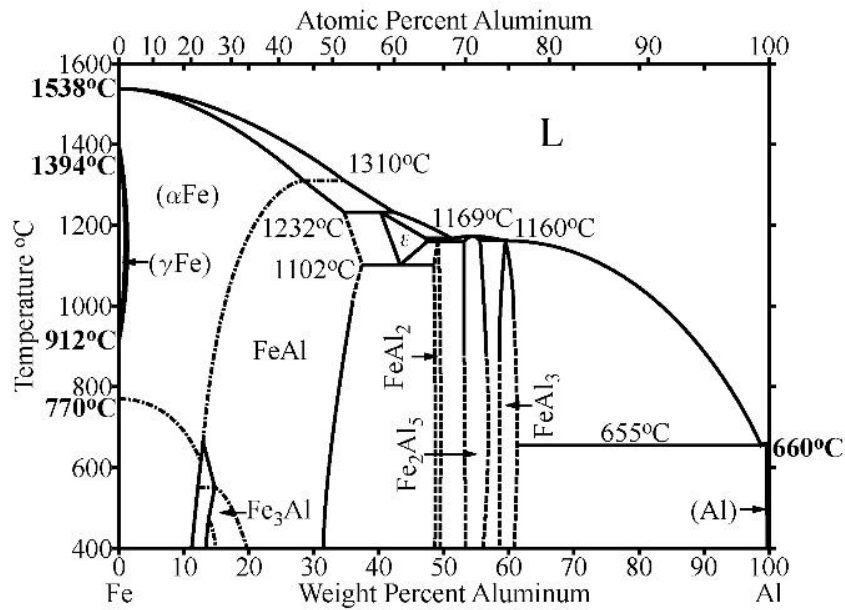
Figure 3 Al-Fe Phase Diagram [19]

Also several other research works discussed the effects of these compounds and the process parameters on the mechanical properties of the joints; Uzun et al [19], in the welding of 304Stainless steel to aluminum AA6013-T4, reported a recovery of approximately 70% of the original aluminum alloy strength in the weldment. In some other case, for example in the works of Tanaka et al [20], the maximum strength did not exceed 60% of the original un-welded and weakest metal, in this case the aluminum alloy. The mechanical analysis of the joint quality in this last reference is also coupled to SEM imaging which revealed a layer of IMC and which increasing thickness was shown to decrease the joint strength. Finally, Liu et al. [17] reported a maximum tensile strength equal to 85% of the base aluminum alloy strength in their study.

The tool, being the source of heat generation, is a key factor to the FSW process. It is typically constituted of a pin (or probe) and a shoulder the geometries of which greatly impact the mechanical quality of the weld. The mixing between the two materials is also an indication of the integrity and strength of the weld and is also

25

mostly related to the tool geometry. The effect of the shoulder and its characteristics has been studied by Zhang et al [21] in which three main characteristics of the shoulder were defined: outer surface, end surface, and end surface feature. The outer surface shape is either cylindrical or conical. However, since less than 5% of the shoulder is engaged in the workpiece the shoulder shape is rather found to be insignificant. The end surface shape is typically flat, but can also be concave or convex. The flat shoulder generates downward force but allows material to extrude under the edges, causing an excessive flash, whereas the concave shoulder is designed to restrict the extrusion of material. The gap in the concave shoulder allows material to travel up and then exerts a forging force on the workpiece, significantly improving material flow. When it comes to the convex shoulder, and depending on the plunging depth, the entire surface of the tool can get in full contact with the WP which presents a major advantage of this geometry. However, the main drawback of this shoulder profile remains that it causes the material in question to be displaced away from the probe. An optimal shoulder size was also the main focus point of Rajakumar et al. [22] due to the primary effect it has on the soundness of the FSW joint through the generation of the majority of the heat on the surface and in the upper part of the sample and the resultant mixing produced in this region. While a very large shoulder diameter leads to a wider heat affected zone and deterioration of the weld strength, a very small shoulder results in a narrow contact area and thus cold joints and similarly a low strength.

Malarvizhi and Balasubramanian [23] compared several pin profiles by macroscopic observation of the cross-sections of the produced welds. This analysis revealed that cylindrical, square and triangular prism pins all produced defects due to absence of vertical motion of material, stirring too much material away from the stir

zone and insufficient heat generation. However, the tool with a threaded pin produced a defect-free weld as it addresses the issue of vertical motion in cylindrical tools by generating downward force. In this same study, the optimal ratio between the tool shoulder diameter and the plate thickness was found to be equal to 3.5 leading to better tensile properties in the case of AA6061 welded to AZ31B. Besides assisting in vertical flow, the threads also aid the stirred material in their movement around the tool according to Zhao et al [24]. The benefit of a tapered pin allows more heat generation due to larger contact surface, and promotes higher hydrostatic pressure in the weld, which enhances stirring and nugget stability. However, it may also cause greater tool wear. The effect of the tool design and the FSW setup configuration on the microstructure and the mechanical properties was also investigated in the work of Simoncini and Forcellese [25] in their works on DFSW of thin sheets of AA5754 to AZ31. It was also found that a pinned tool, rather than a pin-less tool, is advised for better surface appearance and better mechanical properties. The pin, which plays an important role in the resulting joint integrity, is responsible for mixing in the bulk of the sample. Its geometry is directly related to the volume of materials being plasticized and stirred. The larger the pin, the higher the stirred volume. Dialami et al [26] studied the effect of different pin geometries on the material flow and the temperature in the joints using a speed-up two stage simulation methodology. It was found that the pin surface affected the resulting heat generated and a cylindrical or tri-flute pin geometry can cause obstacles to the flow of material and possibly prohibit the joint from forming. According to the work of Motalleb-nejad et al [27] the quality of the weld was reported to be improved by the tapering of the pin and by its threading. These are results previously reported by Kimapong et al. [18] for FSW of aluminum to steel. Moreover,

27

two additional parameters have to be taken into account which are not related to the geometry of the tool itself but rather to its setup and configuration; the tilt angle and the offset of the tool significantly contribute to the weld soundness. According to Long et al [28] defects tend to appear in the weldment for a 0^0 inclination of the tool and disappear for an inclination of 2^0. As for the offset, it was investigated by Chen et al [16] and Dehghani et al [14] during the welding of aluminum alloys to steel and in both cases a large offset of the tool into the steel side yielded defects in the weld line. Finally, the tool material also presents another parameter to be considered when deciding on a tool where the friction between the tool and the workpiece, which impacts the weld quality, varies not with the tool material but also with its surface roughness and wear. This aspect was approached by Al-Badour et al [29] where an increase of the friction coefficient resulted in lower defects and voids. Conclusively, optimizing the tool geometric configuration together with the process parameters produces the best results in terms of strength and overall weld quality according to the work of Blignault et al [30].

On another hand, the material flow between the advancing and retreating sides, is one of the essential information to be tracked during the process of FSW, as it can provide clear evidence of the mixing between the two regions and thus reflects the joint integrity. Different tracking routes methods are reported in the literature such as the technique used by Wu et al [31] where thin copper sheets are employed as markers to track the flow of material during Friction Stir Processing (FSP) of aluminum 2024. In this work, the mixing results were utilized to develop a numerical model which is able to predict the nugget size and the flow close to the pin. This model revealed that the tool rotational speed has the larger effect on the flow across the weld line. As for Pourahmad

et al [10] the tracking of material flow was achieved using steel shots embedding in the advancing and retreating sides equally. The angle α by which the steel shots placed in the AS moved is larger than the angle β by which the steel shots placed in the RS moved. Additionally, the beads placed in the AS were able to cross the centerline and into the RS whereas the opposite was unachievable. The position of the beads was verified using X-ray imaging on the samples before and after the welding was done.

B. FINITE-ELEMENTS MODELLING OF THE FSW PROCESS

The complexity of the FSW process lays just as in the accurate choice of the process parameters as in the understanding of the flow and mixing of materials in order to create strong and sound joints all while avoiding the different IMC that are likely to appear at the interface. After taking the time to understand the experimentally accessible details of the process of FSW and DFSW, numerical modelling was exploited in an effort to reproduce the long and costly experiments and investigate more suitably the different state variables that are hard, and sometimes impossible, to measure during the experiments. Therefore, it is imperative that accurate modeling of this complex process is available to provide proper guidance for selecting the best combination of input parameters.

Much effort was expended in the last decade to simulate welding operations using FEM. Several commercial software packages are available for this purpose such as DEFORM, ABAQUS and ANSYS. Some of the first numerical simulations of FSW used thermal models where the tool was modeled as a heat source without calculating mechanical stress and strain. Li et al [32], and using ABAQUS, developed a model for Al/Fe dissimilar FSW based on functionally graded materials (FGM) principles.

However, only thermal stresses were taken into account, yielding results in fair agreement with experiments. In their subsequent work, these same authors [33] used again the FGM method to create Al/Fe DFSW joints where the tool was modeled as a heat source. Once more, thermal stresses and strains were investigated. A variation to this model was also added later on and in which the volume of the nugget zone increased with time using a time varying FGM method [34].

Later, more accurate models using coupled thermo-mechanical based finite elements simulations started developing where both thermal and mechanical effects were accounted for. These thermo-mechanical methods however differ from one another by the different adopted theories used to compute the results such as computational fluid dynamics (CFD), computational solid mechanics (CSM) with Lagrangian and/or Eulerian formulations. One of the first CSM models used to simulate the FSW process in similar Al-Li alloy plates is proposed by Xu et al. [35] in which the material flow is also tracked and compared to experimental findings. In other publications, Schmidt and Hattel [36] used an arbitrary Lagrangian-Eulerian (ALE) formulation to complete their 2D/3D thermo-mechanically coupled model simulating the steady FSW process and provide insight on the material deformation. Similarly, Al-Badour et al. [29] proposed a Coupled Eulerian-Lagrangian (CEL) formulation which provides a limited distortion of the mesh in their FSW model used in the case of dissimilar aluminum alloys (Al5083-O to Al6061-T6). Both cited references validated their models against experiments. Jamshidi et al. [37] constructed a thermo-mechanically coupled simulation under ABAQUS to investigate the behavior and microstructure evolution during the welding of two types of aluminum alloys namely AA6061-T6 /AA5086-O. It was found that placing the AA5086 in the advancing side

resulted in a more efficient mixing at the weld nugget. Gupta et al. [38] also developed a thermo-mechanically coupled model under ANSYS where Al/Cu bimetallic lap joints were created. The temperature profiles were monitored in the advancing and retreating side making sure that it does not exceed the melting temperature of the base metals in addition to the monitoring of the stresses developed by this deformation process, unlike Hamilton et al. [39] where the temperature in their model exceeded the melting temperature of the materials investigated. In their work, Hamilton et al. [39] successfully modeled the three stages of the FSW process namely plunging, dwelling and traversing. Several field variables were developed such as temperature and stress and strain fields in the weld line. Additionally, material movement was visualized by defining tracer particles at positions of interest. Based on this work, Gao et al. [40] proposed a novel finite elements model developed under ABAQUS to study the material flow in a FSW process of similar aluminum alloys. The novelty of this model lies in the two stage meshing method applied; a Lagrangian adaptive mesh is used for the entire workpiece during the plunging phase as opposed to a Eularian adaptive mesh to investigate the material flow during the steady welding phase. Temperature profiles at key locations in the workpiece were tracked and compared to experiments for the model validation.

Using the FEM software Deform, Ammouri and Hamade [41] developed and tested a relationship based on a power law to predict the grain size as a function of the process parameters used in a thermo-mechanically coupled finite elements model of FSP of AZ31B magnesium alloy. The obtained numerically generated temperature profiles were validated using experiments reported in the literature by Chang et al. [42]. In other subsequent work of Ammouri and Hamade [43], three constitutive equations

were compared to the literature finding of Zhang et al. [44] toward a more realistic simulations of these processes. Additionally, for the same authors, material flow stress was investigated for the FSP of Mg AZ31B and the best flow stress model was proposed [45]. The modelling of the FSW process in the case of dissimilar materials using finite element software is a variation that has not been widely developed. This is partly due to the complexities which take place during this process, including, but are not limited to, the complex material flow and the high probability of generation of IMC as a result of the severe plastic deformation and increased temperature.

This dissertation comes as an extension of Ammouri and Hamade's previously reported works such that dissimilar materials could similarly be modelled using finite elements software Deform with a focus on Aluminum/Steel interfaces and a parametric study of the effect of the friction coefficient and the tool geometric features on the temperature and mixing evolution and on the joint integrity. The proposed FEM work paves the way towards a precise prediction of the locus and quantity of the resulting IMC at the interface between dissimilar materials, which constitute the primary source of weaknesses and brittleness in the joints. Moreover, the model was validated against experiments conducted on the same materials and using the same tools reproduced in the FEM. The comparison was based on temperature mixing profiles and analysis.

C. MOLECULAR DYNAMICS OF INTERMETALLIC COMPOUNDS

A prerequisite for IMC formation is material intermixing. Solid-state mixing in metals is accelerated by heat according to the Arrhenius relation. Also, mixing may be aided by high-stress mechanical loading commonly known as mechanically assisted mixing. Under specific conditions of temperature and pressure, IMC are likely to form

in interfacial systems. Fundamental aspects of IMC formation can be studied via atomistic simulations and MDS. MD is a numerical computational method which studies the interaction between atoms/molecules under different dynamic conditions. Several studies have utilized it to predict the creation of such compounds especially in multilayered systems as well as to understand the nucleation mechanism of the IMC at the molecular level. MDS is very sensitive to the potential adopted, the timestep and the computing times, but still provides a powerful tool for the investigation of this interfacial behavior. It is used in the literature for single and poly crystalline Al, Fe, as well as many other systems. Moreover, understanding the mechanical response of metallic materials subjected to extreme thermo-mechanical loading is of great importance in many engineering and technological applications such as solid state welding and explosive forming. For characterizing the behavior of metals under such ultrahigh strain rates and temperatures, shock and impact techniques (including shock compression and laser driven experiments) have been used to investigate the different aspects of plastic deformation. However, and due to the extremity of the loading and the very short time involved in these experiments, the level of uncertainty in the results cannot be overlooked. While a persisting challenge lies in linking MD-obtained results from ideal simulation setups to those of experiments, MD presents an advantage in the attainable high strain rates that it mimics. As such, MD offers a powerful simulation tool for investigating materials plastic deformation that is governed by the nucleation, multiplication, and motion of dislocations. The mechanism of induced plasticity is believed to be largely dependent on temperature and rate of deformation whereby thermal activation or phonon drag mechanisms may dominate or coexist depending on the loading conditions [46].

The work reported in this dissertation investigates firstly the probability of creation of an intermetallic compound in solid state at an incoherent interface, formed by Al (FCC) / Fe (BCC), under diverse mechanical loading and prescribed temperature conditions. Intermetallic compounds in such systems were shown to form by mechanical alloying of elemental aluminium and iron powders [47] or by other deposition techniques such as physical vapor deposition of aluminium thin film on low carbon steel substrate [48]. One engineering application of such a system is that of friction stir welding of aluminium AA6061 to low carbon steel where intermetallic compounds, Fe_xAl_y (e.g., FeAl, Fe_3Al) were shown to form at the abutted surfaces [14,18]. The creation of such compounds in the interfacial region between dissimilar materials may have detrimental effects on the structural integrity of welded joints. Therefore, understanding the mechanisms of formation and conditions under which Fe_xAl_y compounds evolve is of paramount interest. A considerable amount of work exists in the literature on Al (FCC) / Fe (BCC) systems. Employing the EAM, Chung and Chung [49] simulated the growth of Al (FCC) thin film on Fe (BCC) substrate and vice versa. Utilizing the Radial Distribution Function (RDF) analysis to determine the structure of the evolved FeAl intermetallic compound, it was found that kinetic energy did not have an effect on the intermixing of the two compounds and the evolution of FeAl intermetallic while temperature did. Depositing Fe on Al substrate was found to result in the creation of FeAl intermetallic compound, including at room temperature and at low kinetic energy values, whereas depositing Al on a Fe substrate shows no intermixing under these conditions. With the aid of [57]Fe Mossbauer spectroscopy with respect to crystal orientation, Sule et al. [50] reported similar asymmetry findings to those reported by Chung and Chung [49] regarding the growth of Al/Fe interface

during mixing between Al and Fe. Fonda and Traverse [51] showed evidence of intermixing between iron and aluminium and, consequently, the formation of iron aluminide intermetallic compound using physical vapour deposition of Al/Fe at room temperature but the exact structure of the formed compound was not identified. In order to validate the potential used in the Modified Embedded Atom Method (MEAM), Hao and Lau [52] employed the second nearest neighbour to examine the interaction of deposited Fe on aluminium. Liao et al. [53] investigated the interaction between a prismatic plan and the $Mg_{17}Al_{12}$ precipitate which was studied in MD using the modified embedded atom method potential for the Mg-Al alloys. The initial properties for the $Mg_{17}Al_{12}$ can serve in the comparison the results of future work when creating this IMC between Al and Mg system, but this was the closest work that can be found in the literature regarding MD of IMC between Al-Mg. One of the objectives of this the study is to investigate dislocation IMC interactions and its effect on the mechanical response of the weld.

Other systems were also simulated in molecular dynamics and reported in the literature such as in works of Chang et al. [54]. The sensitivity of the yield stress in a Titanium single crystal under tensile deformation strongly depends on its orientation and at a given orientation and the yield stress drastically increases with increasing strain rate for $\dot{\varepsilon} > 10^{10} s^{-1}$ while it increases but at a slower rate for a strain rate lower than this value. In other work, El Ters and Shehadeh [55] investigated the mechanical response of single crystal BCC iron under compression over a wide range of temperature (300K-900K) and strain rate ($10^2 s^{-1}$-$10^7 s^{-1}$) using multiscale discrete dislocation plasticity (MDDP). A power model for the yield stress as a function of temperature and strain rate was then proposed showing the temperature softening (with

35

a coefficient of n=-0.61) as well as the strain rate hardening effects (with a coefficient of m=0.184). Additionally, Hassani et al. [56] used the Embedded Atom Method (EAM) in their MD simulations to study the structure and growth of the interface when depositing aluminium (FCC) on a nickel (FCC) substrate. Similarly, Wu et al. [57] studied the intermetallic compound formation in a Ni (FCC) / Al (FCC) system created via physical vapour deposition. Other system such as the Ti (HCP) / Al (FCC) system studied by Kiselev and Zhirov [58] investigated the formation of the TiAl intermetallic compound at a thin interface utilizing the Lennard Jones potential and the RDF post-processing tool in OVITO which showed the resultant $L1_0$ structure of the γ-TiAl intermetallic compound.

Another aspect of MD studies in multi-layered systems, apart from the interfacial structures, involves the investigation of dislocation nucleation mechanisms. In this regard, coherent interfaces formed of similar crystalline lattice systems (e.g., FCC/FCC) are typically studied [59] under the same crystalline orientation. While much work has been reported on simulating the plastic response of single and poly crystalline Al and Fe little can be found on multilayered Al/Fe systems. Chen et al. [60] investigated the mechanical properties of a Cu (FCC) / Ni (FCC) interface with respect to the twist angle and found that yield stress decreases with increasing twist angle accompanied by increase in the misfit dislocations density. Zhou et al. [61] studied a coherent interface between two materials of the BCC crystalline lattice type where crack propagation was assessed as function of loading conditions. Compared with coherent systems, incoherent interfaces (e.g., BCC/FCC systems) are studied less. The interface of incoherent systems may be described as 'opaque' acting as a barrier to slip transmission as dislocation trap [62,63]. Such a system is that of copper (FCC) and

niobium (BCC) which was reported on by Shao et al. [59], Wang, et al.[64], Hoagland et al. [62], and Abdolrahim et al.[63]. The Kurdjumov and Sachs (KS) crystallographic orientation was adapted for this mixed FCC (Cu)/BCC (Nb) interface system whereby the [111] plane of the BCC material is placed parallel to the [110] of the FCC material [64]. Such crystallographic orientations offer the least misorientations between slip planes of the two structures thus allowing the highest chances for dislocations continuity and movement across the interface [59,65] used the KS relationship for a Mg (HCP) / Nb (BCC) system by adopting the crystal orientation using the generalized stacking fault energy method advanced by Vitek [66,67]. Partial dislocations were detected at the interface instead of the more commonly arising full dislocations. In the work of Gerlich et al. [68], the microstructure and stress strain response of aluminum poly- and bi- crystals was investigated using molecular dynamics (MD) simulations. The system was loaded in compression at high strain rate of $10^8 s^{-1}$ and temperature ranging between 845K and 910K (just below melting) and the average flow stress during the final 5% strain was fitted to a thermally activated Arrhenius equation from which the activation energy was then found. In [69] high strain rate ($10^9 s^{-1}$ and $10^{10} s^{-1}$) tensile deformation was applied at low temperatures (150K and 250K) to an aluminum/Metallic glass interface to study its strength and deformation mechanism. It was found that Shockley partial dislocation motion was the dominant deformation mechanism which appears in the aluminum region close to the interface although their activation energy is considerably high. It was also noted that the strain rate has a positive hardening effect on the strength of the interface unlike the temperature which has a softening effect. Significant amount of work has been reported in the literature for iron and iron based systems under compression and tension using MD. Dutta [70]

showed an accentuated effect of the temperature at high strain rate uniaxial compression of an iron nanopillar unlike what was reported in [71] for both FCC and BCC metals and which highlighted the effect of strain rate over that of temperature. Also studied in [70] was the deformation mechanism in an iron nanopillar at $10^8 s^{-1}$ and temperatures ranging from 50K to 500K. For the chosen Fe crystal orientation, it was found that increasing the temperature altered the deformation mechanism from dislocation slip mediated plasticity to slip plus twinning deformation. Similarly the deformation mechanism was compared in [71] between FCC and BCC metals., Nickel and tantalum were chosen as the samples respectively, and it was reported that the work hardening and cross slip are dominant in both cases over the thermal activation deformation with an addition of phonon drag in the case of the BCC metals. Additional molecular dynamics work reported by Sainath et al. and Sainath and Choudhary, respectively, in [72–74] studied a nanowire system formed of iron and loaded in tension at high strain rate. Next to the deformation mechanism which was found to be governed by full dislocation slip, the effect of the nanowire size and orientation on the flow stress (at 15%, 20% and 30% strain), yield strength and Young's modulus was investigated in details. It was found that the Young's modulus and the yield stress depend highly on the orientation of the nanowire whereas the flow stress decreases with the increase in the nanowire size. Most of the work reported in the literature focuses on a single material, and even sometimes single crystals, and the investigation of the deformation mechanism under a specific type of loading [75]. The mechanical response of single crystal BCC iron under compression was simulated [55] over a wide range of temperature (300K-900K) and strain rate ($10^2 s^{-1}$-$10^7 s^{-1}$) using multiscale discrete dislocation plasticity (MDDP). A power model for the yield stress as function of temperature and strain rate

was then proposed showing the temperature softening (with a coefficient of n= -0.61) as well as the strain rate hardening effects (with a coefficient of m= 0.184).

Experimentally, only few tests can achieve high strain rates that compare with the Split Hopkinson pressure bar test or shock compression and other laser driven experiments. Deformation mechanisms in such experiments can differ from those conducted in strain rate controlled uniaxial compression tests. Smith et al. [76] studied the response of the peak elastic stress at the onset of plastic flow for FCC aluminum, aluminum 6061 as well as BCC iron for a strain rate of $10^8 s^{-1}$. The results were also compared to other available literature models and it was found that the peak elastic stress σ_E is proportional to $\dot{\varepsilon}_p{}^{0.43}$ for both Al and Fe. As in many other references mentioned in their work, a general form for BCC metals modeling predicts a linear correlation between the stress σ and the strain rate $\dot{\varepsilon}$ in the thermally activated regime ($\dot{\varepsilon} = 10^4 - 10^6 s^{-1}$) that drastically changes to a power law $\sigma \propto \dot{\varepsilon}^n$ for higher strain rates [77,78]. Two regimes were differentiated; the first is at low dislocation velocities where the temperature has the major effect. This is usually translated in the thermal component of the model. The second regime is for high dislocation velocities where the effect of temperature is much less pronounced [79]. The multiscale modeling approach was mainly employed in few of the available publications in the literature such as in the case of Shu et al. [80] where the stress was found to depend on $\dot{\varepsilon}^{0.24}$ for steel and iron. In other shock experiments conducted on materials at very high strain rates, Armstrong et al.[81] performed an experiment on an iron plate and tracked the response of the flow stress at different strain rates beyond $10^4 s^{-1}$. It was found to increase exponentially after the threshold of $\dot{\varepsilon} = 5.0 \times 10^4 s^{-1}$ with a trend proportional to $\dot{\varepsilon}^{0.25}$.

On a final note, and given that the focus of the engineering applications has shifted in the most recent years from macro-processes to micro and nano processes with more extensive and elaborated research on micro electromechanical systems (MEMS), nano electromechanical system (NEMS) [82–84] and thin films characterization such as nanoindentation of multilayered materials[85–88] and Atomic Force Microscopy (AFM) [89,90], a concluding test was conducted in MD to shed some light on the mechanisms of deformation and the dislocation generation and propagation in the FSW process, which remain unchanged with the difference of scales going from nano to macro. The main disadvantages for using these numerical simulations to reproduce macroscale processes are associated mainly to the system size, the method precision [3] and the large difference between the timescale and the deformation strain rate range. However, many researchers were able to correctly reproduce the details of many processes by using numerical simulations [91,92].

Nano joining is one of these processes going from diffusion bonding [93,94], to explosive welding [95] to friction stir welding (FSW) [3]. This process has been modelled over many years using finite element simulations [96,97] and more recently in more limited research using MD methods. In the work of Konovalenko and Psakhie [98] and Konovalenko et al. [99] the effect of process parameters such as tool depth and the effect of an additional auxiliary vibration on the tool were investigated on the intermixing of the two regions respectively. It was found that increasing the tool plunging depth results in more intense heating and reduces the mechanical resistance of the plasticized metal thus increases the intermixing of the two regions. This however is accompanied by the increase of structural defects in the weld line, therefore a compromise on this specific process parameter is advised. Moreover, it was found in

[99] that adding an auxiliary vibration action to the tool increases the intermixing of the two regions involved in the mixing. This same result was also supported by Nikonov et al. [91] in the MD simulations of different modes of FSW. In their work, Nikonov et al. showed an improved mixing when a conical tool replaced the spherical one and when vibrations are added to the tool at different frequencies and amplitudes. Using these improved process parameters structural defects are reduced and a higher penetration is achieved in the case of similar materials, dissimilar materials and similar solid solutions occupying the two regions. Additionally, lattice rearrangement was observed when the conical tool was applied at the Cu/Fe interface, with copper atoms substituting iron atoms in the original Fe BCC lattice. This resulting structure is also supported by experiments. The optimization of the process parameters adopted during FSW, such as increasing the rotational speed or decreasing the advancing feed of the tool, aim to improve the mass transfer and intermixing between the two regions [100] but also decrease the total volume of structural defects [92] typically found at the interface following extreme plastic deformation such as in the case of FSW. Validation of the MD simulations may be obtained from the comparison between the resultant microstructure of the welded samples with experiments [92]. Once validated, such simulations would present new and practical ways to obtain information regarding non-equilibrium dynamic variables and sub-surface thermodynamic data that are usually out of reach during experiments [92,101].

MD simulations are conducted throughout all this work using the Large-scale Atomic/Molecular Massively Parallel Simulator (LAMMPS) [102]. Characterized in the first place, is the mechanical response of Al (FCC) / Fe (BCC) bi layer system under uniaxial compression loading, at constant strain rate of $5 \times 10^7 s^{-1}$ and over temperatures

41

ranging from T=150K to T=900K (just below the melting temperature of aluminium). During these simulations, the Mean Squared Displacement (MSD) method is employed to evaluate the resulting mixing of one element in the other (across the two regions of Al and Fe). The conducted simulations aimed at investigating the conditions of IMC formation under imposed compression and prescribed temperature. The likely composition of the formed Fe_xAl_y intermetallic structure after loading is determined to be FeAl as evidenced by the coordination analysis and by the RDF. Due to the wide range of its engineering applications, the Al/Fe interface has received much attention in recent years. These include the FSW process where post-processing of friction stir welded aluminum/ iron samples had shown in several studies the formation of FeAl and Fe_3Al IMC [14,18].

In the second tests, MD is utilized to investigate the mechanism of deformation in bimetallic Fe/Al interface compressed at strain rates of 5.0×10^7, 5.0×10^8, 1.0×10^9, and $1.0 \times 10^{10} \, s^{-1}$ and over the same temperature range employed in the first tests (150-900K). The yield stresses (first and second yield points) as well as the flow stress in the system, as obtained from the stress strain plots, are modelled with respect to temperature and strain rate for these extreme conditions. They are found to follow a thermally activated model.

On the other hand, the focus of the engineering applications has shifted in the most recent years from macro-processes to micro and nano processes. These application come with more extensive research on micro electromechanical systems (MEMS), nano electromechanical system (NEMS) [82–84] and thin films characterization such as nanoindentation of multilayered materials [85–88] and Atomic Force Microscopy (AFM) [89,90] out of many others. Therefore, the final MD simulations propose a

concluding numerical approach to model extreme rotational loading conditions which result in the mixing at the interface between Al and Fe regions at the nanometric level through the use of a rigid undeformable tool at different process parameters.

Eventhough the connection between the different scales, going from macro to nano, is not always straightforward, however understanding the mechanisms of deformation and the dislocation generation and propagation, which remain unchanged with the different scales, has led the researchers to apply and develop numerical methods such as molecular dynamics (MD) to reproduce and understand the desired processes. The main disadvantages for using these numerical simulations to reproduce macroscale processes are associated mainly to the system size, the method precision [3] and the large difference between the timescale and the deformation strain rate range. However, many researchers were able to correctly reproduce the details of many processes by using numerical simulations[91,92].

Nano joining is one of the investigated processes starting with diffusion bonding [93,94], to explosive welding [95] to friction stir welding (FSW) [3]. FSW has been more commonly modelled over many years using finite element simulations [96,97] but some recently published research has shown preliminary investigations of this process using MD [98,99]. The reported publications investigate the effect of process parameters such as tool depth and tool geometry along with the effect of an additional auxiliary vibration on the tool. It was found that increasing the tool plunging depth results in more intense heating and reduces the mechanical resistance of the plasticized metal thus increases the intermixing of the two regions. This, however, is accompanied by the increase of structural defects in the weld line, therefore a compromise on this specific process parameter is advised. Moreover, it was found in [99] that adding an

auxiliary vibration action to the tool increases the intermixing of the two regions involved in the mixing. This same result was also supported by Nikonov et al. [91] in their MD simulations. In this work, Nikonov et al. showed an improved mixing when a conical tool replaced the spherical one and when vibrations are added to the tool at different frequencies and amplitudes.

Additionally, lattice rearrangement was observed when the conical tool was applied at the Cu/Fe interface, with copper atoms substituting iron atoms in the original Fe BCC lattice. This resulting structure is also supported by experiments. The optimization of the process parameters adopted during FSW, such as increasing the rotational speed or decreasing the advancing feed of the tool, aim to improve the mass transfer and intermixing between the two regions [100] but also decrease the total volume of structural defects [92] typically found at the interface following extreme plastic deformation such as in the case of FSW. Validation of the MD simulations may be obtained from the comparison between the resultant microstructure of the welded samples with experiments [92].

These final simulations come as an extension to the previous two experiments using MD where a pristine Al/Fe interface is modelled under compression of different conditions of temperature and pressure. The nucleation of dislocations as a result of the severe plastic work induced by this tool is observed and analyzed and the structure of the subsequent mixed region between the dissimilar materials is investigated.

To the best of the authors' knowledge, no molecular dynamics simulation has been conducted on mechanically stressed Al/Fe interface in solid-state in order to assess the evolution of the IMC formed between these two materials. Moreover, the modeling

of yield stress and flow stress in a multilayered crystalline system as function of strain rate and temperature at high ranges of $\dot\varepsilon$ and T such as addressed in this study is also original to the literature. Such studies, although focused on the Al/Fe system, could well be extended into different systems, especially those that are commonly used in FSW such as Al/Mg for example.

CHAPTER III

EXPERIMENTAL FSW OF DISSIMILAR WELDS

In the context of problem definition and understanding of the FSW process and the effect of many process parameters involved in this process an internal experimental setup was arranged in order to produce friction stir welded samples using a CNC machine and an elaborated LabView code. Different tools were created and imported and adjustments were progressively implemented to the setup to improve the quality of the welds. The integrity of the joints was assessed through mechanical testing and microstructural characteristics. In the following section, details of these experiments and their results are presented.

A. METHODOLOGY

The process of FSW was achieved using a vertical CNC machine adapted to a HAASE-V5 milling machining center with a CAD40 spindle head holding the different types of tools (Figure 4). Many process parameters were modified during the experiments in order to improve on the quality of the welded joints. These process parameters include tool feed and rotational speed, plunging depth, material positioning, offset of the tool among other parameters. The dimensions of the specimens used during all the tests were 95mm x 45mm with a thickness between 2mm and 3mm depending on the welding tool. The fixing of these specimens evolved across several stages; first the plates were brought together and in position using a horizontal and a vertical vise. Later on it was decided to fix the plates more rigidly onto the backing plate made of hard C60 tool steel (Uddeholm Sverker 21) using 4 bolts.

During the two phase FSW process, the tool rotates in a clockwise direction first plunging between the two plates to a specific depth, then feeding and mixing the two sides together as a result of the friction between the tool and the WP and of the increase in temperature in the system. The plate in which the rotation of the tool and the advancing feed have the same direction is called the advancing side (AS) and the other side is the retreating side (in which the rotating and the advancing directions are opposite). Temperature monitoring at several locations was achieved using thermocouples and infrared (IR) sensors. Two thermocouples were implemented on the top of the backing plate, thus maintaining contact with the bottom of the specimens, placed at ±5mm from the weld line into the advancing and retreating sides respectively. Two other thermocouples were placed in the front and on the back of the backing sheet and finally, two infrared sensors were employed to measure the temperature close to the tool; the first IR sensor point to the tool itself and the other to the workpiece just in front of the tool.

Figure 4 Experimental FSW setup

The FSW experiments were performed on a selection of materials from magnesium to aluminum to steel; The first experiments were executed on similar materials welding and later on were developed into dissimilar materials welding. Table 1 summarizes the chemical compositions and nomenclature of the different materials used at any point during the experiments.

Table 1 Chemical composition of the different materials used at any point during the experiments [103]

Alloy Name		% weight									
		Al	Fe	C	Mg	Cr	Cu	Si	Mn	Zn	Others
Alum-inum	AA 1100	99.0 Min					0.12				Bal.
	AA 6061	97.9			1.0	0.2	0.28	0.6			0.02
Magn-esium	AZ 31B	3.0	0.005		97		0.05	0.1	0.2	1.0	0.045
Steel	AISI 1006		Bal.	0.08 Max					0.3 25		0.09

Moreover, different tools were also utilized during the experimental welding in an effort to understand the effect of the tool geometry on the resulting joints' integrity. Part of these tools was supplied by the Beijing FSW Technology company (China), whereas the other part was internally manufactured according to specific geometry standards. A list of these tools is presented in Table 2 with specifications of the tool materials, shape and geometry.

Table 2 Tools' geometries and dimensions

Name/ Designation	Shoulder diameter (mm)	Pin Length (mm)	Upper pin diameter (mm)	Lower pin diameter (mm)	Concavity
HTS	12	3	3.9	2.8	Concave
Carbide	15	2	9	4.5	Convex
Concave tool	20	tapered 4	8.5	3.5	Concave
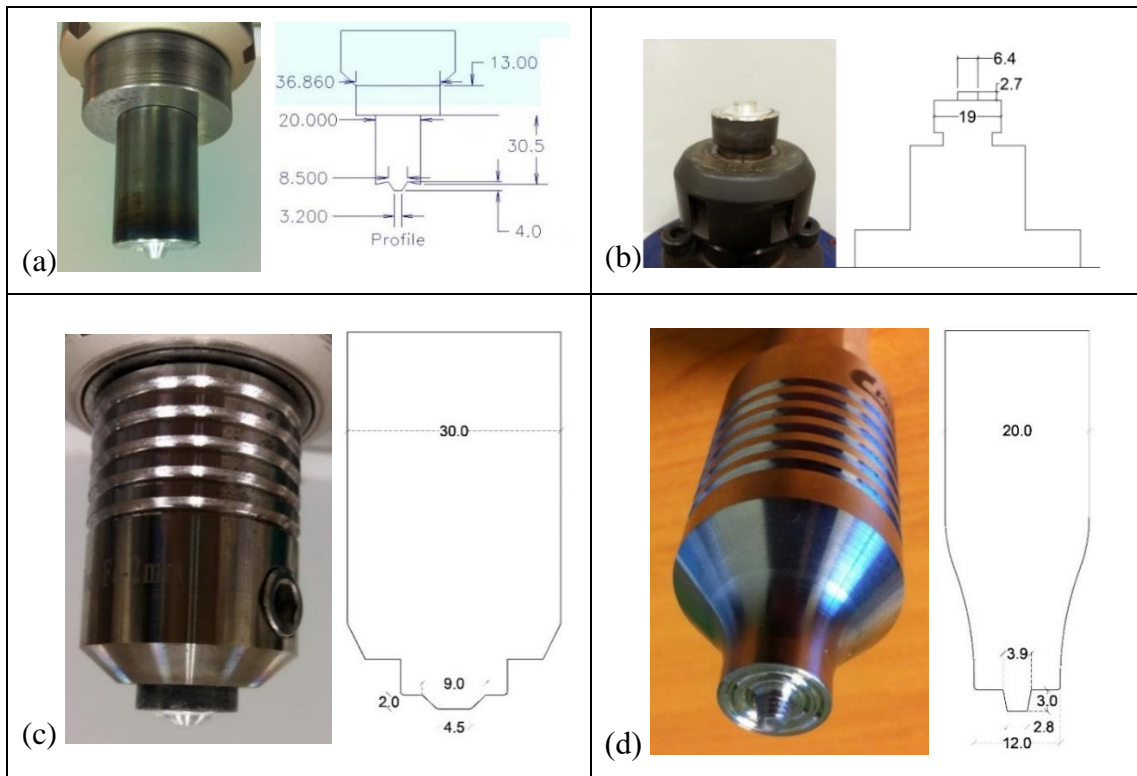
Figure 5 Geometric diagrams and dimensions of the different FSW tools

B. MICROSTRUCTURAL CHARACTERIZATION OF FRICTION STIR WELDED SIMILAR AND DISSIMILAR JOINTS

Microstructural analysis of the welded samples was performed through optical and electronic microscopy on one hand and X-ray diffraction (XRD) on the other. Cross

section specimens were cut from these joints and each was reworked to fit the specific requirements of the different analysis techniques; CSs intended to be used in optical microscopy were polished and etched before any observation in order to reveal to different grains and compounds. The optical microscope used during these analysis is the Olympus BX41M-LED. Moreover, the CSs were examined via scanning electron microscopy (SEM) coupled to energy dispersive X-ray detector (EDX). This operated equipment is a TESCAN, Vega 3 LMU SEM with an Oxford EDX detector coupled with INCA XMAW20. This analysis resulted in elemental composition plots evaluated at different positions along the thickness of the cross-sectional specimens. Finally, X-ray diffraction (XRD) analysis was employed on the solid samples using a Bruker D8 Discover X-ray Diffractometer to characterize and locate the intermetallic phases formed throughout the weld line.
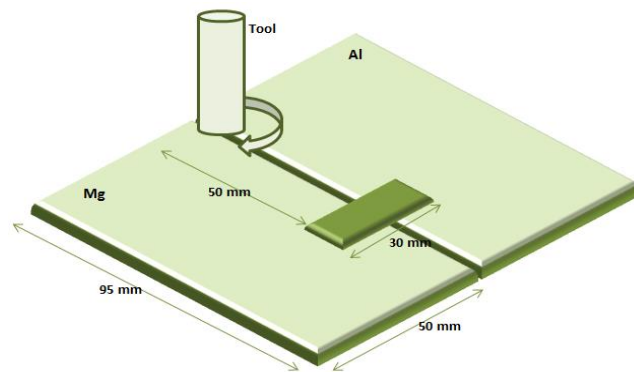
Figure 6 Location of CS specimens cut from plates

Two intermetallic phases, namely the α-phase ($Al_{12}Mg_{17}$) and the β-phase (Al_3Mg_2), were identified in the weld line of aluminum-magnesium friction stir welded joints. These were created using the sverker 21 conical tool and the process parameters listed in Table 3.

Table 3 FSW process parameters

Advancing side	Retreating side	Rotational speed	Advancing feed	Depth of plunge	Tool offset

AA1100	AZ31B	1400 RPM	300 mm/min	2.8 mm	1.5 mm to AS
AA6061					

The EDX analysis of the specimens cut from these joints exhibit some state of elemental cross-mixing between aluminum and magnesium on the surface and in the CS. The elemental composition results are presented in Figures 7 (a and b) and Figures 8 (a and b) where surface and cross-sectional analysis of the variation of Al and Mg content are investigated for the AA6061-AZ31B and AA1100-AZ31B joints respectively (along a distance of 30mm starting at 35mm and ending at 65mm). As can be seen in these profiles, the results show some mixing across the weld line on the surface of the joint due to the stirring action, pressure and heat imposed by the shoulder of the tool. The mixing is shift towards the aluminum side in the CS and closer to the magnesium side on the surface in both specimens. The elemental plots suggest that about 80% Al to 20% Mg ratio was reached upon conclusion of weld. Figures 7 and 8 have shown that the mixing at the surface does not different considerably given that the two samples are welded with the same tool; which shoulder is responsible for the majority of the work found at the surface. It is also noticed that the mixing at the surface is greater than that found in the bulk which could be due to the unthreaded nature of the pin used during these experiments. In Figure 7a, the Stir Zone (SZ) extends below the shoulder for 20 mm (from 37mm to 57mm). This zone is found to constitute of around 80% aluminum and 20% of magnesium. Across this part of the specimen, the aluminum weight, greatly larger than that of the magnesium, validates the notion of the superior movement from the AS to the RS than the opposite direction. This is due to the engagement of the concave shoulder which induces the largest peaks of mixing at around 40mm from the aluminum AS in both joints. This shoulder type contributes just enough in the surface mixing process but most importantly its concavity reduces the

stresses on the weld line. Across this same distance (37mm to 57mm) the CS elemental profile (Figure 7b) shows much less mixing. However, the mixing between the two alloys occurs from 44mm to 52mm which is the distance corresponding to the pin diameter. These plots confirm that the shoulder is responsible for the mixing at the surface and the pin in the bulk of the CS.

On the other hand, although the mixing on the surface of the AA1100-AZ31B is similar to the previous sample, with approximately 85% of Al versus 15% of Mg weight percentage on the surface, limited mixing can be noticed in the bulk of the weld (Figure 8b) with an abrupt change in the composition resulting in steep concentration gradients. These results are definitely due to an incompatibility between the two alloys in place, with the AA1100 containing at very high aluminum content and very little addition elements.
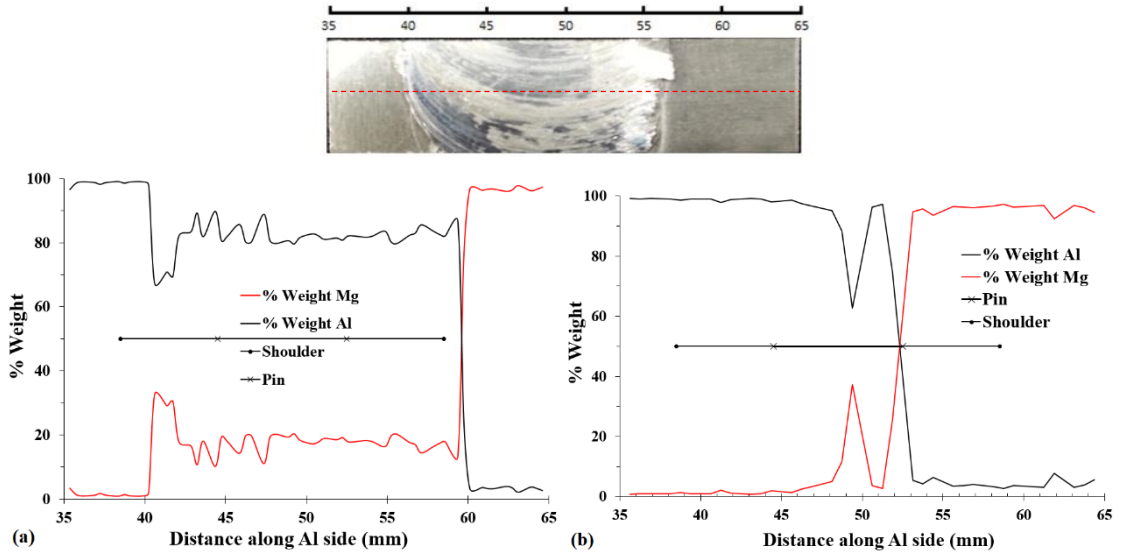
Figure 7 AA6061-AZ31B specimen and elemental mixing plot of its surface and CS
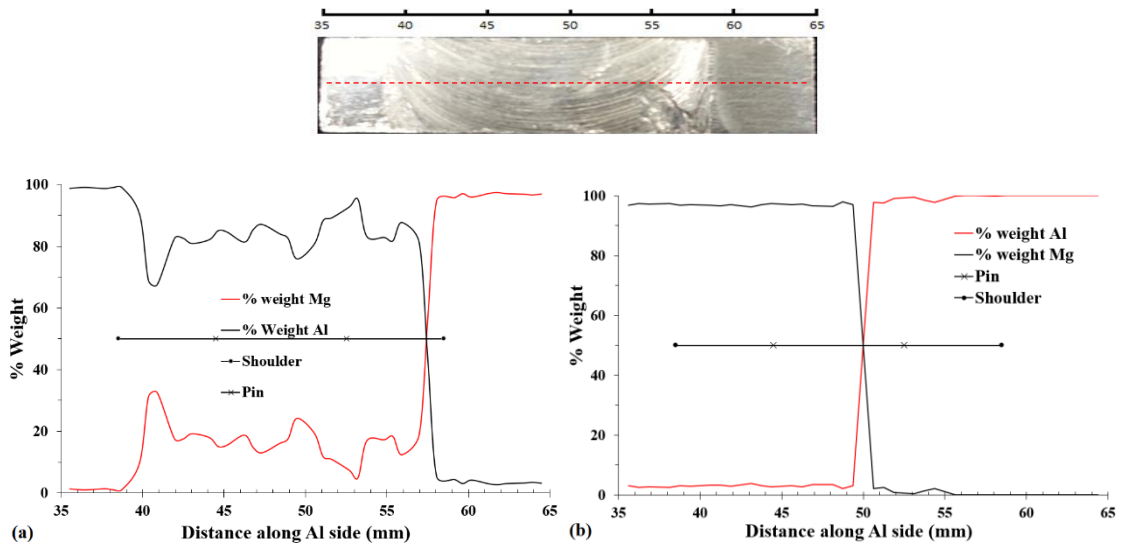
Figure 8 AA1100-AZ31B specimen and elemental mixing plot of its surface and CS

In other metallurgical analysis of the aluminum magnesium joints, XRD was executed on the top surface and across the cross-sections of the specimens. The X-ray beam was focused on a spot of 1mm radius on the surface center. A similar spot was also located on the CS center (Figure 9 shows the XRD setup with the specimen mounted in the middle). This analysis shows that intermetallic phases are more abundant in the cross-sections than on the surface and pure aluminum and magnesium

53

phases are detected on the surface (Figures 10a and 10b and 11a and 11b). The identified intermetallic phases are thought to induce brittleness and reduce the strength of the joints. Concentrations of the α-phase $Al_{12}Mg_{17}$ and the β-phase Al_3Mg_2 were spotted as well as the less prominent γ-phase $Al_{14}Mg_{13}$. Such intermetallic compounds are favored to form according to phase diagrams and are in agreement with what was reported by Sato et al. [11].

The higher content in intermetallic phases found in the CS is due to the larger mechanical deformation and plastic work induced by the pin in the bulk of the specimens even though less mixing is actually detected in the bulk. In this regard, most of the work generated by the shoulder is considered as heat resulting from friction unlike most of the work generated by the pin which is mechanical.
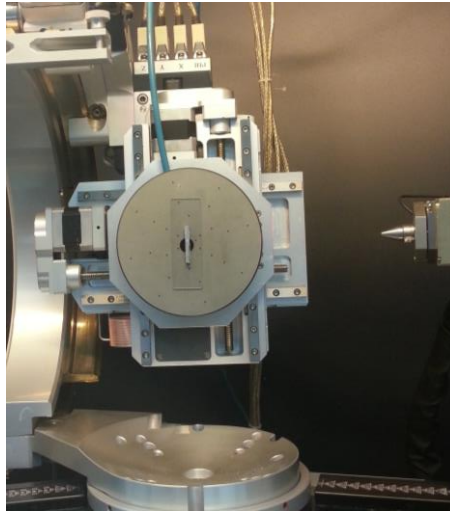
Figure 9 XRD setup showing beam focused on the welded section mounted on the stage
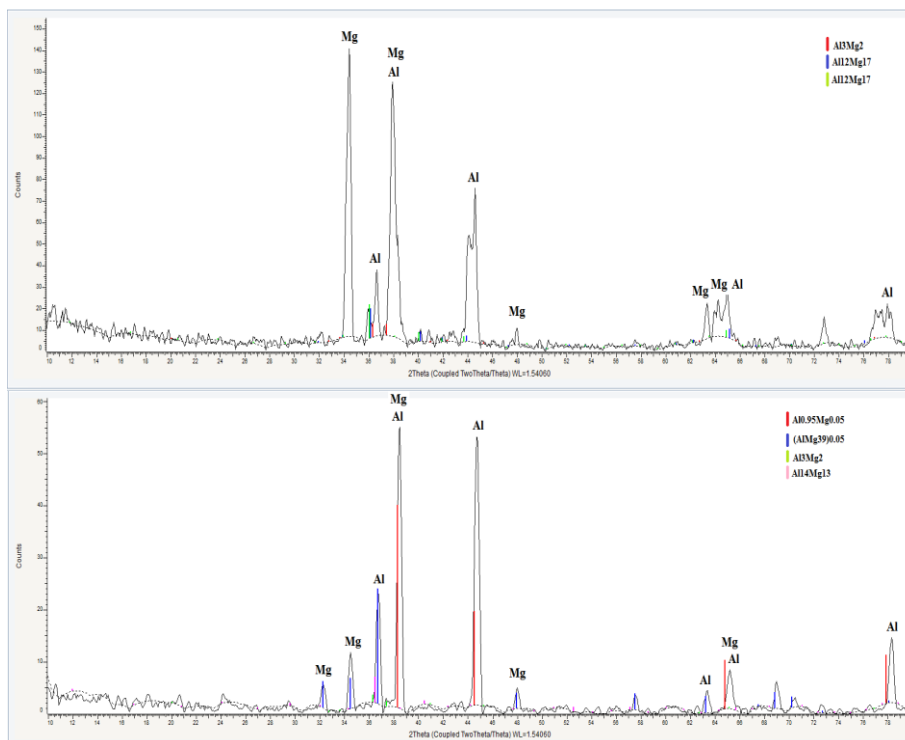
Figure 10 XRD pattern of AA6061-AZ31B (top) Surface and (bottom) CS
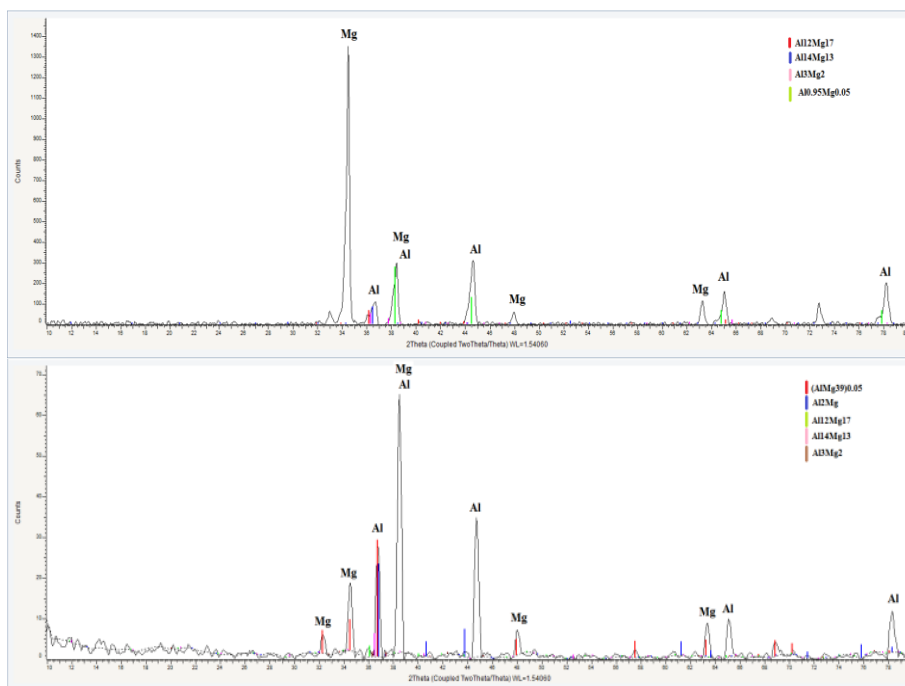
Figure 11 XRD pattern of AA1100-AZ31B (top) surface and (bottom) CS

In other experiments, aluminum was welded to low carbon steel. 2mm and 3mm thick samples are welded with two different FSW tools which geometries and dimensions are indicated in Figure 5c and 5d; the first tool is made from hardened steel

55

and reserved for the welding of 3mm samples whereas the second one is made from carbide and designed for welding of 2mm thick steel samples. Several process parameters are tested such as tool rotational speed and advancing feed. The temperature was tracked through four thermocouples placed at different positions in the backing plate and two infrared sensors pointing at the tool. The steel alloy used during this work has very low carbon content and is often referred to in the open literature as AISI 1006. Such an alloy contains an average 0.08% of carbon in weight. The aluminum alloy is the well-known AA6061 which contains several addition elements including magnesium, manganese and copper. The chemical composition of the steel and aluminum alloys is presented in Table 1 as it appears in the literature [103]. The steel plate was placed in all experiments at the RS and an offset was applied towards this side such that overheating of the aluminum is avoided and mixing between the two plates is increased.

Table 4 Combination of process parameters for aluminum-steel FSW joints

Designation	Speed (RPM)	Feed (mm/min)	Ratio	Depth (mm)	Offset to RS (mm)	Dwelling (s)	Thickness of plates (mm)
D1	1800	120	15	-2.88	0.75	20	3
D2	1800	120	15	-2.88	0	15	3
D3	1800	120	15	-2.88	0.25	15	3
D4	1400	100	14	-2.88	0.25	15	3
C1	800	130	6.15	-1.82	1	0	2
C2	800	200	4	-1.82	1	0	2
C3	800	200	4	-1.96	1	0	2
C4	400	100	4	-2	1	0	2

The chemical analysis (EDX/SEM, XRD) of the cross sections of the welded Al-Fe joints resulted in the elemental profile of Al and Fe shown in Figure 12 (a, b and c) for the 3mm thick plates and Figure 13 (a and b) for 2mm thick plates. For the 3mm samples, the profile was studied at three different positions in the CS: Top, middle and bottom. For the 2mm samples, the profile was only considered at two stages: Upper half and lower half. The intermetallic phases have precisely defined elemental compositions in either materials and therefore such an analysis can validate and confirm the presence or the absence of such phases at different position in the CS of the joint.

In the 3mm sample analyzed hereafter, it was found that the mixing is more stressed at the top and in the middle than at the bottom of the sample. This is due to the engagement of the shoulder and the activity of the pin. At several points in the profile, especially in the top and the middle, an important mixing is shown between Al and Fe as the atomic percentage of each of these elements ranges between 40-60%. This mixing is spread across a distance of approximately 4mm which is equal to the diameter of the pin. The threaded shape of the pin is responsible for the mixing found in the upper half of the sample as well as the threading found in the shoulder itself. Although the tip of the pin is a known zone where high deformation is induced, at the same time the fact that this region is very narrow doesn't favor the mixing in the bottom part of the sample.
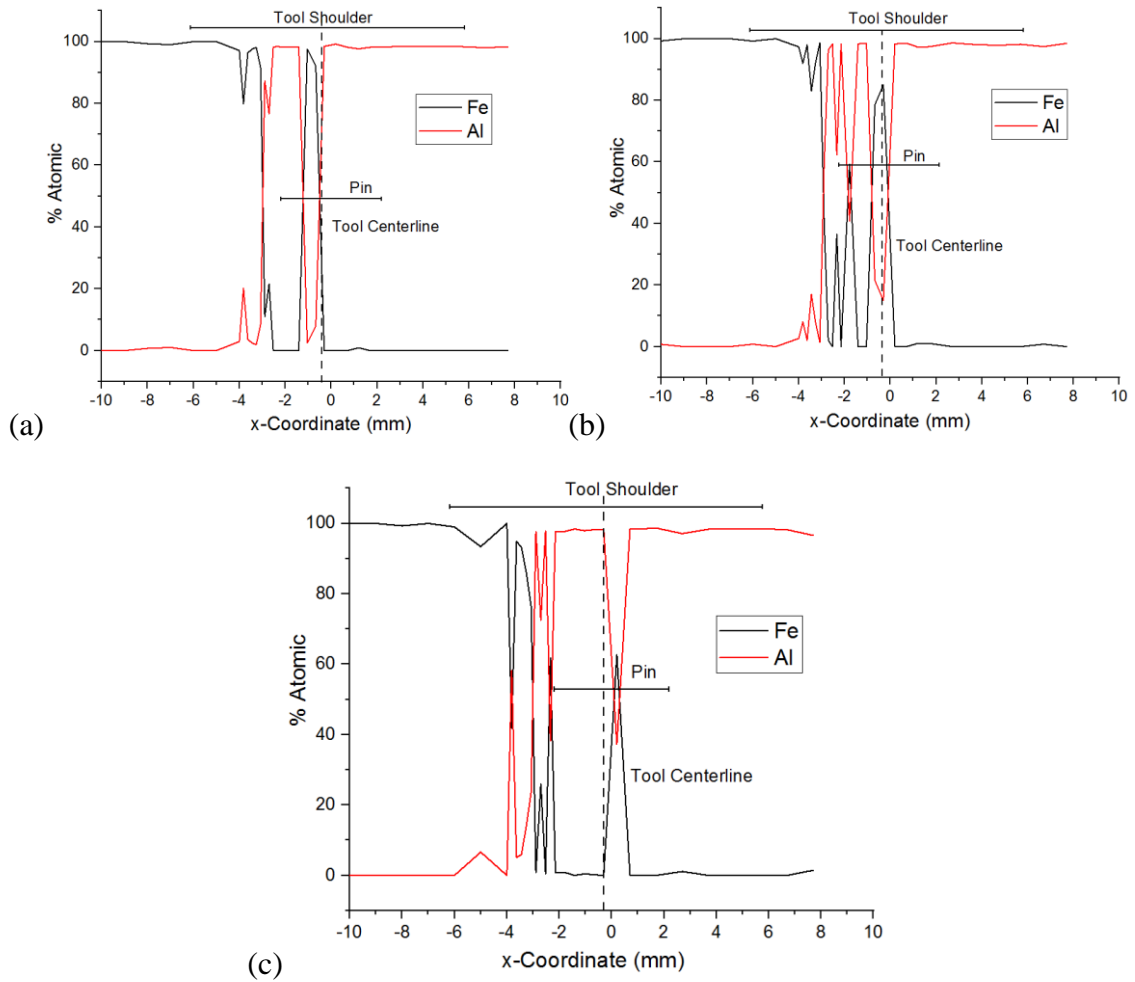
Figure 12 Al and Fe elemental compositions in D4 3mm sample at the (a) Top, (b) Middle, and (c) Bottom as obtained from EDX.

The carbide tool which was used to produce the 2mm samples has a convex, unthreaded shoulder and a large pin which generate lots of heat and friction between the two sides. The mixing in the top part of these samples is also better than that in the lower part just like in the previous samples (Fig. 13a and Fig. 13b). The weldment in these samples is made possible by the heat generated from the friction between the tool and the plates mainly if not merely. The joint is spread along 3-4mm.
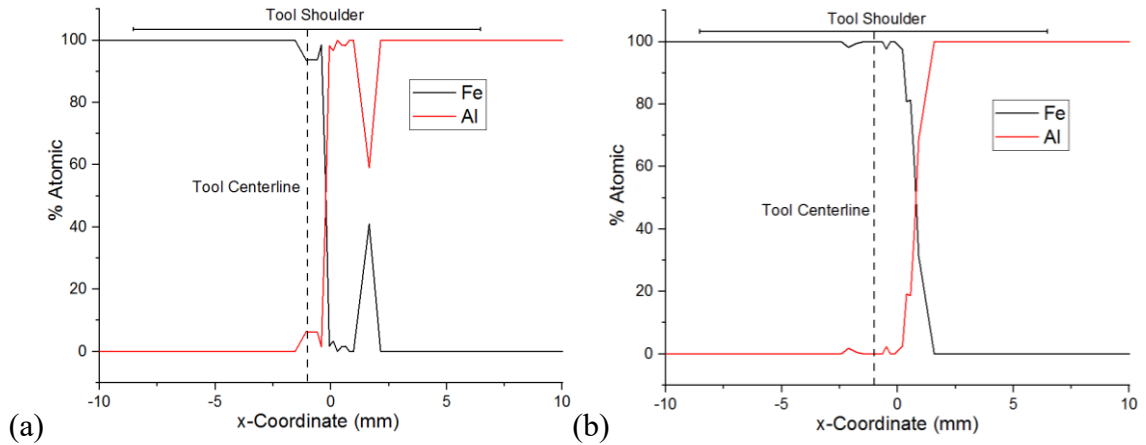
Figure 13 Al and Fe elemental compositions in C4 2mm sample (a) in the upper and (b) lower sections as obtained from EDX

At different positions in the CS of the joint, and given the elemental compositions obtained from the EDX analysis, intermetallic phases were suspected to form. The following Table 5 summarizes the types of phases as well as their positions in the joints in the D4 and C4 samples with respect to their compositions in Al and Fe.

Table 5 Intermetallic phases formed at different position in the CS of samples D4 and C4

Sample	x (mm)	Al	Fe	Expected IMC	Position in CS
D4	16.2	20.2	79.9	Fe_3Al	Top
	16.6	16.9	83.1	Fe_3Al	Middle
	16.2	58.2	41.8	$FeAl_3$	Bottom
	16.7	13.8	86.2	Fe_3Al	
	16.9	23.6	76.4	Fe_3Al	
	17.1	58.3	41.3	$FeAl_3$	Middle
	17.7	62.3	36.5	$FeAl_3$	Middle
	17.7	38.2	61.8	FeAl	Bottom
	18.2	40.8	59.2	$FeAl_2$	Middle
	19.3	21.4	78.6	Fe_3Al	
	19.7	15.0	85.0	Fe_3Al	
	20.2	37.3	62.7	FeAl	Bottom
C4	18.9	6.35	93.65	Fe_3Al	Upper half
	19.4	6.21	93.79	Fe_3Al	Upper half
	19.8	43.4	56.6	$FeAl_2$	Upper half
	21.7	59.01	40.99	$FeAl_3$	Upper half

Considering that the sample tested in SEM/EDX is 4cm in width, and considering the tool offset, the intermetallic phases are found in the middle of the sample, at the weldment position. They first form and develop closer to the Fe side rather than the Al side which is where the deformation in the material is expected to be higher. Qualitatively and from the Table 5 summary, it can be found that much more intermetallic compounds are found in the 3mm sample. This is due to the deformation induced by the threaded pin and shoulder of the HTS tool in comparison to just heat generated by the carbide tool. Therefore, it can be deduced that mechanical deformation is the primary source of intermetallic compound creation whereas the secondary source is the heat input generated from friction.

Moreover, XRD analysis was performed on the CS of the welded samples to validate the presence of the intermetallic phases. Figure 14a and 14b shows the XRD pattern of the D1 and C4 samples respectively across the CS, confirming the presence of $FeAl_3$, $FeAl_4$, $Al_{86}Fe_{14}$ and AlFe intermetallic phases at different "2 theta" positions, next to pure Al and pure Fe phases.

(a)

(b)
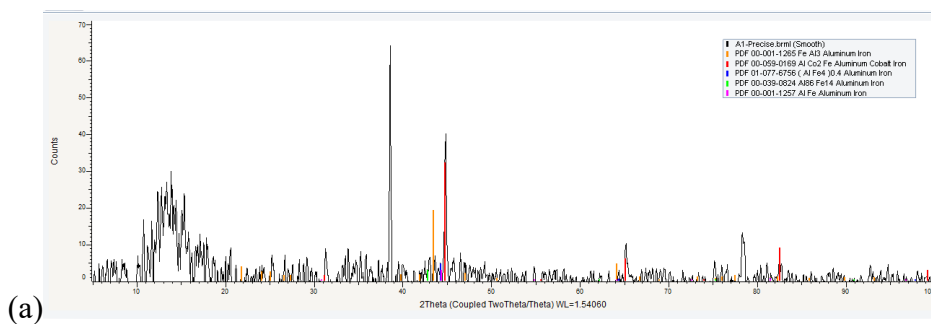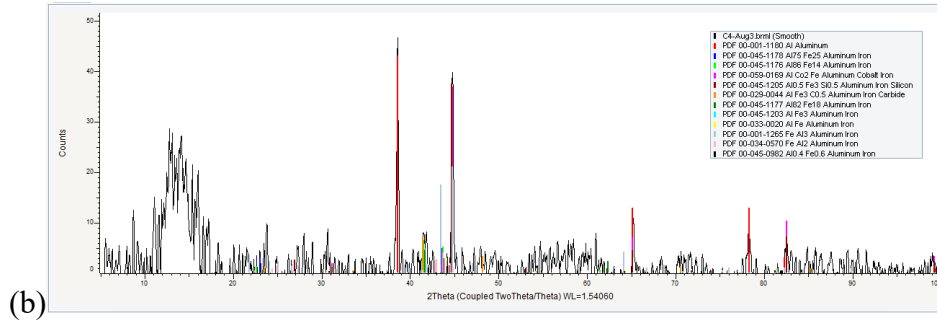
Figure 14 XRD pattern of the CS of (a) D1 and (b) C4 samples

C. MECHANICAL CHARACTERIZATION OF FRICTION STIR WELDED SIMILAR AND DISSIMILAR JOINTS

The integrity of the joints was also evaluated mechanically through tensile and impact destructive tests and micro-hardness nondestructive tests.

It is postulated that forming of intermetallic compounds (along with grain recrystallization) under the shoulder of the tool and in the heat affected zone (HAZ) would result in larger hardness values. The presence of intermetallics was substantiated using Vickers hardness measurements yielding profiles. The aluminum magnesium joints discussed in the previous section underwent micro-hardness measurements which confirmed the presence of clusters of hard intermetallic in the stir zone with hardness values approaching 400 HV. Indentations were performed along three lines located on the cross section and referred to as Top, Middle, and Bottom (Top line is closer to top surface). Hardness measurements vs. distance (from the Al side) can be seen in Figures 15a and 15b for the AA6061-AZ31B and AA1100-AZ31B welded joints.
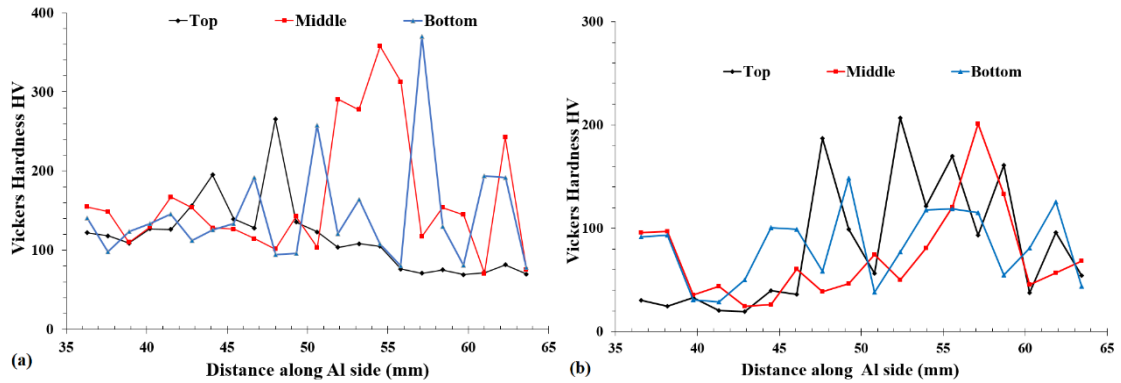
Figure 15 Vickers Micro-hardness for the (a) AA6061-AZ31B and the (b) AA1100-AZ31B welded joints

Peaks of high hardness values are observed at different locations in the both specimens with a clear shift towards the magnesium plate. In Figure 15a, starting Vickers hardness values are close to 100 HV, typical of AA6061. In this specimen, the intermetallic compounds which are thought to result in these high hardness values (max. just under 400 HV) are more abundant in the middle and bottom sections of the CS. These regions are heavily affected by the stirring action of the pin. The hardness profile also suggests that as the frictional force in the bulk of the material increases, as a result of the work of the pin, more intermetallic compounds are formed and thus fragility and brittleness is expected to appear. Closer the top surface, fewer regions of intermetallic (as evidenced by the lesser hardness peak values) seem to have formed and a rather smooth transition between the two materials is noticeable.

Figure 15b shows that in the AA1100-AZ31B welded joint, starting hardness values are in close to 40 HV which is also typical of soft AA1100 alloy. However, intermetallic compounds are found to be present in the three sections of the CS, starting at approximately 45mm from the aluminum side (which coincides with the left edge of the pin). The peaks attributed to intermetallic formations result in hardness values having a maximum of 200 HV, which is considerably less than those found in the case

of the AA6061-AZ31B welded joints. This is probably indicative of a different type of intermetallic compound that has formed between the rather pure aluminum alloy (AA1100) and magnesium as compared to the AA6061-AZ31B joint.

In other mechanical characterization, impact toughness of friction stir welded samples was evaluated using standard Charpy impact tests. The specimens cut for these tests were 55mm x 10mm x 3mm, as per the ASTM E23 standard. Two types of joints were fabricated by friction stir welding: Mg-Mg (similar materials) and Al-Mg (dissimilar materials). Their toughness was compared to that of the un-welded original materials. A limited experimental test matrix was constructed with two input variables: rotational spindle speed (ranging between 1200 RPM and 2000 RPM) and tool feed (varying between 150 mm/min and 550 mm/min). The combination of the process parameters used for each welded joint is shown in Table 6. The toughness of the magnesium AZ31B original metal was found to be equal to 6.27J and that of the aluminum AA6061 equal to 16.95J. Table 6 and Figure 16 also show the percentage of the recovered toughness of the welded similar and dissimilar joints with respect to the original un-welded aluminum AA6061 and AZ31B metals for the different combinations of speed and feed process parameters. It was found that the largest value of impact toughness, for dissimilar Al-Mg welds, corresponds to 1400RPM and 350mm/min tool speed and feed respectively. This combination also recorded the lowest values of temperatures at all sensors placed in the backing plate and on the workpiece. In the case of Mg-Mg welded joints, a similar conclusion was attained; the recovered impact toughness reached close to 100% for the combination of process parameters which yielded the lowest recorded temperatures in the joints.

Table 6 Process parameters and impact toughness of similar (Mg-Mg) and dissimilar (Al-Mg) friction stir welded joints with respect to the original un-welded metals

	Mg-Mg		Al-Mg			
	1200RPM 150mm/min	1400RPM 300mm/min	1200RPM 150mm/min	1400RPM 300mm/min	1400RPM 350mm/min	1400RPM 450mm/min
Toughness (J)	5.39	6.19	4.29	3.75	6.46	3.66
% of Mg base metal	85.95	98.74	68.47	59.82	103.06	58.38
% of Al base metal	-	-	25.31	22.12	38.11	21.59
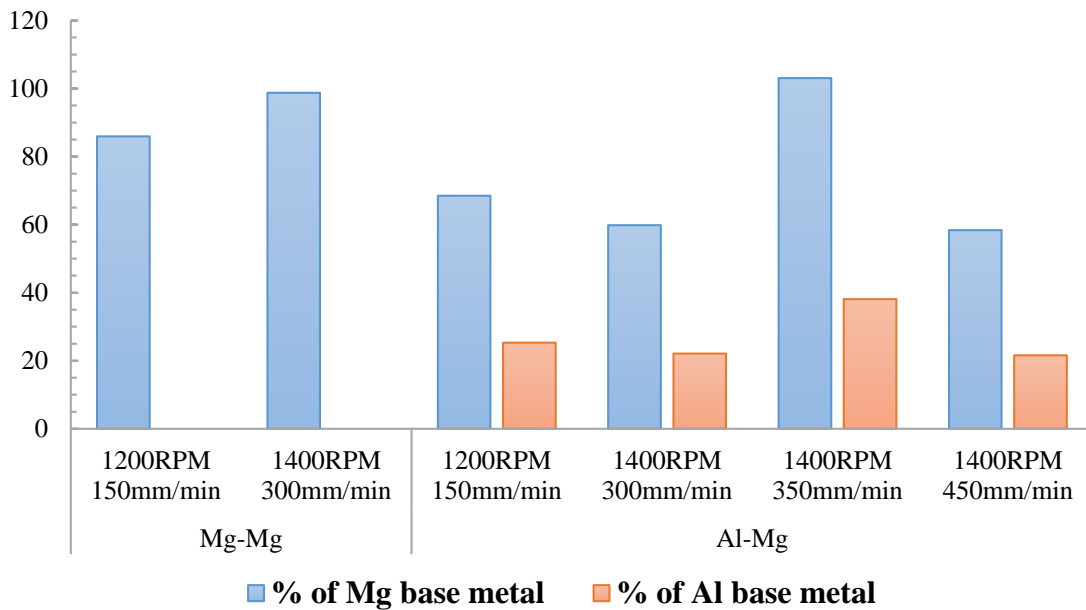
Figure 16 Mg-Mg and Al-Mg welded joints toughness percentage recovered with respect to that of the original un-welded metals and to process parameters

Finally, the same aluminum-low carbon steel samples mentioned in the first section (B. Microstructural characterization of friction stir welded similar and dissimilar joints) were tested in tension in order to evaluate their strength against the un-welded original metals. A tensile specimen was cut from each of the un-welded and welded samples according to ASTM-D198 standards and tested with a displacement controlled

rate of 1mm/min using a standard Hounsfield UTM H100KS model. Figures 17a and

17b show the stress-strain behavior of three original un-welded low carbon steel and

aluminum AA6061 samples, respectively. It was found that the ultimate stress in the low

carbon steel is 320MPa and that in AA6061 317MPa. Moreover, Figures 18 and 19

show the friction stir welded D4 (3mm thick) and C1 (2mm thick) samples respectively

with the corresponding tensile specimens cut from them for testing.

(a)   (b)
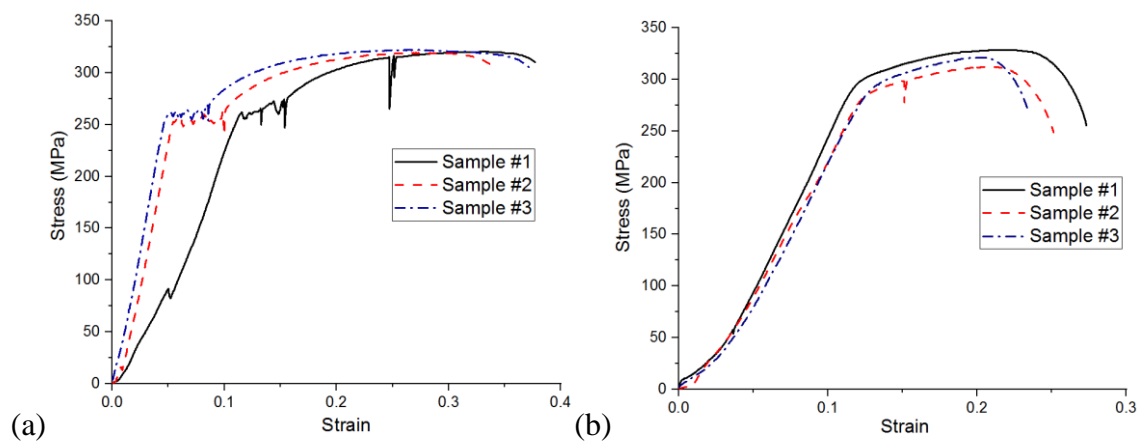
Figure 17 Stress versus strain of un-welded (a) low C steel and (b) aluminum AA6061.
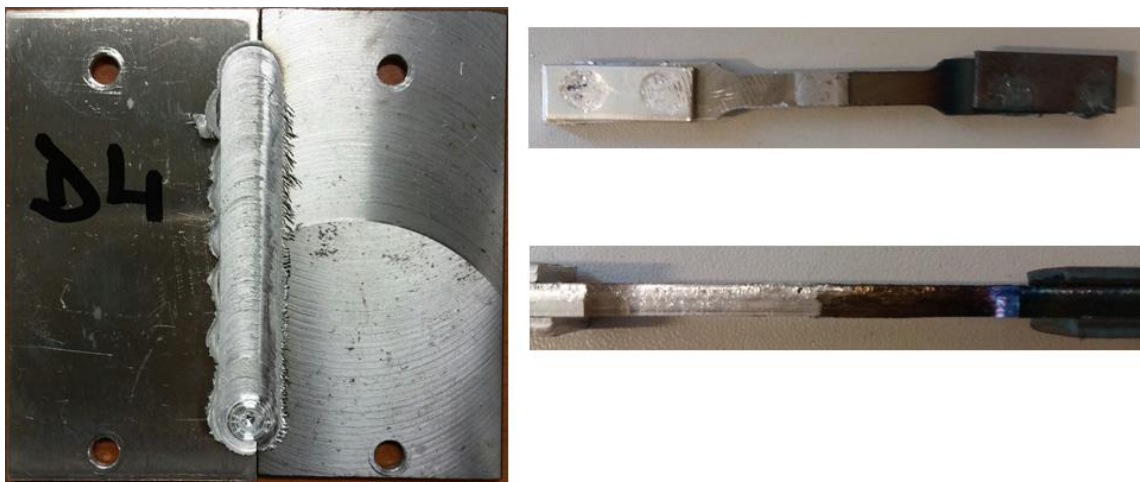
Figure 18 D4 sample after welding and after preparation for tensile testing

Figure 19 Sample C1 after welding and after tensile testing

Table 7 summarizes the resulting percentage of strength of the welded

specimens with respect to the un-welded material. Similarly, the stress-strain behavior

of these joints is shown in Fig. 20a and Fig. 20b for the 2mm and 3mm thick metal

sheets respectively. The behavior of the 2mm thick welded joints showed an increased

plasticity and a globally closer behavior to a regular ductile metal in addition to higher

strength when compared to the 3mm thick joints. The best results in terms of tensile

strength were obtained for the C4 sample which recovered almost 55% in strength of

both original un-welded materials (Ultimate strength =175.4MPa). As for the 3mm thick

samples the highest strength was obtained for D4 with a recovery of close to 47% of the

strength of the original un-welded metal (Ultimate Strength =148.4MPa).

Table 7 Percentage of the recovered strength of the Al-Steel friction stir welded joints
with respect to both un-welded materials

Sample #	Ultimate Stress (MPa)	% with respect to AA6061-Exp	% with respect to Low-C-Steel-Exp
D1	89.78	28.33	28.01
D2	90.78	28.64	28.32
D3	119.03	37.56	37.13
D4	148.44	46.84	46.31
C1	156.2	49.29	48.73

C2	172.65	54.47	53.86
C3	76.13	24.02	23.75
C4	175.37	55.33	54.70

(a)   (b)
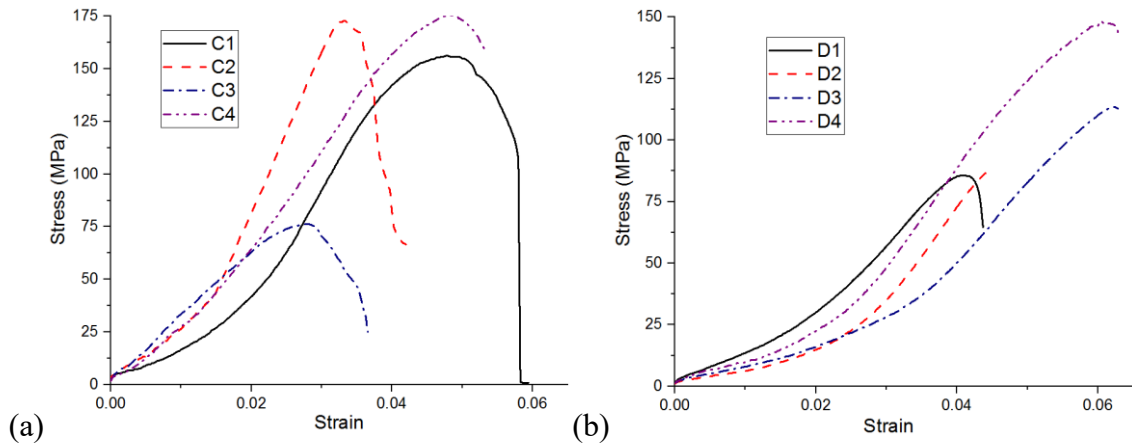
Figure 20 Stress strain plots of (a) 3mm and (b) 2mm welded Al-Steel.

The behavior of the Al-Fe welded 2mm joints showed better plasticity and an overall better behavior in addition to higher strength than in the case of 3mm joints. The sharp and brittle-like failure in the 3mm joints, shown in the stress-strain plots, presents the first remarkable difference between the behaviors of the samples welded using the HTS tool as compared to the Carbide tool. This would suggest either a lesser mixing between the two materials or a higher brittle intermetallic compound content in the weld line. These two assumptions were validated in the chemical analysis section.

D. MATERIAL FLOW ANALYSIS

On another hand, the material flow between the AS and RS during the FSW process was considered and investigated through the steel shot tracking technique [31,104] . This was also later on used for the comparison and validation of the finite elements model against the experiments. These experiments employed twin roll casted 3mm thick magnesium AZ31B plates measuring 45mm x 95mm. The concave and straight tools shown in Figure 5a and 5b are used for these experiments with a rotational

speed of 1200RPM and an advancing feed of 150mm/min for the two tests. Steel shots of 0.43 mm diameter were pre-placed in the advancing side magnesium plate according to the sketch in Figure 21. The same setup and embedding sketch was used for both tools, where a lone steel shot was placed at 20mm from the lower side of the plate and 1mm from the weld line which helps in understanding the post positions of the rest of the beads. At 30mm, 45mm and 60mm from the lower side, 6 steel shots were placed 2mm apart as of 1mm from the weld line until 11mm. The beads placed at 60mm were the closest to the surface (0.5mm from the surface) whereas the ones at 30mm were the deepest in the material (1.5mm from the surface). The beads at 45mm from the lower side were embedded 1mm deep in the plate. After placing the steel shots, the two plates were welded together at the previously mentioned process parameters.
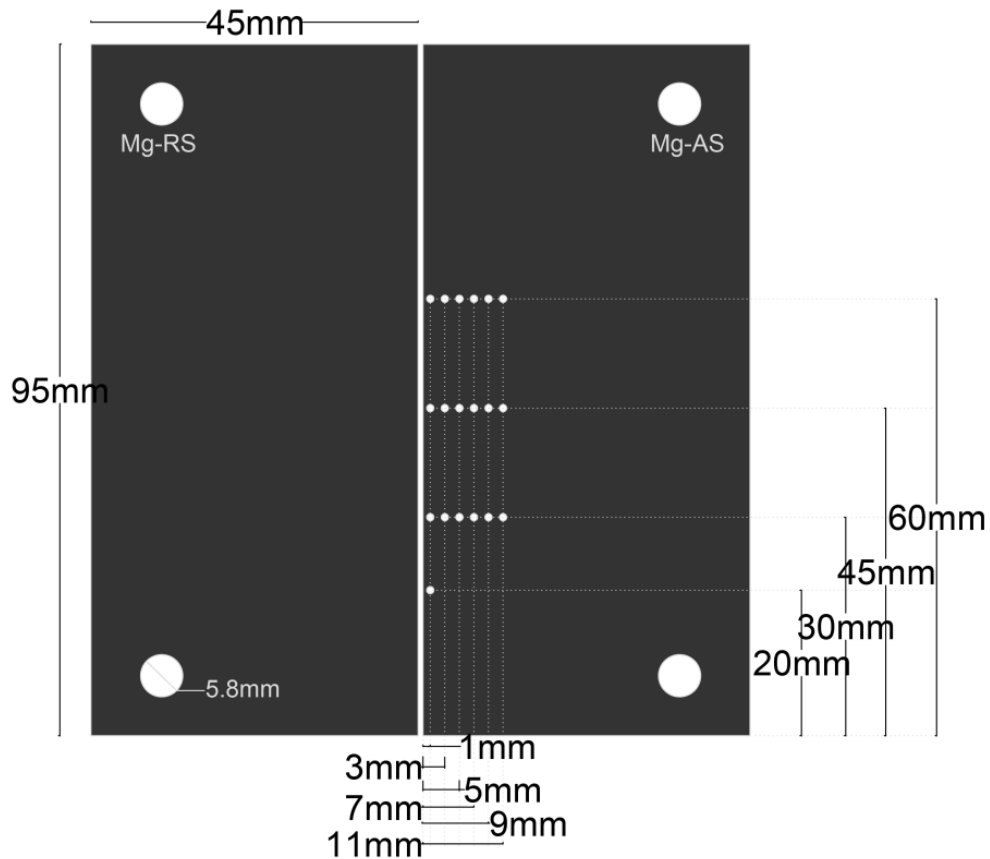
Figure 21 Sketch of the position of steel shots embedding

In Figure 23, the position of the beads (black dots) was obtained from commonly available X-Ray medical machines imaging of the sample and was compared to their position before the welding (white unfilled circles). The image of the equipment used in shown in Figure 22. The movement of these beads was evaluated as the total rotational angle for each of them which reflected the material flow and mixing that has taken place during the process. Figure 23a represents the experiment obtained using the straight tool and Figure 23b the one using the concave tool. In the case of the first experiment using the straight tool (Figure 23a), all the steel shots below the pin and the shoulder have moved considerably. Only those outside of the tool area (at 9mm and 11mm from the weld line) have not moved at all thus indicating that the area that has been plasticized is limited to the stirring zone (SZ) below the tool. In the case of the second experiment, using the concave tool, only the points that are on the path of the pin have moved. The flow below the straight tool is much greater than that below the concave tool which can also be noted from the angles (distances) by which the steel shots have moved indicating an over-engagement of the straight tool or otherwise an under-engagement in the concave tool. The area of contact between the shoulder and the plates is greater in the case of the straight tool. This increases the friction between the tool and the plates and the resulting temperature in the joints and leads to a smoother mixed material and thinner flow. Nonetheless, the concavity of the second tool and the tapered shape of its pin are also two factors that are thought to increase the flow of materials without increasing the temperature as much as the first type of tools. Moreover, in both experiments the effect of the tool shoulder and pin is aggravated at the surface and decreases gradually as the depth increases. The closest points to the weld line (1mm) undergo a doubled effect from the pin in a first place and from the shoulder afterwards.

This effect is even clearer in the case of the second tool where the tapered shape of the pin favors the flow near the surface which then gradually decreases with the increase of the depth.

Figure 22 X-Ray medical machine employed for imaging of welded samples

(a)   (b)
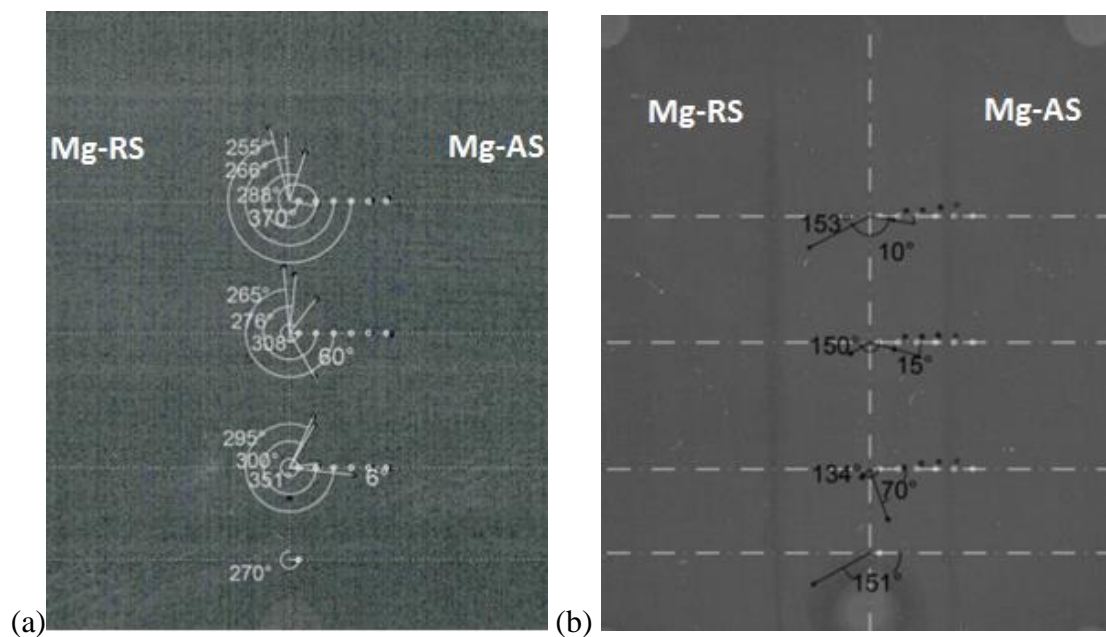
Figure 23 X-rays from experiments using (a) straight and (b) concave tools.

As a conclusion, it can be noted that the flow under a straight tool is larger than that under a concave tool, due to the increased temperatures generated by this geometry and from the large friction area and heat. However, the effect of a tapered pin is more

observable in the depth of a material leading to larger flow closer to the larger pin diameter which in this case is right below the surface.

CHAPTER VI

FINITE ELEMENTS MODELING OF THE FSW PROCESS

Many considerations have directed this research on the FSW process of dissimilar materials into numerical modelling and finite elements simulations. These considerations include the avoidance of long and costly experiments and the prospect of reading the different state variables that are normally difficult to read during the experimental analysis. In order to do so, finite elements (DEFORM 3D^{TM}) thermo-mechanically coupled model is proposed and measurable variables, such as temperature and volume fractions, are compared with the experiments for the sake of its validation.

A. FINITE ELEMENT MODEL SPECIFICATIONS

The model's components comprise of the tool, workpiece (WP), and backing plate (BP) such as shown in Figure 24. The tool and the BP are modeled as rigid un-deformable bodies since their yield stress is much higher than that of the WP. Both the WP and the BP were modeled as thin sheets with a 50x16 mm^2 surface area. Modeling the WP as two separate bodies is not feasible since it creates contact instabilities and issues in the convergence of the solution. Therefore, the WP is modeled as a single rigid plastic object in which two phases are defined, each on a side representing the two materials in the AS and RS considered for welding. Eight-noded tetrahedral elements are used to mesh the model components and active global re-meshing is considered for all three components. A size ratio of 5 and a minimum element size of 0.4mm are set for the different simulations. The tool and the BP contained 156000 and 20000 elements, respectively, at the start of the simulations. The workpiece on the other hand was divided initially into 126000 elements that were mostly concentrated in a meshing

window just below the tool and on the weld line. Outside of this zone, a progressively

coarser mesh was utilized.
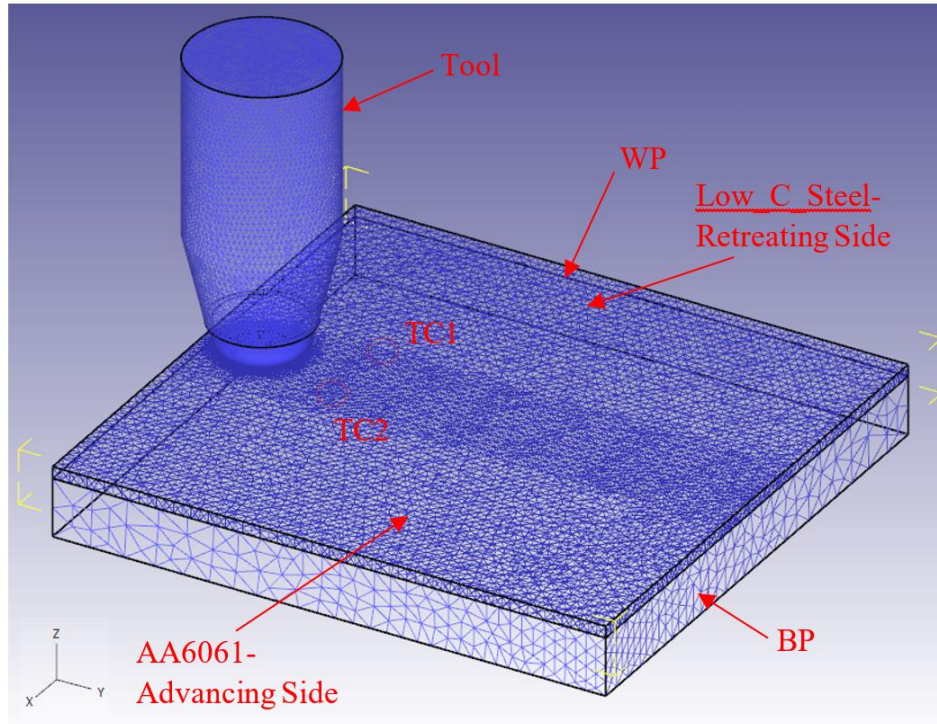
Figure 24 The FEM model showing meshed tool, workpiece (WP), and backing sheet (BP)

Reproduced in the simulation are the exact tool configurations and welding

process parameters (tool feed, rotational speed, tool offset, plunging depth, and tool

offset). The FSW tools used during all the simulations were drawn in CATIA and

imported into the simulation software Deform. Moreover, all of the simulations took

place in two stages: (1) plunging stage in which the tool drops progressively between

the sheets (in the –z direction) and (2) feeding stage in which the tool advances (in the y

direction) at the designated rotational speed and advancing feed. The simulation time

step was calculated based on the tool rotational speed and the minimum element size

such that the rotational distance traveled in each step does not exceed one workpiece

element length.

B. ALUMINUM TO LOW CARBON STEEL DFSW FEM

The proposed model is focused on the two Al-Low Carbon Steel FSW experiments which yielded the best welds in terms of soundness and strength and which were previously discussed in Chapter 1. The simulations specifics are discussed in details below.

As mentioned previously, the simulations and proposed model aimed to reproduce the exact experimental details employed in the FSW process. Therefore, the HTS and Carbide tools shown in Figure 5c and 5d (Chapter 1) were drawn in CATIA and imported for the respective simulation. Similarly, the process parameters indicated in Table 4 (Chapter 1) and recapitulated in Table 8 (Chapter 2) were also employed in the respective simulations.

Table 8 Combination of process parameters for aluminum-steel FSW joints

Designation	Speed (RPM)	Feed (mm/min)	Ratio	Depth (mm)	Offset to RS (mm)	Dwelling (s)	Thickne- ss of sheets (mm)
D4 (HTS)	1400	100	14	-2.88	0.25	15	3
C4 (Carbide)	400	100	4	-2	1	0	2

AISI-H-13 hardened tool steel (HTS) and carbide (tungsten carbide base) were assigned as the FSW tool materials. AISI H-13 hardened steel also assigned for the backing sheet. Due to numerical difficulties in having 2 separate plates being joined in the numerical simulation, the workpiece was assumed to be a one-piece with a mixture material formed from two phases namely aluminum alloy AA6061 and low carbon steel. Each of these phases is assigned to a side of the workpiece such as shown in Figure 25.
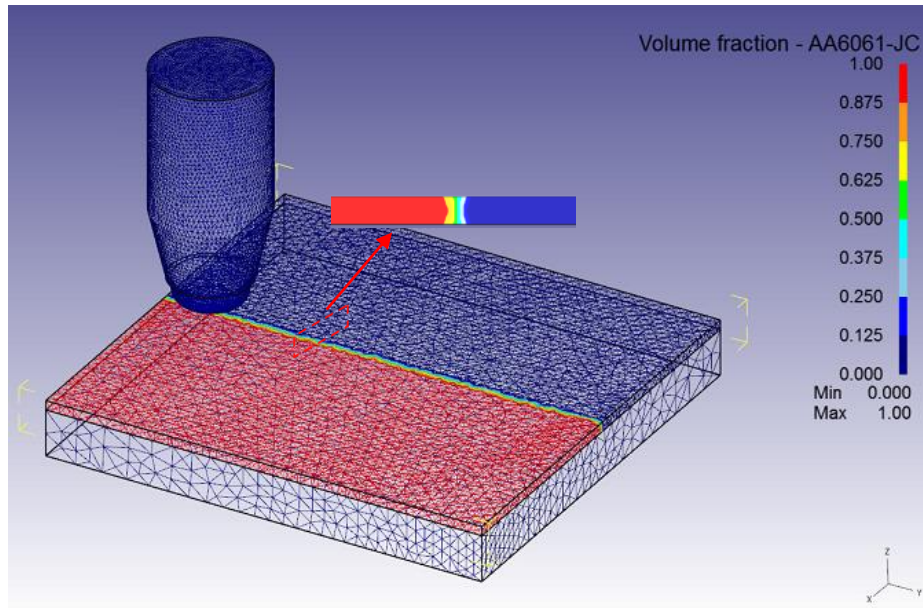
Figure 25 Volume fractions of the WP elements at initial step

The mixture material phase was considered as rigid plastic where the flow stress $\bar{\sigma}$ is modelled as a function of strain ε, strain rate $\dot{\varepsilon}$ and temperature T. The different materials available in the Deform library use tabular flow stress which are typically experimental data available in various handbooks and other sources such as in the work of Atabaki et al.[105], which describe the flow stress for each material as a function of temperature, strain and strain rate. The thermal and mechanical properties of low carbon steel (such as Young's modulus, thermal expansion, thermal conductivity…) given from the Deform material library are all a function of temperature whereas for the case of the aluminum AA6061 they were given as constants by defaults but were later on modified according to the values reported online [103] and by Al-Badour et al.[29] to better reproduce the material behavior at high temperature. A summary of the properties of all the materials used are listed in Table 9.

Table 9 Material properties

	Aluminum AA6061 (E-Funda) (Al-Badour, et al., 2013)	Low Carbon Steel (Scientific Forming Technologies Corporation, 2018)
Young's modulus E (GPa)	68.9	271$\rightarrow$69.4 T=-100$\rightarrow$1500
Poisson's Ratio v	0.3	0.3
Thermal Expansion (/ºC)	23.4E-06	1.08E-05$\rightarrow$1.49E-05 T=-100$\rightarrow$600(ºC)
Thermal Conductivity (N/sec/ºC)	180	41.7 for T=20(ºC) 43.4 for T=100 (ºC) 34.1 for T=1650 (ºC)
Volumetric heat Capacity (N/mm2/ºC)	2.4	2.91$\rightarrow$6.11 T=-100$\rightarrow$600
Emissivity	0.25	0.75
Mass Density (Kg/m^3)	2700	7800

The conductive heat transfer coefficient between the different components of the simulation was set at 8 kW/(m^{2}ºC) following an optimization of the value as proposed by Ammouri et al. [43] and recommendations of the range projected by Al-Badour et al. [29]. Convective heat transfer between the model components and the environment was considered. The environment temperature was set at 25ºC and the convective heat transfer coefficient at 0.02 N/sec/mm/ºC (default Deform value). Defining the friction coefficient in a finite elements simulation is a challenging task that takes into account several aspects including but are not limited to the value of this parameter and its type (shear, coulomb…). The variation of conditions of temperature, strain rate, and stress in the welded region adds to the challenges of defining the friction coefficient.

Considering that the workpiece is modeled as one object, only one friction coefficient was allowed to be defined between the tool and the WP in the inter-material boundary conditions although the WP contains two different materials (aluminum and iron). Al-Badour et al. [29] used a shear friction coefficient value of 0.61 which was decreased to near zero when temperature increased beyond 640°C. The effect of the friction coefficient was evaluated through several conducted simulations.

C. VALIDATION OF THE FEM VERSUS EXPERIMENTAL RESULTS

Temperature evolution and material mixing of the materials in dissimilar FSW joints are two key indicators of the soundness and reliability of the joints. Therefore, the effect of the configuration and tool/work friction coefficient on the evolved temperature profile in the aluminum and steel sheets and on the mixing between the two materials were investigated.

1. Effect of tool configuration and tool/work friction coefficient on temperature evolution in the FSW joints
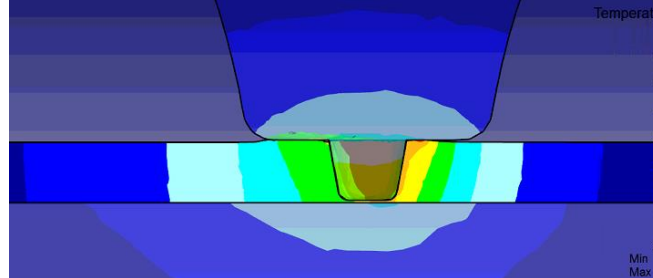
Temperature histories (profiles) were experimentally tracked using K-type thermocouples at the points of interest (Fig 24) placed during all the runs at the bottom of the sheets. Similarly following each FEM simulation, the temperature evolution profile at the FEM nodes corresponding to the thermocouples positions was tracked via post processing. The coordinates of these points are ±5mm from the weld line in the x direction, into both the advancing (aluminum) and retreating (steel) sides, respectively. Experimentally, the temperature was recorded as the tool traversed past these points during the welding process. To investigate its effect on the temperature profiles, the

77

friction coefficient values between the tool and workpiece was varied during the

numerical simulations between 0.3, 0.61, 0.9, and 1.2.

a. HTS tool

An example of the heat generation capability of the HTS tool for a friction

coefficient µ=0.3, is illustrated in Table 10. The tool/WP contact area was found to be

equal to 442 mm^2 and the heat flux in Al and Fe to 27 and 13.5 W/mm^2, respectively.

The table summarizes these results generated due to the combined effects of geometry

and friction while running at the process parameters listed in Table 8 with an illustration

of the distribution of the temperature between the tool and the WP.

Table 10 Contact area between HTS tool and WP and resulting heat flux in Al and Fe

	Contact Area (mm^2)	Heat Flux in Al (W/mm^2)	Heat Flux in Fe (W/mm^2)
	442	27	13.5

At the simulations' monitoring points and for the case of dissimilar welds using

HTS tool, the evolved temperature profiles obtained from FEM at different friction

coefficients versus those obtained from experiments in the aluminum and steel sheets

are shown in Figures 26a and 26b, respectively. The initial temperature in the

experimental setup was close to 50⁰C due to the succession of experiments and

therefore heating of the backing plate, however the initial temperature in all the

simulations was artificially set at 20⁰C. The two stage simulations (plunging and

feeding) are distinct in the slope of the heating curve in all the simulations. The slopes

of the heating curves, which correspond to the part where the tool is approaching the monitoring points, in case of both aluminum and low carbon steel, are sharp and steep as are the slopes of the experimental results. However, on the cooling side, the decrease in the temperature in case of the FE simulations happens much more rapidly than experiments which shows a progressive cool down in the two materials. This is most probably due the environmental condition of temperature applied in the simulation to the WP which acts as a heat reservoir during the process and which is not the case experimentally. It should however be noted that all curves converge toward almost similar final temperatures, 10sec after the start of the cooling process.
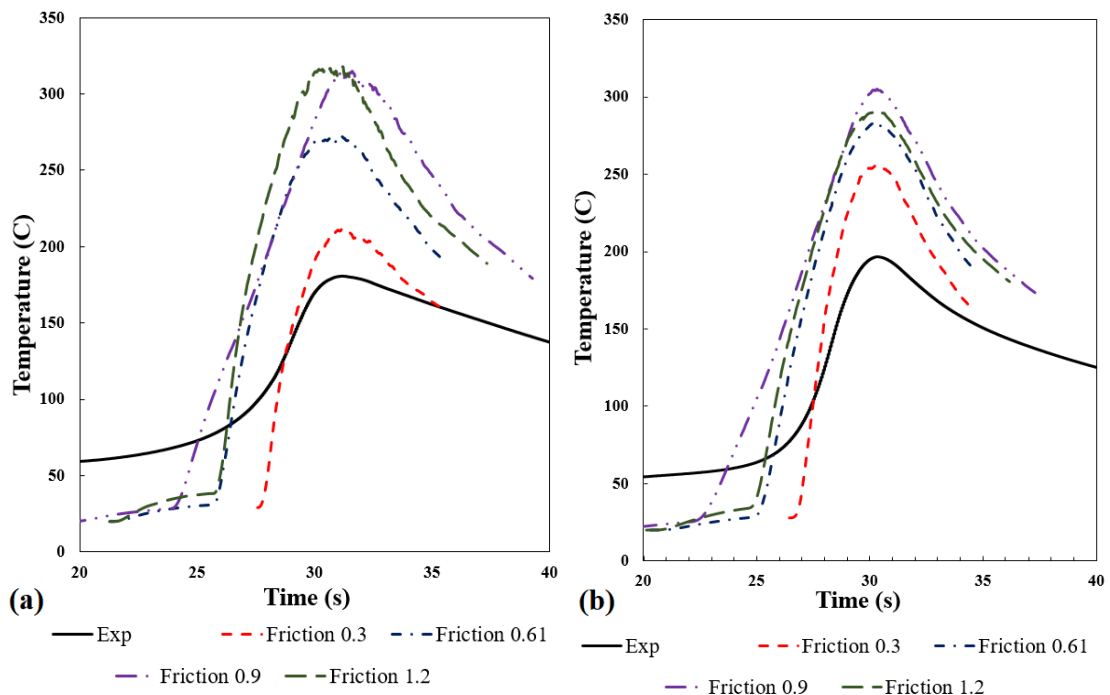
Figure 26 HTS tool: temperature profile comparison between experimental data and FEM results for different friction coefficients: (a) aluminum side and (b) low carbon steel side.

Figure 27 compares the maximum temperatures obtained from experiments versus those in the different FEM simulations as function of friction coefficient values for both aluminum and steel sides. The maximum temperature is found to increase with increasing friction coefficients in both materials. Comparing FEM simulations results to

experiments suggests a friction coefficient value equal to 0.3 would yield a reasonable error between the two techniques. This value of friction coefficient between aluminum and steel is half the value reported in the work of Al-Badour et al. [29]. For this friction coefficient value, the difference between the maximum temperature measured experimentally and in the FEM simulation is 31% on the aluminum side and 6% on the low carbon steel side. The overall increasing trend of the maximum temperature plateaus around μ=0.9.
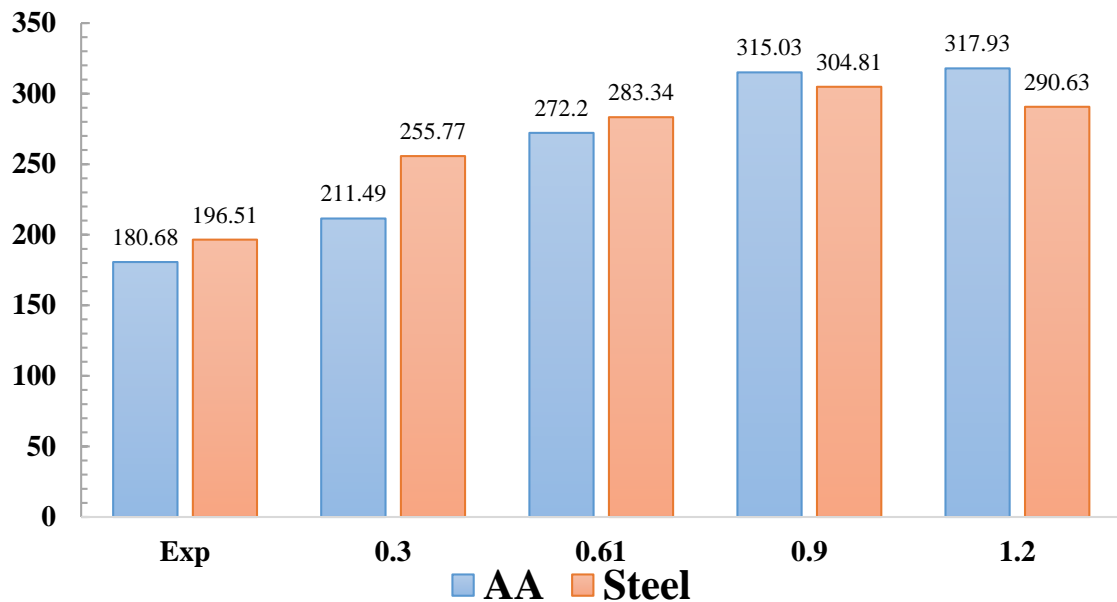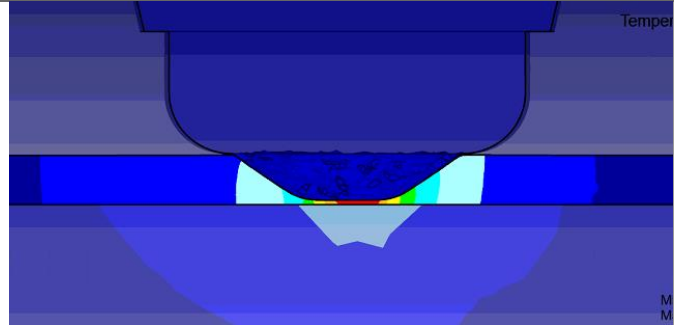
Figure 27 Maximum temperature observed in aluminum and low carbon steel at the monitored points versus friction coefficient values.

b. Carbide Tool

Similarly, heat generation capability of the carbide tool is shown in Table 11 alongside an illustration of the heat distribution in the tool and WP for a friction coefficient μ=0.3. This table lists the calculated contact area between tool and WP as well as the heat flux generated due to the combined effects of geometry and friction while running at the corresponding process parameters listed in Table 8. Under these

conditions, the carbide tool/WP contact area is found to be equal to 941 mm^2 and heat

flux in Al and Fe to 9.75 and 5.08W/mm^2, respectively.

Table 11 Contact area between the carbide tool and WP and resulting heat flux in Al
and Fe

	Contact Area (mm^2)	Heat Flux in Al (W/mm^2)	Heat Flux in Fe (W/mm^2)
	941	9.75	5.08

For the 2mm welded joint, the evolved temperature peaks at the FEM-

monitored points are plotted for the four different friction coefficient values (Figure 28).

Unlike the HTS tool, the carbide tool does not have a pin to penetrate between the two

materials making most of the heat generated from friction. The slopes of the profiles on

both heating and cooling sides for both materials are similar to those obtained

experimentally. One can also note the fairly flat appearance of the plots corresponding

to aluminum as compared with steeper profiles for the HTS tool in Figure 26.
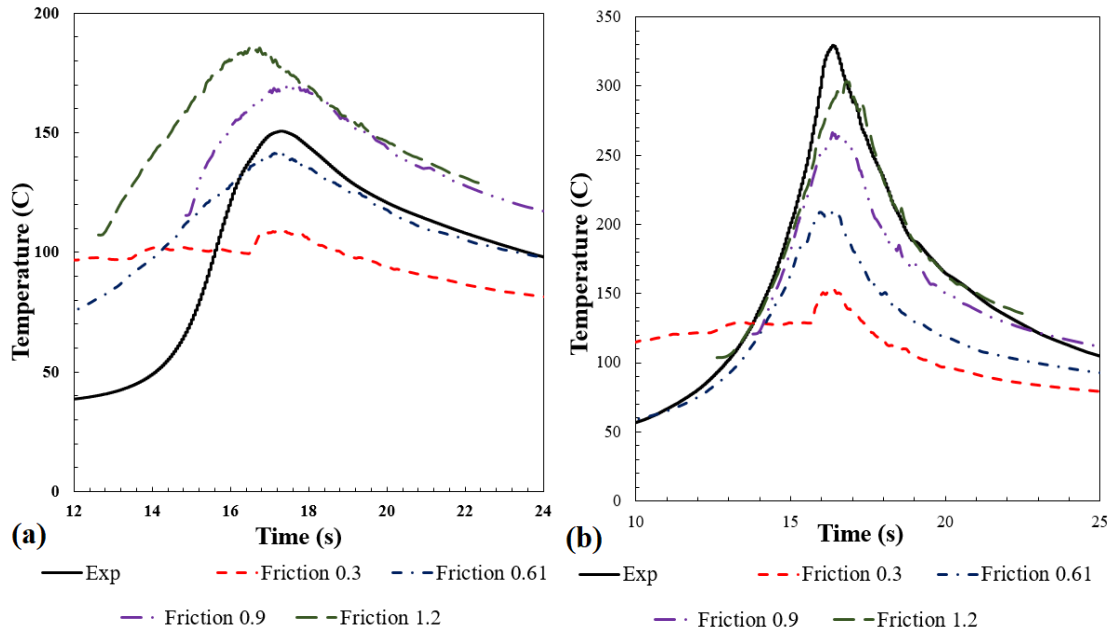
Figure 28 Carbide tool: temperature profile comparison between experimental data and FEM results for different friction coefficients: (a) aluminum and (b) low carbon steel

A large difference can be noticed in Figure 29 between the maximum temperature in the aluminum and in the low carbon steel. A compromise between these two values can be reached for a friction coefficient of 0.9 for which the error on the temperature reading is 13% in the aluminum and 19% in the steel sides.
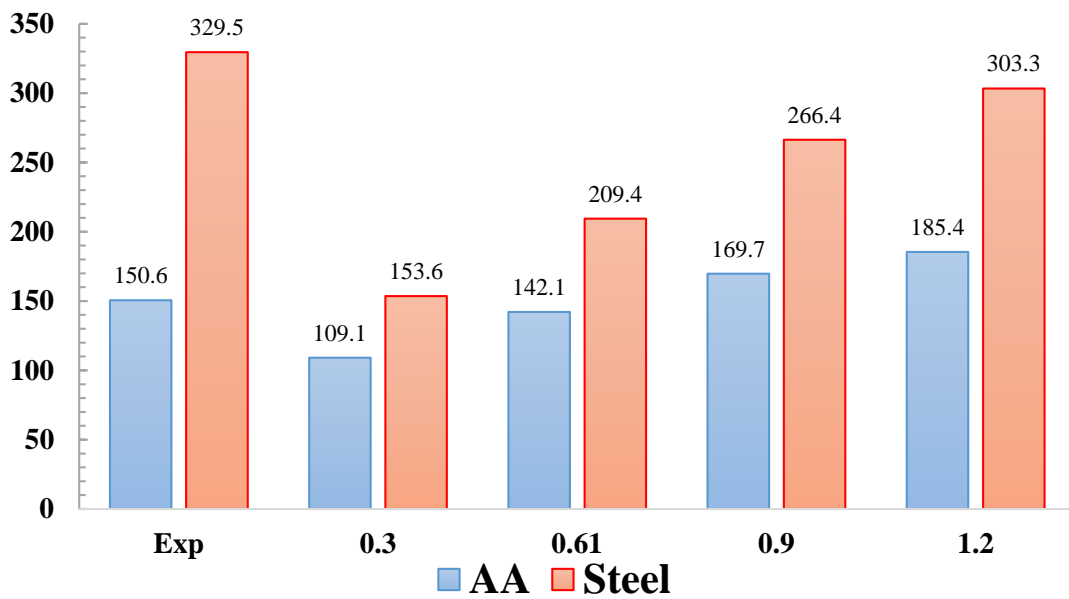
Figure 29 Maximum temperature observed in aluminum and low carbon steel at the monitored points versus friction coefficient values.

In conclusion, the smallest friction coefficient tested yielded the best results for the HTS tool which has a rather small contact surface versus the larger coefficient for the carbide tool which has the largest contact surface. This is again related to the geometry of the tool and whether a pin is present or not. When a pin was available, a small friction between the tool and the WP was enough to reach the temperature in the plates that would produce a sound weldment. To the contrary, the carbide tool without a pin relied much on the friction between the tool and the WP to reach the desired temperature in the plates. This is another time evidence that the mechanical work produced from the HTS tool compensates the work produced from friction and heat in the case of the carbide pinless tool.

2. *Effect of tool configuration on material mixing of the FSW joints*

The effect of tool configuration on the mixing between the aluminum and iron sheets are also investigated in the case of the 3mm thick joint welded using the HTS tool and the 2mm sample welded using the carbide tool. The experimentally collected elemental distributions of Al and Fe from EDX analysis (detailed in Chapter 1) are contrasted to those from the FEM simulations under the same conditions. For the FEM simulation, the volume fraction distribution was considered for the four friction coefficient values ranging from 0.3 to 1.2 similar to those used in the temperature evolution study.

The EDX analysis was performed on a 40mm wide sample that was cut from the welded sample midway through the length and the width of the original welded specimen. The experimental analysis was done on the first sample at three different positions in the cross-section (CS), namely top (P1), middle (P2) and bottom (P3) and at

two positions for the second sample namely upper half (P1) and lower half (P2) as referred to in Chapter 1.

a. HTS

The geometry of the HTS tool is superimposed on the D4 experimental and FEM samples to highlight the work generated and which resulted in the mixing (Figure 30). Three regions could be noticed from the FEM volume fraction image; the first region is the one outside of the tool limits which is composed of either the aluminum alloy or the low carbon steel purely. A second region is proposed below the shoulder of the tool, which is typically known as the heat affected zone (HAZ), in which a minor mixing can be noticed. This mixing is however limited to a maximum of 25% of one phase in the other according to Figure 30. Finally, the third proposed region is across the tool pin path and is the one in which most of the mixing occurs. Within this region, almost 50% of each phase can be identified.
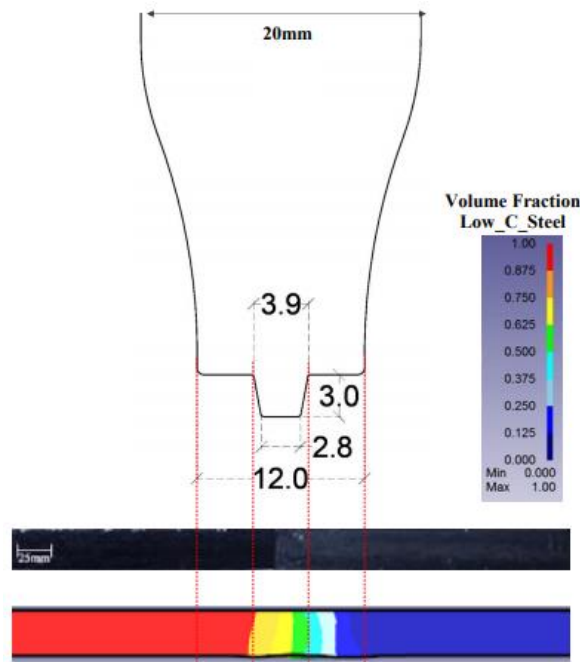
Figure 30 Volume fractions of the cross section of Al/Steel FSW D4 3mm-thick joint as obtained from FEM

The volume fraction distribution in these samples is reported in Figures 31 (a,b and c) from FEM and compared to the elemental composition of Fe and Al across the cross section as obtained from EDX. According to the FE model proposed, the change of the friction coefficient doesn't induce a major difference in the mixing between the two materials. The minor offset in the mixing towards the right of the pin (aluminum advancing side) was the only difference that could be noticed as the friction coefficient increased. This result is due to the higher sticking condition provided by the increase in the friction coefficient which allows the harder material to become more malleable and mix with the softer material. As previously mentioned, choosing a friction coefficient especially in the case of dissimilar FSW is a daunting task. The higher coefficient reflects better contact between the tool and the steel material, which is brought in the aluminum side although it is placed on the retreating side. However, it doesn't look as suitable for the contact between the tool and the aluminum which was not stirred in the steel side for mixing.

Experimentally, and as reported in Chapter 1, the mixing was found to take place at the left side of the pin more than on the right side, although many sites on the right side of the pin were also found to contain a mixture of both materials in all three EDX plots Figures 31 (a, b and c). This is the expected behavior of the materials in FSW whereby the material at the advancing side moves into the material placed at the retreating side. Additionally, the offset of the tool into the steel retreating side also contributed to this shifted joining in the weld. This could suggest an artificial volume fraction distribution produced by the FEM rather than an actual mixing resulting from the tool stirring action.

Additionally, the mixing was found to be more noticeable at the top and in the middle of the sample rather than at the bottom. This was equally found in the EDX experimental results. The activity of the concave threaded shoulder is thought to be the main reason behind this mixing action found in the upper part of the CS. At several points in the EDX profile, especially in the top and the middle, an important mixing is shown between Al and Fe every time the atomic percentage of each of these elements ranges between 40-60%. The same regions defined previously in Figure 30 can also be identified in the mixing profile provided by the EDX analysis. The first region outside of the bounds of the shoulder where no mixing is found. The second region below the shoulder in which some mixing could be noticed. It is limited to 20% on the right side of the tool (advancing side) but could be higher on the left side (retreating side) where the material of the advancing side is stirred in the material of the retreating side due to the action of the tool. Finally, the third region is below the pin and is where a mixture between Al and Fe is always obtained. The threads found in the pin and shoulder of the HTS tool contribute actively to the mixing of the two materials. Although the tip of the pin is a standard zone of high deformation, the fact that this region is very narrow does not favor the mixing in the bottom part of the sample which is noticed in the FEM CS as well as in the EDX profile of the bottom region.
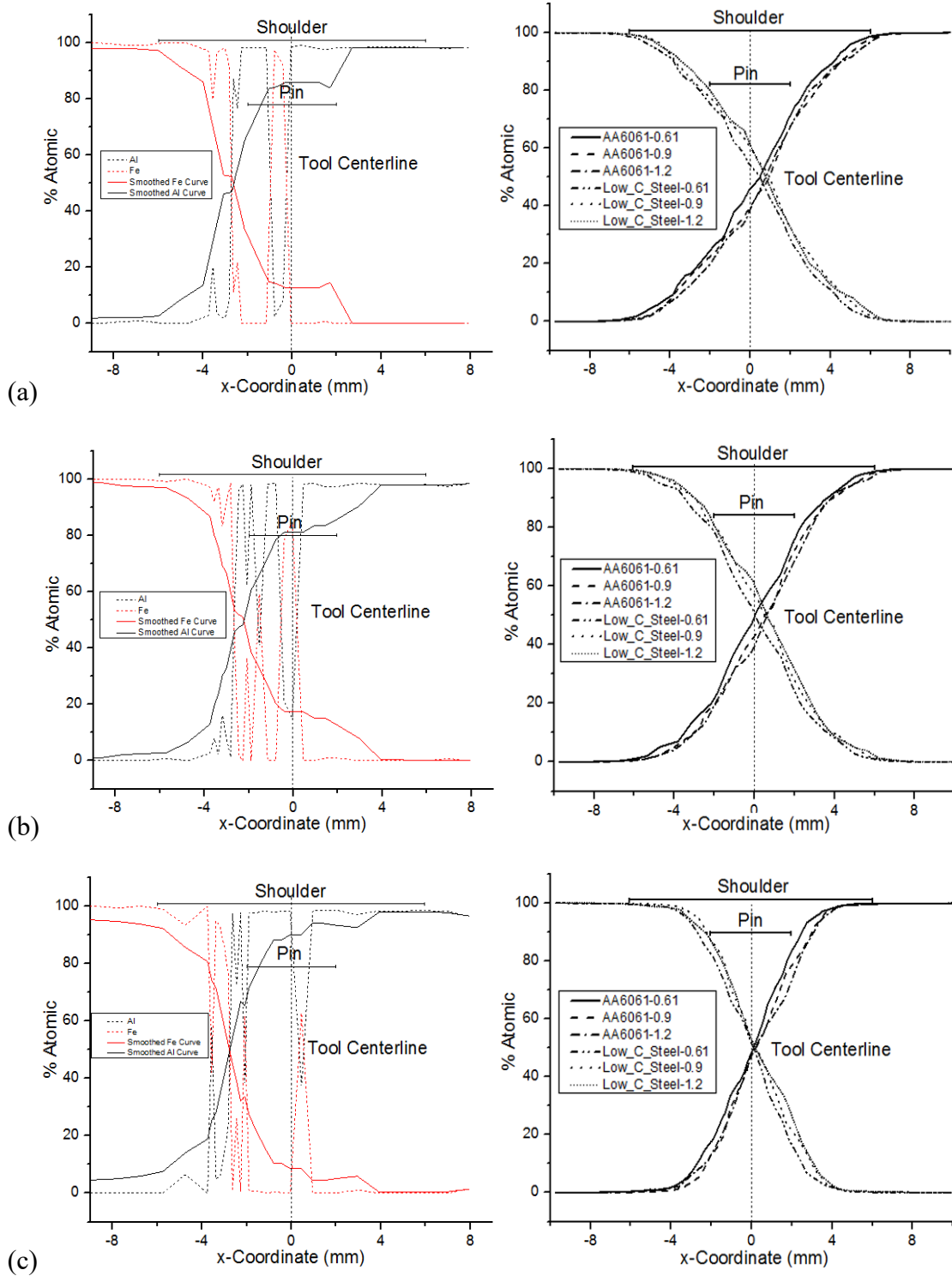
Figure 31 Al and Fe elemental compositions in D4 3mm sample at the (a) top, (b) middle, and (c) bottom as obtained from (left) EDX and (right) FEM, respectively

b. Carbide

In the case of the C4 2mm sample, the carbide tool which was used to produce this specimen has a convex, unthreaded shoulder and does not contain a pin. The tool geometry is superimposed on each of the samples (FEM and experimental) to highlight the work generated by the tool and which resulted in the mixing in Figure 32. The process parameters used for the production of this sample, include an offset of the tool of 1mm towards the retreating side (steel). The volume fraction distribution produced from the FEM shows that the large part of the mixing takes place below the shoulder of the tool, although its centerline is shifted to the left. A large tunnel to the right of the tool is distinct which could well be the consequence of the tool convex geometry. The material that is softened due to friction is circulated by the movement of the tool from the advancing towards the retreating side. Unlike this tool, when the shoulder is straight or concave, the material close to the weld line is kept in place and its movement on the surface closes the gap that results from the opening of the tool path.
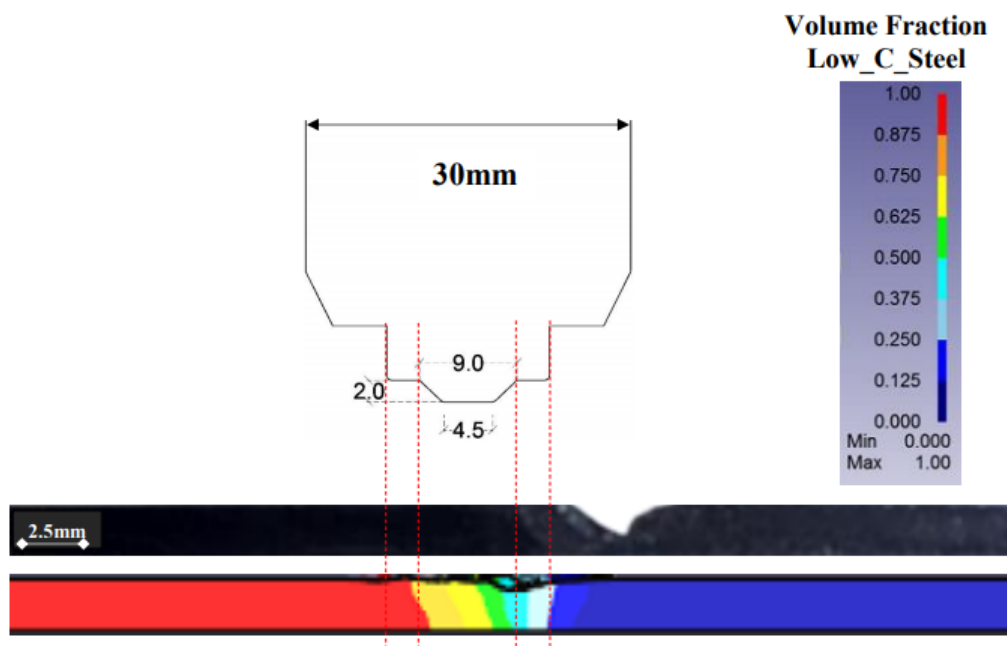
Figure 32 Volume fraction of the cross section of Al/Steel FSW C4 sample as obtained from FEM

Figures 33 (a and b) show the volume fraction distribution in the upper and lower parts of the CS of the sample, respectively. Similar to the first sample discussed above, the elemental composition in Fe and Al produced from FEM (Right) and from experimental EDX (Left) are also compared. It was again found that most of the mixing takes place in the upper part rather than in the lower part of the sample and is spread along 3-4 mm. For both plots (FEM and EDX) the mixing was more pronounced at the right side of the tool (advancing side). This result is unlike that found for the sample welded with the HTS tool and even unlike what FSW theory might suggest which could indicate a fundamental difference in the mixing mechanism between the two samples and more precisely the two tools. The most obvious difference between the two tools is the pin which is absent in the Carbide tool; this suggest that the majority of the work induced by this tool leading to most of the mixing is mechanical. The heat on the other hand, which is larger in the case of Carbide tool than in the HTS tool, was not enough to stir the material from the advancing side into the retreating side.

Moreover, once more the effect of the friction coefficient on the mixing is not very significant. In the FEM plots the mixing takes place midway between the two materials regardless of the position of the tool. This could also be evidence of an artificial volume fraction distribution which does not take into account the action of the tool especially that it does not contain a pin which tends to increase mechanical work between the two materials.
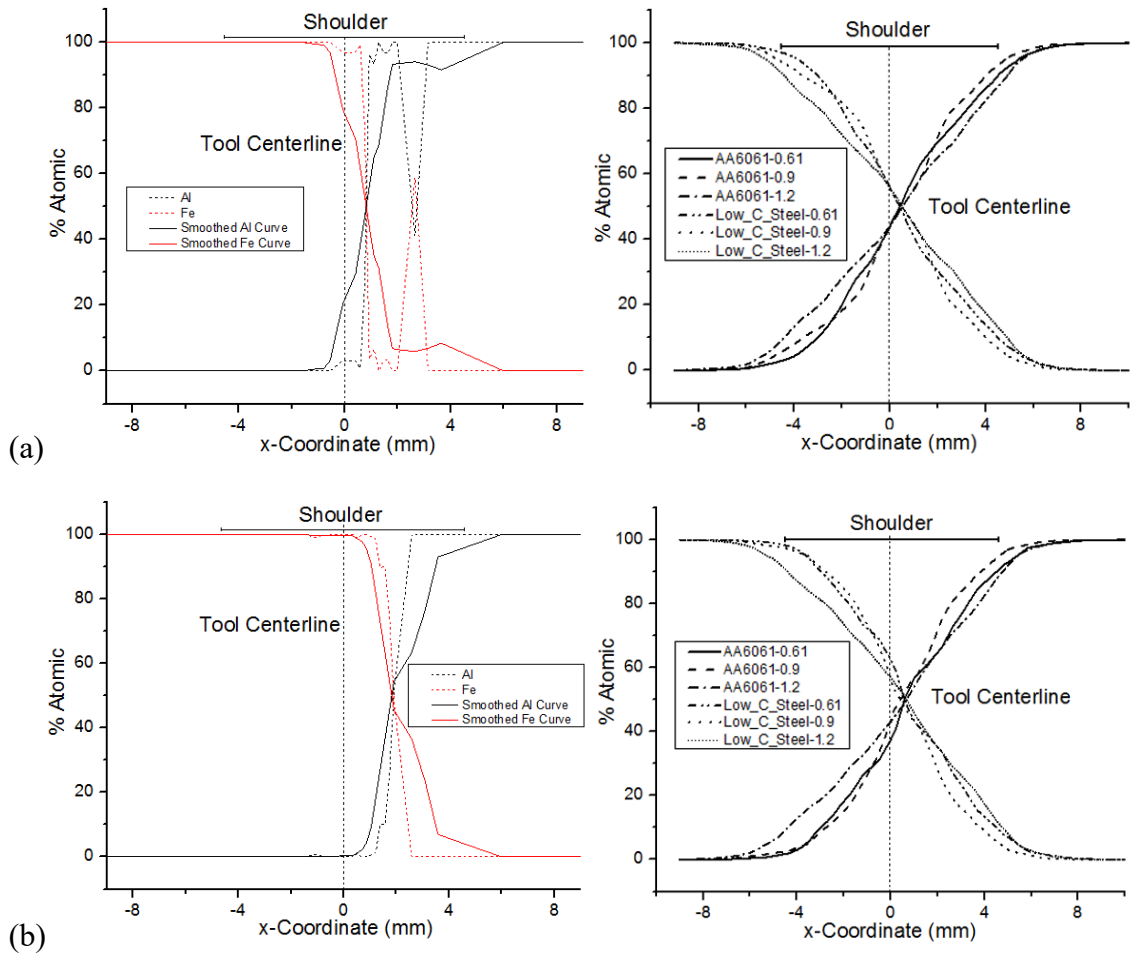
Figure 33 Al and Fe elemental compositions in C4 2mm sample (a) in the upper and (b) lower sections as obtained from (left) EDX and (right) FEM, respectively (values in legend refer to friction coefficient).
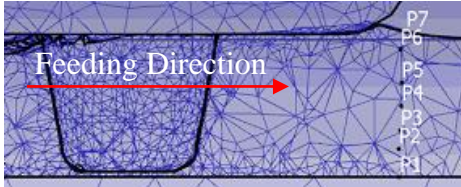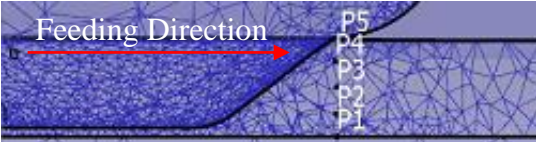
c. Discussion

Material mixing in the two samples was investigated and compared by tracking different point locations and movement in the weld line as the tool passed through them. This was achieved through the point tracking option available in Deform. 7 and 5 points were defined in the D4 and C4 samples respectively. These points were distributed every 0.5mm in the z-direction of the cross section of the samples with the intention of validating the theory of mechanical work induced by the pin versus its absence in the case of lack of a pin. A summary of the movement of these points is shown in Tables 12 and 13.

The geometry of the HTS tool which consists of the concave shoulder and the tapered pin aided the observed movement of the points in the D4 sample. Points 1 to 4 rotated about the threads of the pin before being brought down towards the bottom of the plate. Whereas points 5, 6 and 7 rotated about the threads of the pin and were kept roughly the same position in the z-direction due to the downforce applied by the shoulder. On the contrary, the 5 points tracked in the C4 sample where most taken from the bulk of the sample to the surface as a consequence of the convex geometry of the shoulder of the Carbide tool. As shown in the different images in the right column of Table 12, points 2 to 5 contoured the limits of the shoulder up until reaching the surface of the sample. This also explains the presence of the tunnel shown in Figure 32 above and the theory of the materials being pushed outside of the weld line.

The mixing profiles discussed previously largely favor the welding done by the HTS tool over the Carbide tool. This is due at the same time to the process parameters as well as to the geometry of the tool itself and the work of the pin combined to the concave shoulder which keeps the smoothed material close to the weld line instead of the convex geometry of the carbide tool which pushes these material further from the weld line.
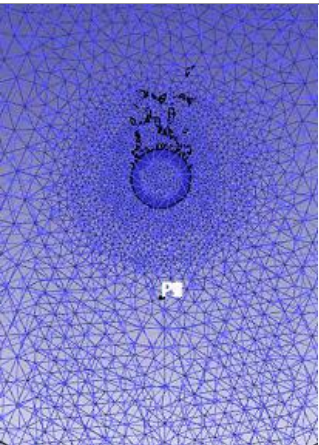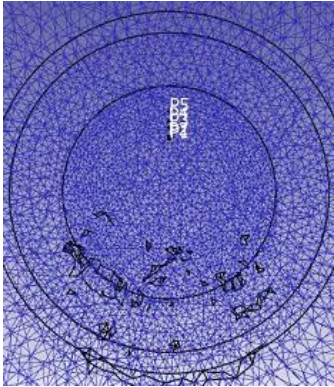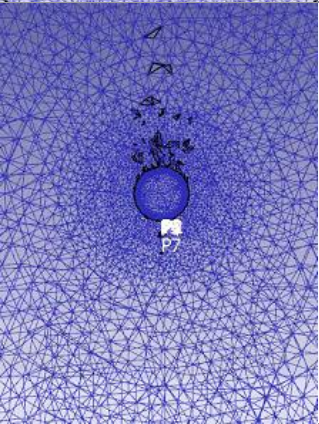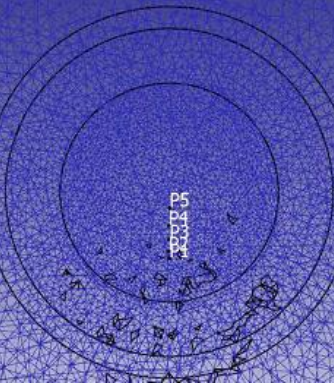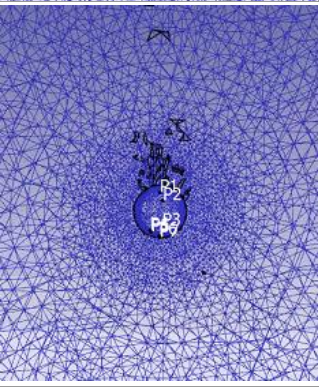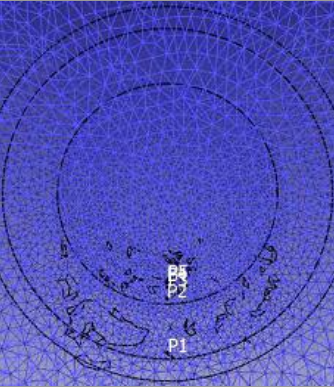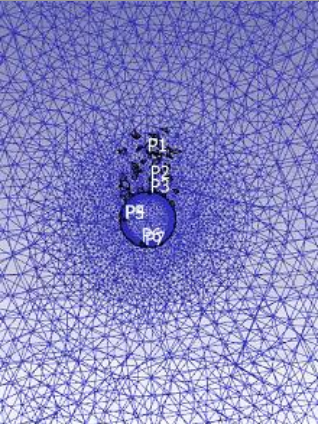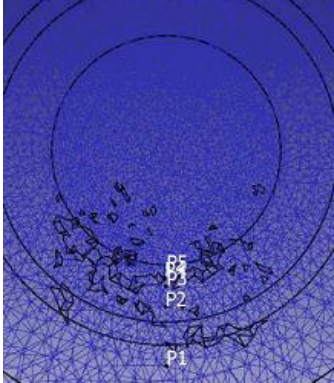
Table 12 Side view comparison of the tools behavior on the mixing in the WP

Step	HTS Tool- D4 Sample	Carbide Tool- C4 Sample
1		

Step	HSS Tool- D4 Sample	Carbide Tool- C4 Sample
2		
3		
4		
5		

Table 13 Top view comparison of the tools behavior on the mixing in the WP

Step	HSS Tool- D4 Sample	Carbide Tool- C4 Sample
1		

2				
3				
4				
5				

The intermetallic compounds are distinct compounds of predefined compositions normally formed following the FSW could not be evidenced from the FE model proposed. This is mostly due to the absence of continuous cooling plots for the mixture between the two materials chosen in these simulations namely aluminum and low carbon steel. The aim of such plots is to detect the resulting compound given the composition and the cooling rate. Moreover, even though the effect of the friction coefficient on the mixing was not clearly observed from the mixing profiles, its anti-proportional relation with the maximum temperature is perceived and elaborated in the first chapter. Finally, the main differences found between the experimental results and those obtained from the FEM are mainly due to the fact that the WP is modelled as one object composed of two materials. The sharp interface originally imposed at the first step of the simulation progressively disappears as the simulation progresses.

D. MATERIAL FLOW ANALYSIS

Another FE model is proposed to evaluate the material flow between the AS and RS in similar material FSW using two different tools (Figure 5a and 5b). This model is based on the experimental FSW of Mg-AZ31B reported previously in Chapter 1. Experimentally the material flow was tracked through the use of steel shots of 0.43 mm diameter which were pre-placed in the advancing side magnesium plate. On the other hand, a thermo-mechanically coupled FE model, also using Deform, is proposed through which the material flow is investigated using FE simulation and compared to the experimental results. In this model, a backing plate, a tool and a workpiece are included with both the backing plate and the tool modeled as rigid un-deformable bodies made of AISI13-H-Machining material and across which only heat transfer is accounted for. Meanwhile the workpiece was modeled as a plastic single plate subjected

to deformation and heat transfer. The material model for the workpiece was based on the Sellars and Tegart (ST) law which relates flow stress ($\bar{\sigma}$) to temperature (T) and strain rate ($\dot{\varepsilon}$) via the following equation [45,106]:

$$\bar{\sigma} = \frac{1}{\alpha}\sinh^{-1}\left[\frac{1}{A}\dot{\varepsilon}e^{\frac{\Delta H}{RT}}\right]^{\frac{1}{n}} \tag{1}$$

Where α, A and n are material constants, ΔH is the activation energy and R the universal gas constant. Table 14 summarizes the different parameters used in the modeling of this FSW process based on the work reported by Ammouri et al. [106]. In other reported work [45], the ST model was compared to the Johnson-Cook (JC) and Zerilli-Armstrong (ZA) models for FSP simulations of twin-rolled cast AZ31B. The ST model was capable of prediction the stress and temperature in the SZ eventhough the strain hardening was not perfectly reproduced in the HAZ where the strains have not yet saturated. The mixing and movement of the material around the tool can also be compared in the case of these three models in future work.

Table 14 Process Parameters in Deform for FSW AZ31B modeling [106]

Parameter	Rate
Young's Modulus	44830 MPa
Poisson's ratio	0.35
Coefficient of Thermal expansion	2.65e-05
Thermal Conductivity	96 N/(s.K)
Heat Capacity	2.43 N/(mm^2.C)
Emissivity	0.12
Material constant, A	27.5 s^{-1}
Material constant, α	0.052 MPa^{-1}
Activation Energy, ΔH	130 kJ/mol
Material constant, n	1.8

Also friction between the tool and the workpiece was set as a function of temperature according to previous research works of A. H. Ammouri et al. [106] ranging from 0.35 between 0°C and 630°C and 0.05 between 650°C and 1000°C. Figure 34 shows the meshed model with the straight-shouldered tool and the concave-shouldered tool respectively used in Deform. Mesh windows were used on the weld path below the tool, reducing the minimum element size to 0.001 and thus increasing the accuracy of calculation of the state variables.
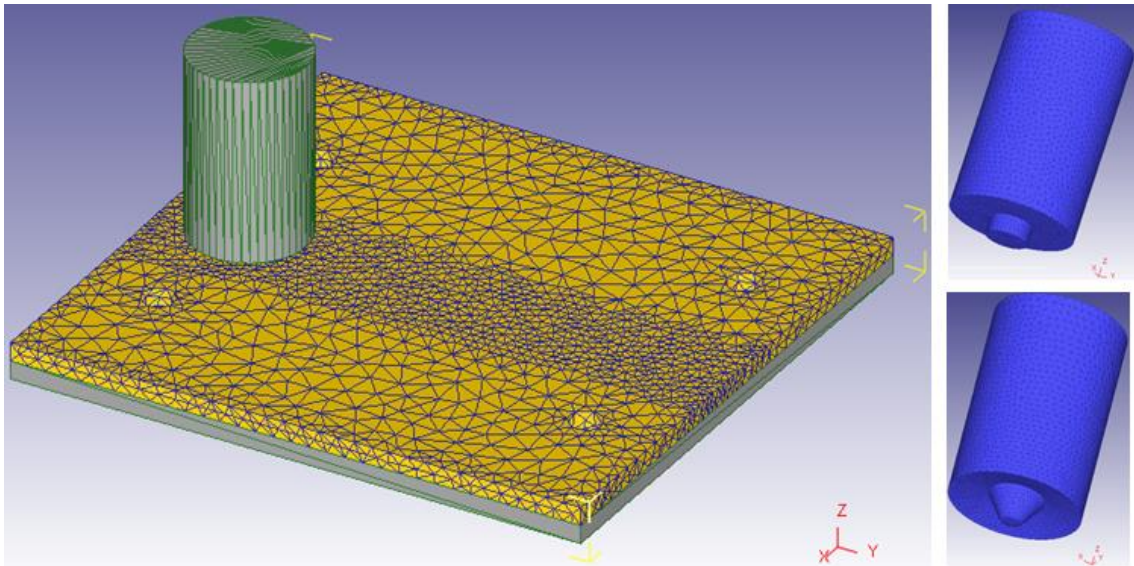
Figure 34 Deform meshed model with (top) straight and (bottom) concave tools

Using the point tracking option in Deform, it was possible to track the positions of several nodes before and after the passage of the FSW tool. These nodes represent the same positions of the steel shots pre-placed in the experiments that were placed the closest to the surface (0.5mm deep from the surface). The comparison between the experimental and FEM results for the process led by the straight and concave tool are shown in Figure 35 and 36 respectively.

Using the straight tool, it was found that the angular movement of the first two points (from the weld line) is reproduced more or less well enough in the FEM with

approximately 75% of the full turn. The third point experimentally also turned almost

295° whereas in the FEM it did not go around the tool and stayed in the AS. This could

be the result of the size of the mesh (in the tool and the WP) or of the distortion of this

mesh due to the movement of the tool at the interface between the two sides. On the

other hand, in the case of the concave tool, the movement of the steel beads was limited

to the first two (from the weld line) and is fairly reproduced by the FEM proposed. The

first point rotated approximately half of the full turn and the second 25% of the full turn.

The better reproduction of the material flow in the case of the concave tool is due to the

fact that this tool induces less distortion of the mesh across the weld line when

compared to the straight tool.

(a)

(b)
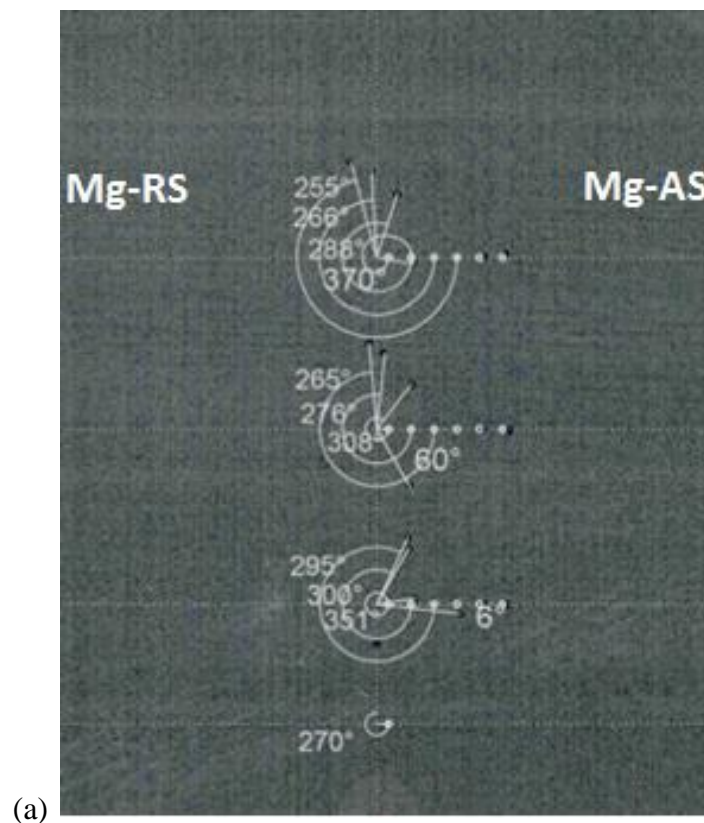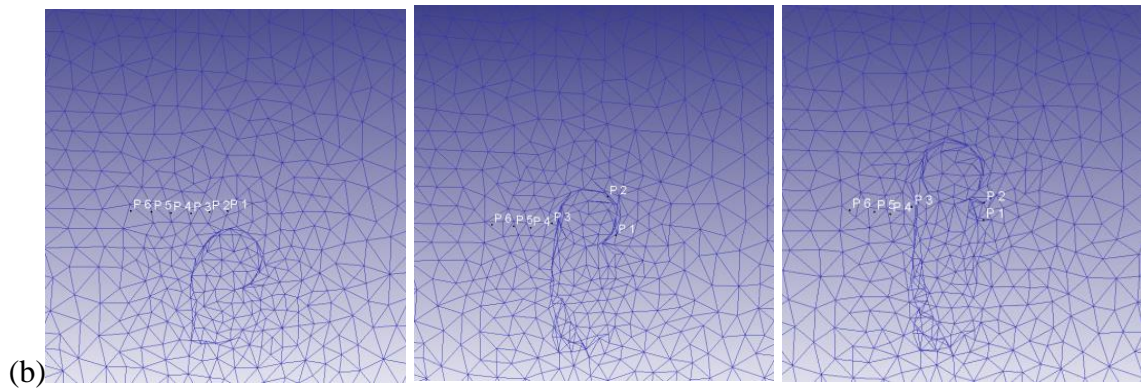
Figure 35 Comparison between experimental and FE simulated material flow in Mg-Mg FSW process using the straight tool

(a)

(b)
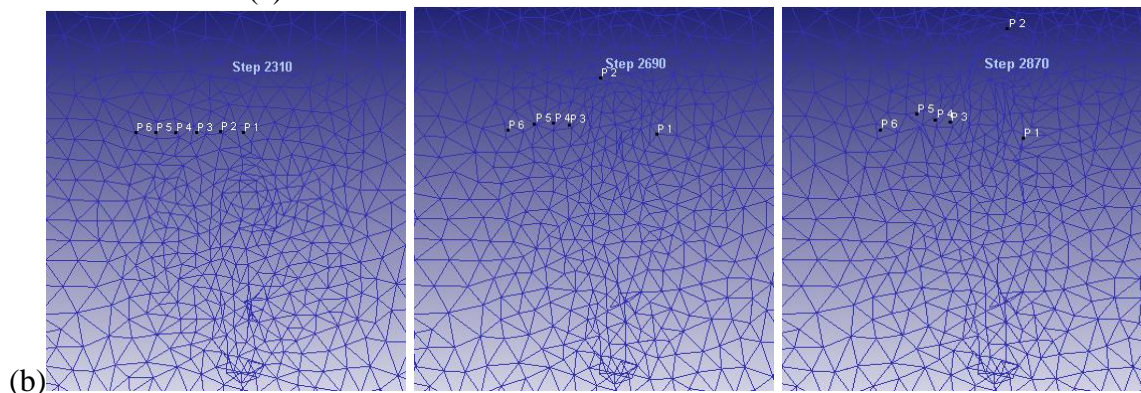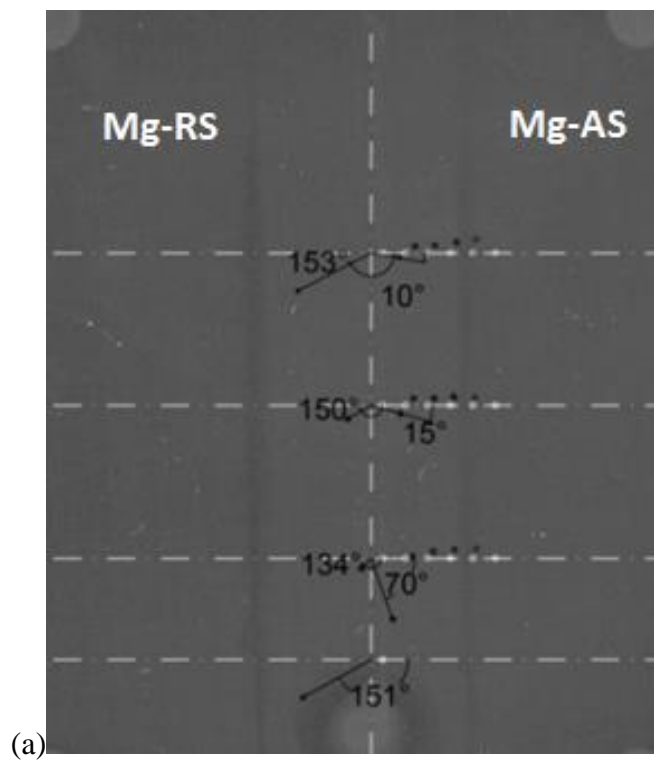
Figure 36 Comparison between experimental and FE simulated material flow in Mg-Mg FSW process using the concave tool

98

CHAPTER V

MOLECULAR DYNAMICS SIMULATIONS OF AN INTERMETALLIC COMPOUND FORMATION AT THE INTERFACE BETWEEN AL AND FE

Another aspect of the FSW process resides in the creation of the brittle IMC at the interface between the two welded plates. The mechanism of creation of these compounds was investigated at the molecular scale using Molecular Dynamics Simulations (MDS). The considered interface is formed from aluminum on one side and iron on the other. The mechanical response and interfacial mixing of Al/Fe system loaded in uniaxial compression at a constant strain rate of 5×10^7s-1 and five temperatures (150, 300, 500, 700, and 900K) was accounted for. During the simulations, the temperature was kept below the melting temperature of aluminum (~933K) so that stress assisted solid state mixing is examined. For that purpose, the accuracy of the Al-Fe.eam.fs potential was validated though static simulations of pure Al and Fe crystals separately. Then, the mechanical response of Al/Fe system under compression was simulated. The onset of nucleation of dislocations in both materials was observed shortly after relaxation.

A. METHODS

A prerequisite for intermetallic compound formation is material intermixing. Solid-state mixing in metals may be activated by high levels of mechanical stress and is accelerated by heat. Given mixing, and under conditions of temperature and pressure, intermetallic compounds are likely to form in interfacial systems. Such fundamental aspects of intermetallic compound formation can be studied via Molecular Dynamics (MD) simulations. This work investigates the mechanical response of a solid-state Al

99

(FCC) / Fe (BCC) bi-layer system under uniaxial compression loading (constant strain rate of $5x10^7$ s^{-1}) and five temperatures ranging from T=150K to T=900K (just below the melting temperature of aluminum). Also examined is the evolution of intermetallic compounds at this incoherent Al (FCC) / Fe (BCC) interface under same conditions. MD simulations utilizing Large-scale Atomic/Molecular Massively Parallel Simulator (LAMMPS) [102] are conducted. The Mean Squared Displacement (MSD) method is used to evaluate the resulting mixing of one element in the other (across the two regions of Al and Fe).

1. Setup

Figure 37 shows the simulation domain to consist of two regions each containing one of the two original elements: Fe (blue atoms, r_0=0.126 nm) or Al (red atoms, r_0=0.143 nm). The structures of both materials were arranged in perfect, defect-free lattice. The adopted interface is that of the Kurdjumov- Sachs (KS) Al/Fe such that the (111) Al plane is aligned with the (110) Fe plane as indicated in Figure 37 [59,62–64]. The difference in the crystal structures (FCC vs BCC) of the two materials leads to an incoherent Al/Fe interface. The large difference between the Fe and Al lattice parameters (a_0=2.867Å [107] and a_0=4.05Å [108] respectively) facilitates the creation of misfit dislocations [109]. The overall domain dimensions were obtained as a result of this crystal orientation as a x b x h = 10nm x 10nm x 23.7nm. The aluminum (atomic structure: FCC) region is defined over the entire spread of the xy-plane and ranging from -11.9nm to -0.1nm in the z-direction. The iron (atomic structure: BCC) region covers the entire xy-plane and ranging from 0nm to +11.8nm in the z direction. The model constitutes of a total of 12 aluminium lattices and 41 iron layers, leading to a total of 176226 atoms (103443 Fe atoms versus 72783 Al atoms) and during all

simulations, periodic boundary conditions were applied along the x, y and z boundaries
to ensure continuity of the system and repeatability of the simulation cell.
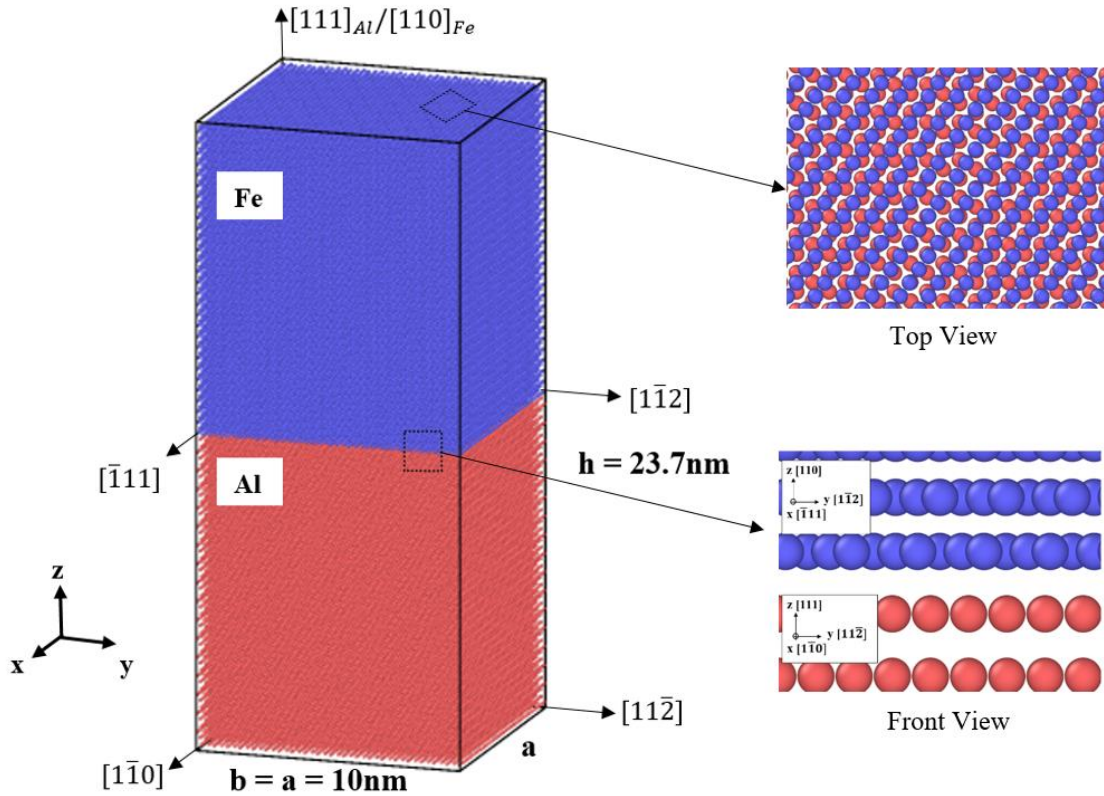
Figure 37 The simulation domain: Fe atoms (top; blue) and Al atoms (bottom; red)

All the simulations were conducted in three steps: (1) minimization phase,
originally intended to run a maximum of 50000 steps, was stopped by one of the
LAMMPS stopping criteria after the entire system energy was brought down to its
minimal value and thus the system brought to its most stable configuration, (2)
equilibrium phase in which a thermostat is imposed on the system thus taking it to
equilibrium at the designated temperatures (ranging between T=150K and T=900K)
over 150ps (or the equivalent of 30000 steps), and (3) loading phase in which a uniaxial
compression is applied in the z-direction at a constant strain rate of 5×10^7 s^{-1} over
4.500ns (or the equivalent of 1500000 steps). During this last step, the internal stress of

the system is computed in all three (x-, y-, and z-) directions. The stress strain plots as well as the resulting structure of the intermetallic at the interface were obtained using a timestep of 3fs in order to optimize the computational time.

2. EAM potential testing

The Al-Fe.eam.fs potential was introduced by Mendelev et al. [110] in order to describe Al-Al, Fe-Fe, and Fe-Al interactions. In their treatise of the embedded atom method, the total energy of the system is calculated as:

$$E_{Sys} = \sum_i E_i = \sum (F_\alpha (\sum_{j \neq i} \rho_\beta(r_{ij})) + \frac{1}{2} \sum_{j \neq i} \varphi_{\alpha\beta}(r_{ij})) \qquad (2)$$

where the system's total energy is the sum of the energies of all atoms. This per atom energy, E_i, is the sum of the embedding energy, F_α, (function of atomic electron density, ρ) and pair potential interaction, φ, summed over all neighboring atoms j of atom i within a cutoff radius value. This potential was found suitable for pure Al, pure Fe, and for the intermetallic compounds resulting from these two elements: Al_2Fe, Al_3Fe, AlFe, $AlFe_2$ and $AlFe_3$. All the possible crystal structures for each of the intermetallic compounds were considered when calculating the cohesive energy. The accuracy of this EAM potential was tested by performing static molecular simulations to obtain the elastic properties of pure Al and pure Fe [62] the findings of which compare favorably to those reported previously [111,112]. In this work, this potential was utilized under similar compressive loading conditions and thermostat and based on recently published work by the authors [113].

B. EVOLUTION OF MECHANICAL STRESS

For LAMMPS-simulated mixing and intermetallic compound formation in the Al/Fe system, several loading types and parameters were tested before deciding on the tests described hereafter. All simulations were conducted at temperatures below aluminum' melting temperature so that system constituents remain solid. The internal system stress as well as temperature was monitored during loading in both aluminum and iron regions. Figure 38a presents an evolved stress-strain diagram of the system subjected to uniaxial compression in the z-direction (at strain rate of $5\text{x}10^7\text{s}^{-1}$ and temperature of 700K). Initially, the mechanical response is linear elastic with a slope of 108GPa. The deformation is then accommodated plastically via different mechanisms of dislocation nucleation and growth in both materials. Given that the system is taken into the loading phase with the pre-existing misfit dislocations observed as of the very first steps after equilibrium (Figure 38b-I), plastic deformation is expected to take place at a stress level lower than what would have been the case without the presence of these misfit dislocations. The first noticeable plastic relaxation seen on the stress-strain plot occurs at approximately 4.7GPa corresponding to the nucleation of partial ⅙<112> dislocations on the (111) plane (Figure 38b-II). Employing the dislocation analysis tool provided by OVITO, the significance of relaxation points becomes apparent upon post-processing the simulation results. The loop expands into the bulk of Al leading to a minor drop in the stress to 4.4GPa (Figure 38b-III). In agreement with the findings of Zhang et al. [114], the nucleated partial loops appear to emit from misfit interfacial dislocation sites (considered as high distortion sites). Expanding partial loops encounter another interface on the lower surface where their mobility is hindered. The system then undergoes pronounced strain hardening with almost constant dislocation density until a

stress of 7.2GPa is attained. At this level of stress, bulk nucleation is detected in Al and significant drop in the stress to a value of 3.9GPa is encountered indicating a proper relaxation mechanism associated with yielding in the FCC aluminum (Figure 38b-IV). Following the stress relaxation to 3.9GPa, strain hardening ensues. Dislocations multiplication in the FCC crystal combined with an incoherent interface (obstacle to dislocations motion), induce hardening of the crystal. This is generally detected by system stress increase up to a critical stress value in the BCC constituent where dislocations start nucleating. This hardening is also related to the types of dislocations found in this region which contain a rather significant amount of junctions and jogs (highlighted in Figure 39a). At stress of 6.9GPa (strain approximately 11.2%), nucleation in the Fe region progresses emanating from the interface (Figure 38b-V). This is accompanied by a large increase in the dislocation density. It appears that the dislocations in Fe are predominately extended straight lines of predominately screw character. These extended dislocations annihilate after their brief appearance and shortly before yet another hardening behavior given their opposite Burger's vectors. This multiple relaxation followed by strain hardening dominates at all temperatures reflecting the same underlying mechanism of misfit dislocation movement followed by nucleation in Al followed by interface nucleation in Fe and annihilation. A similar stress-strain behavior was reported by Yang, et al. [115] for multi-layered Ti/TiN system where 3 peaks were observed: the first was shown to correspond to full dislocation dissociation into two partials whereas the second and third peaks correspond to yielding in two layers, respectively. Dislocations nucleation occurs in the more compliant material of the two (Salehinia, et al. [116]), here it is the aluminum constituent.

(a)
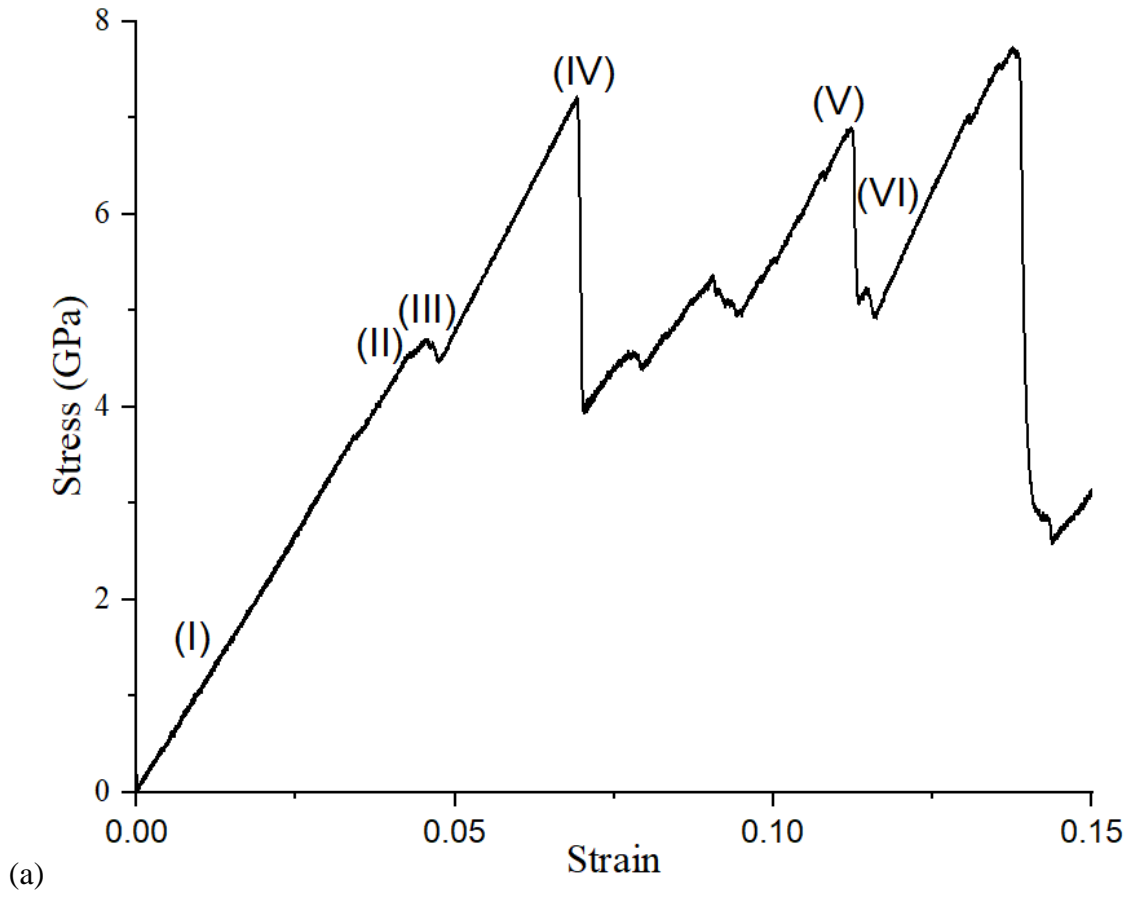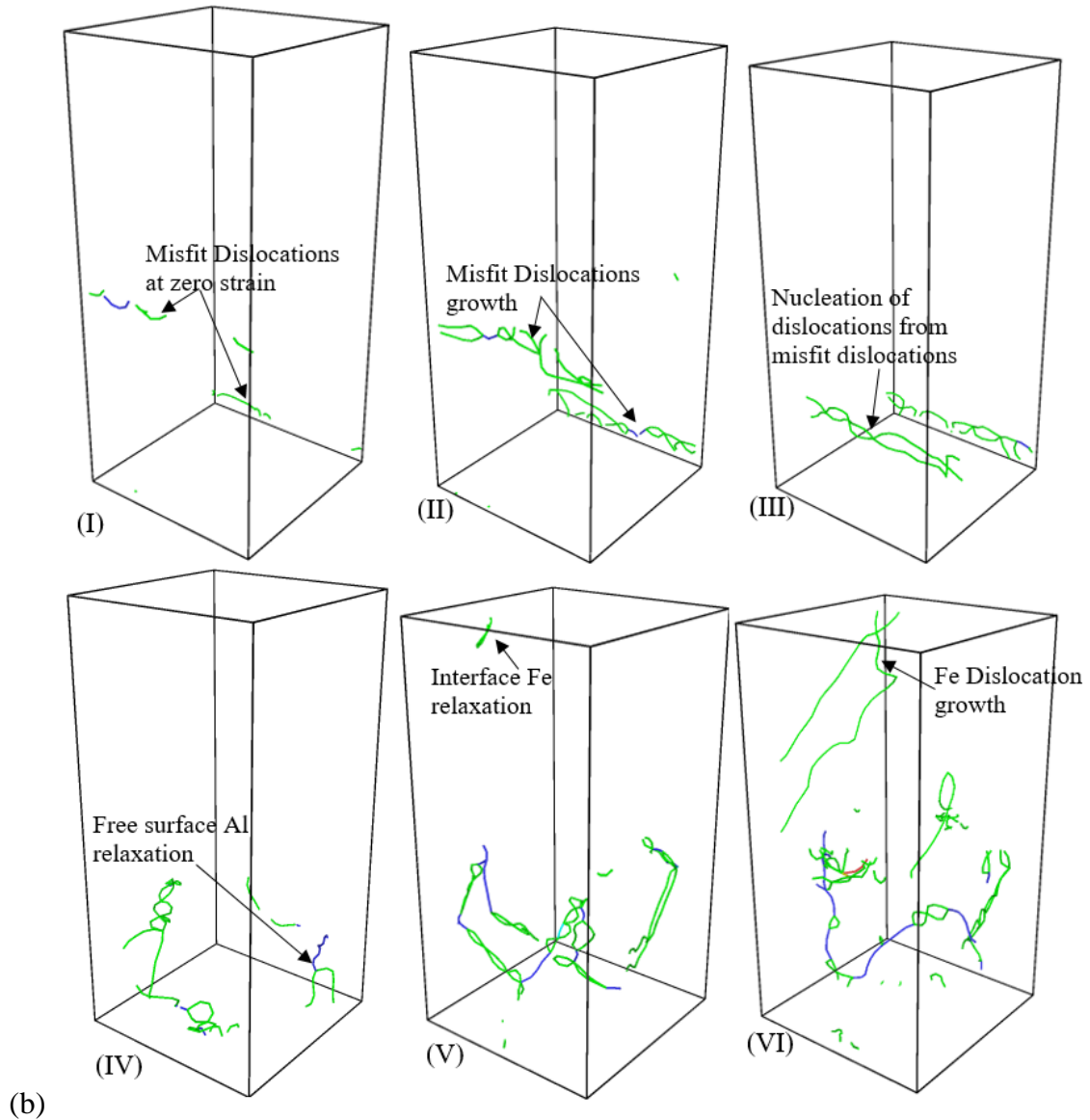
Figure 38 (a) Evolution of Al/Fe system stress (GPa) (Left Y-axis) and temperature (K) (Right Y-axis) versus strain during uniaxial compression at T=700K. (b) The different drops in the stress seen on the plot correspond to the different relaxation mechanisms in the two regions of the system such as movement of the misfit dislocations and nucleation of dislocations. This is accompanied by a minor and transient temperature increase.

Dislocations found in the FCC crystal are of different types at each step of the simulation; edge, screw and mixed dislocations are present. Most are found to be Shockley partials with a burgers vector equal to $\frac{1}{6}\langle 112 \rangle$. Other types of junctions and jogs were detected including few perfect dislocations with a burgers vector equal to

$\frac{1}{2}\langle 110\rangle$ (Figure 39a). However, in the case of the BCC crystal and as the stress

increases, it is observed that edge components of the nucleated dislocations in Fe move

at high speeds leaving behind trails of extended screw lines. The dislocations in Fe are

found to have nucleated on the {110} family of slip planes along the $\langle 111\rangle$ direction

(Figure 39b). The extended screw microstructure is commonly observed in BCC metals

deformed below certain temperatures (for iron this temperature is $T_c\sim340K$, defined as

the critical temperature at which the flow stress becomes insensitive to the test

temperature and screw and edge dislocations have the same mobility) [55]. Albeit in

small density, an unusual dislocation type with a burgers vector in the <100> direction

is identified at the free surfaces of the BCC iron and at the interface. This slip system

was also detected by Talaei et al. [117] upon indenting an Fe bi-crystal. This direction is

not a recognized slip direction in BCC metals but is likely the result of a junction

between two perfect gliding dislocations [118].
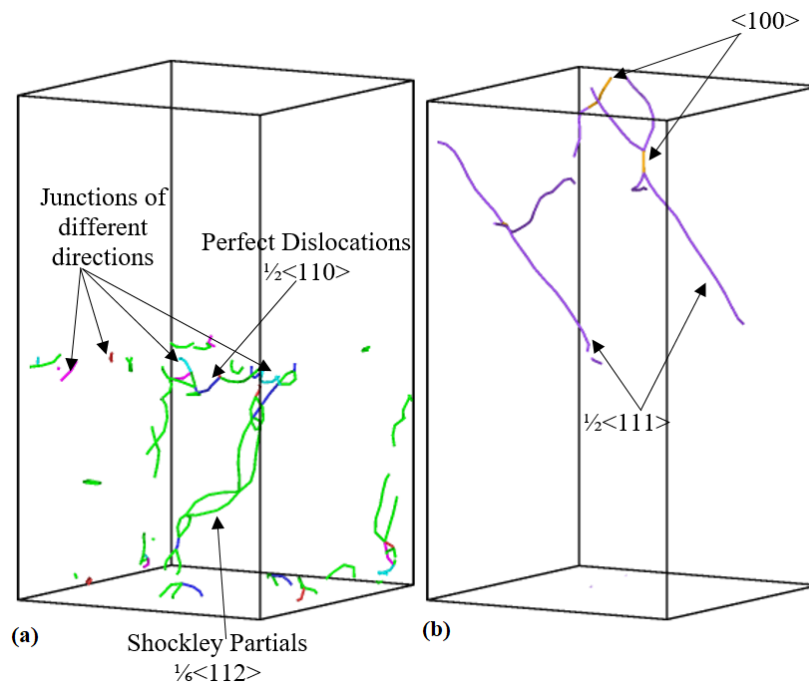
Figure 39 Perspective view of the different dislocations types in the (a) FCC (at 8% strain) and (b) BCC (at 15% strain) regions of the system at T=700K

C. TEMPERATURE EFFECT ON EVOLVED STRESS

The system is mechanically loaded at temperatures ranging from T_1=150K ($<T_c$) to T_5=900K ($<T_m$) including T_2=300K, T_3=500K and T_4=700K. Figure 40 illustrates the effect of temperature on the values of key evolved stresses obtained from the stress-strain curves, namely: (1) interface nucleation stress in aluminum, which seem to emanate from misfit dislocation sites when present, (2) bulk nucleation stress in aluminum, and (3) interface nucleation stress in iron. Multiple striations are observed for all temperatures demonstrating the multiple dislocation nucleation and movement mechanisms in both materials. These striations can also be explained by the presence of the incoherent interface which acts either as a sink or as barrier to dislocation movements [109,119]. For all temperatures below 900K, coherency stresses were observed on the stress strain plots and are reflected in misfit dislocation observations (via OVITO). At 900K, the stress at zero strain starts from zero due to thermal agitations at temperatures approaching aluminum melting. Dislocation transmission is another phenomenon observed at this temperature (expected observation especially using this specific crystal orientation). After bulk nucleation takes place in aluminum, dislocations are found to cross the interface into the iron region aided by thermal agitation and mechanical load.
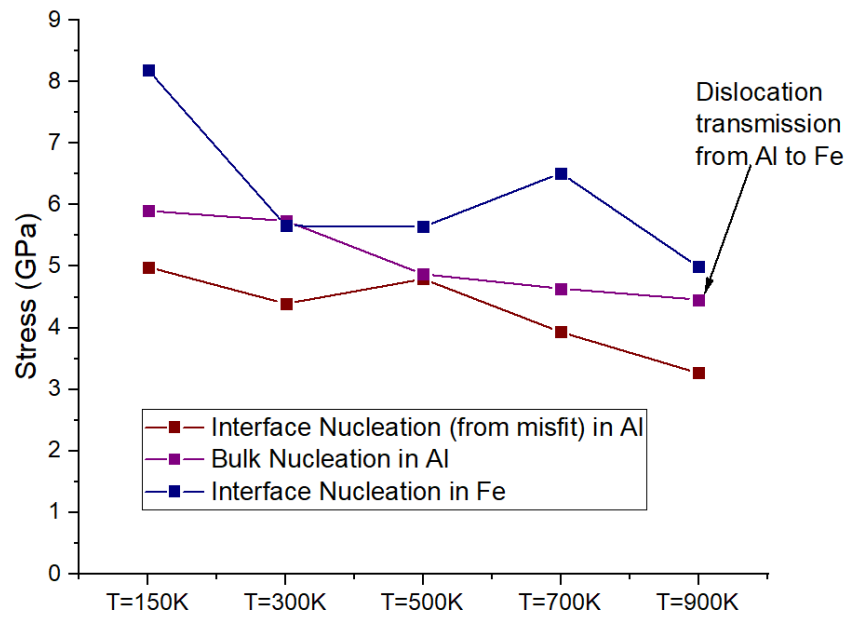
Figure 40 Effect of temperature on the Al/Fe system stress strain curves. Stress drops correspond to different relaxation mechanisms in the interface system.

The stress required to initiate dislocation nucleation and movement in the iron crystal at low temperature is expected to be large in order to overcome the large lattice friction which is strongly sensitive to temperature [120–125]. As temperature increases, the magnitude of lattice friction decreases. This is partly the reason behind the decrease of yield point associated with nucleation of dislocations in the BCC Fe. Temperature increase in BCC iron is also associated with an increase in phonon drag [46,126–129]. These competing phenomena, namely the softening behavior due to a decrease in nucleation barrier and lattice friction and the hardening behavior due to the increased phonon drag, result in the overall weak temperature sensitivity of yielding behavior in Fe above the critical temperature defined as 340K. Similarly, the relaxation stress, associated with dislocation nucleation in the FCC aluminum region, from the misfit sites as well as from the bulk, also decreases with increasing temperature [115]. This is largely attributed to the effect of thermal fluctuations in the crystal which facilitates the nucleation of dislocations and their movement. The mechanical contribution to the

energy barrier is compensated by the thermal energy. Finally, the interfaces and their types have been shown to play a major role in strain hardening and strain hardening rate as they were found to increase in incoherent interfaces [59].

D. INTERFACIAL MIXING

Interfacial mixing of Fe and Al atoms is studied at several temperatures using the Mean Squared Displacement (MSD). This method indicates the displacement, in the x, y, and z directions, of Fe (or Al) in a predefined region which will be referred to herein as the close interface. This displacement is perceived on the MSD plots (Figures 41a and 41b) as a straight line following the start of mixing between the two regions which is associated with the minor overshoot shown in the plots. This close interface region contains the first 7 layers of Al and 7 layers of Fe away from the interface. System temperature ranges are selected to range from 150K to 900K to ensure solid-state mixing. The simulations ran for a total time of 4.5ns at the designated strain rate of 5×10^7 s^{-1}. In Figures 41, displacements are reported on the y-axis in angstroms (Å) versus strain.

(a)

(b)
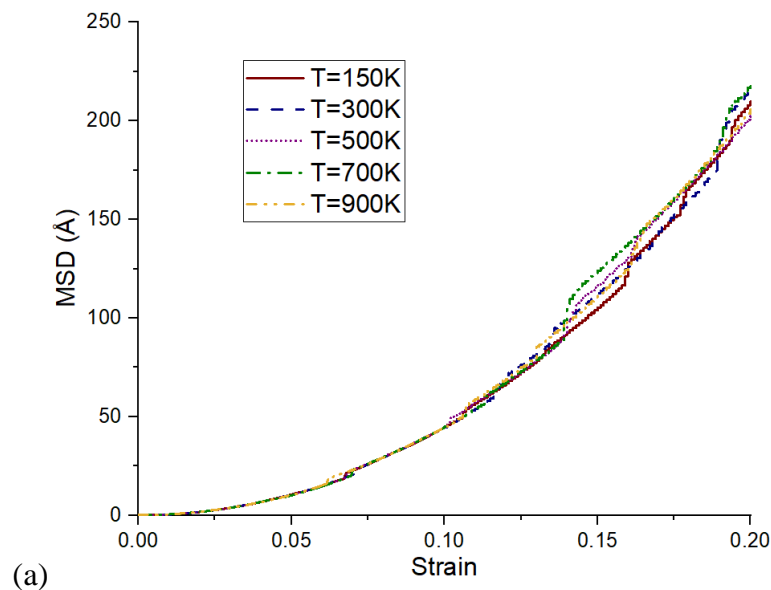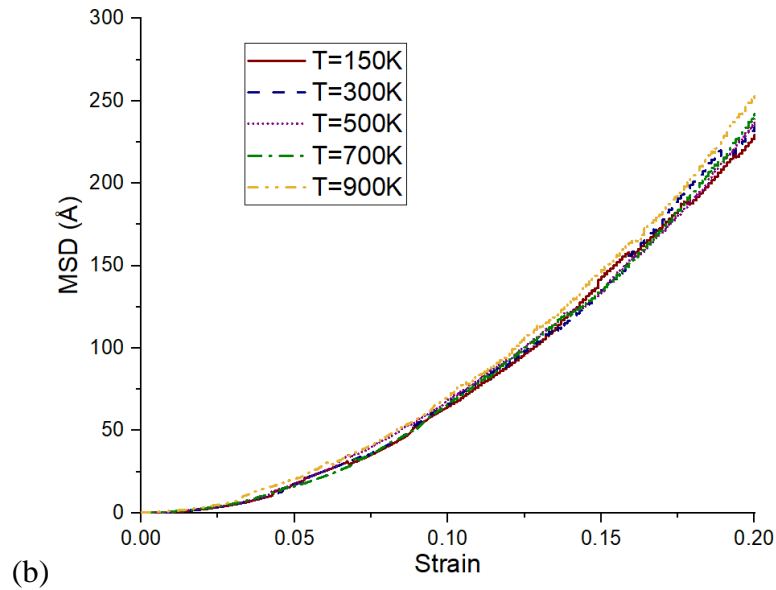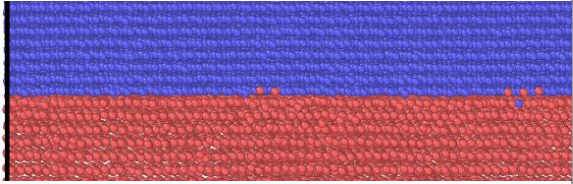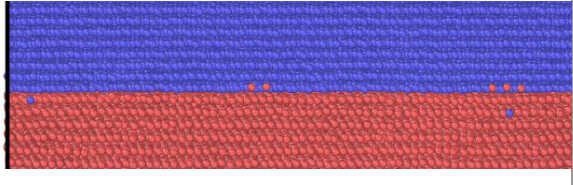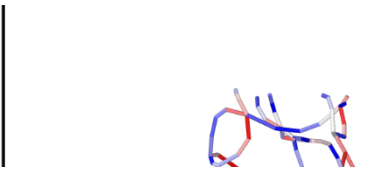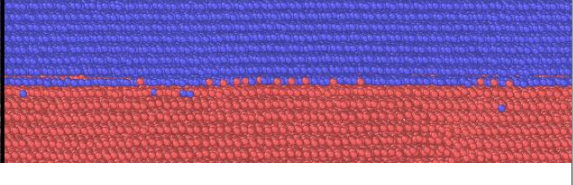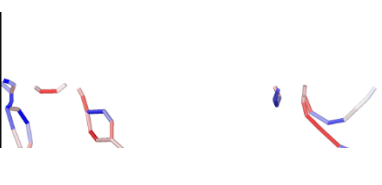
Figure 41 The mean squared displacement of (a) Fe in Al and (b) Al in Fe versus strain at all temperatures from 150K to 900K

Each of the minor jumps is associated with stress drop in the stress-strain plot. This is also referred to as a relaxation in one of the materials. As such, the displacement of the different atoms only occurs after system relaxation and as a result of the nucleated dislocations. The time corresponding to the start of the displacement of atoms, therefore the mixing, occurs at considerably low strains. As temperature increases, strains are also found to decrease. This is associated with increase in the thermal fluctuations at higher temperatures. The energy barrier needed to initiate interfacial mixing between the two materials is partially overcome by the mechanical load applied to the system with balance provided by the generated heat.

The MSD figures suggest that as temperatures increase, the slope of the MSD curve, which corresponds to the displacement velocity of the atoms, also increases. This is in accordance with the well-established temperature effect on displacement and diffusion coefficients. Due to the presence of misfit dislocations at the interface, creating defects in the structure, and making room for atoms to move, the displacement

initiated at the early stages is detected in the system microstructure in Figures 42 (a and

g). As strain increases, an interphase region appears quickly as atoms of Fe circulate in

the Al region (and vice versa) with more noticeable visual mixing (Figs 42 (a-f)).

concurrently, the movement of aluminum (red) and iron (blue) atoms is accompanied by

the increase of dislocation density in both materials across the interface (Figs 42 (g-l)).

Strain Level	Interfacial mixing	Dislocation patterns
0%	(a)	(g)
6.38%	(b)	(h)
11.3%	(c)	(i)

15.0%	(d) / (j)
18.8%	(e) / (k)
22.5%	(f) / (l)
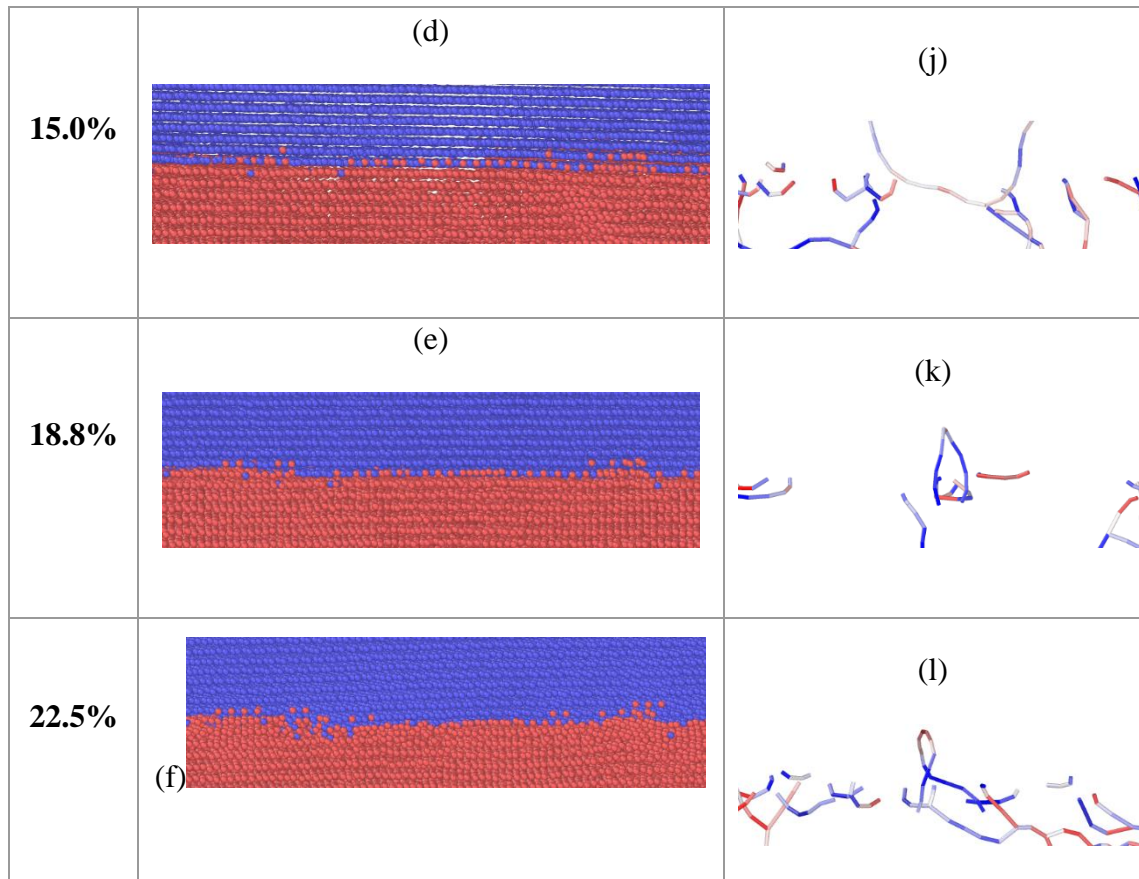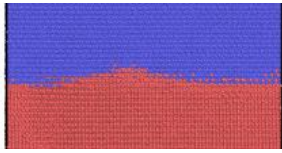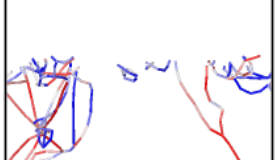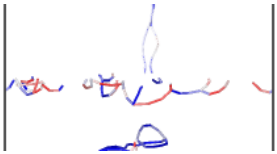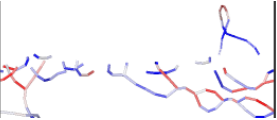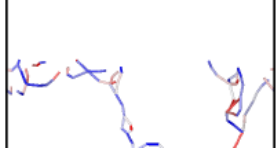
Figure 42 Interfacial mixing (a-f) at T=500K and different strain values and corresponding dislocations (g-l): Red dislocations are screw, blue are edge, and grey are mixed. Dominance of the edge dislocations is noticeable in the aluminum FCC crystal whereas a much lower density of mostly extended screw dislocations is visible in the BCC Fe crystal

These findings imply that the dislocations nucleation induces or facilitates the migration of the atoms at the interface. As per their definition, dislocations are line defects in a crystal, and any type of defect is considered as the original source behind any eventual mixing., The dislocations created in the Al FCC region pile up on the interface and aid the nucleation of dislocations in the Fe BCC from the interface on the other side. The dislocations in Fe, although much less dense as compared to those in Al, first appear at the interface and grow into the extended screw dislocations (Figure 39b).

Figure 43 shows interfacial mixing and dislocation patterns over five temperatures ranging from 150K to 900K. The effect of temperature on the number of

migrating atoms from both layers at the interface can be seen in the left column and are indicative of atomic intermixing. Visually, the mixing between the Al and Fe layers does not seem to be largely affected by initial temperature. This observation will be further corroborated below by the RDF results. The initial temperature can, however, affect the thermal expansion in the bulk of the material.

Temperature (K)	Interfacial mixing	Dislocation Patterns
150		
300		
500		
700		

900		
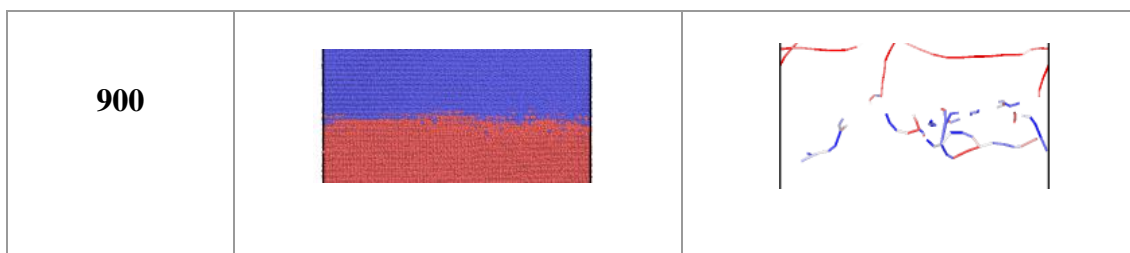
Figure 43 Effect of temperature on the mixing at the interface at the last simulation step corresponding to 22.5% strain.

E. RADIAL DISTRIBUTION FUNCTION AND INTERMETALLIC COMPOUND FORMATION

During loading, the RDF is computed at different positions in the system. RDF defines the positions of different neighboring atoms to each of the system atoms. The distance of these neighbors is stored in the RDF thus resulting in a global picture of the structure of either material at a given time in the simulation. The system is divided into N bins over which the distribution of the atoms is considered. This distribution is then averaged over time (or number of steps). After loading of the system, the RDF is assessed for the interface at different temperatures in Figure 44. All these temperatures are below the melting temperature of aluminum so that materials remain solid. The RDF was plotted in Figures 45a and 45b at different regions in the system, namely in the bulk of the Al and the Fe regions and at the interface between the two materials.
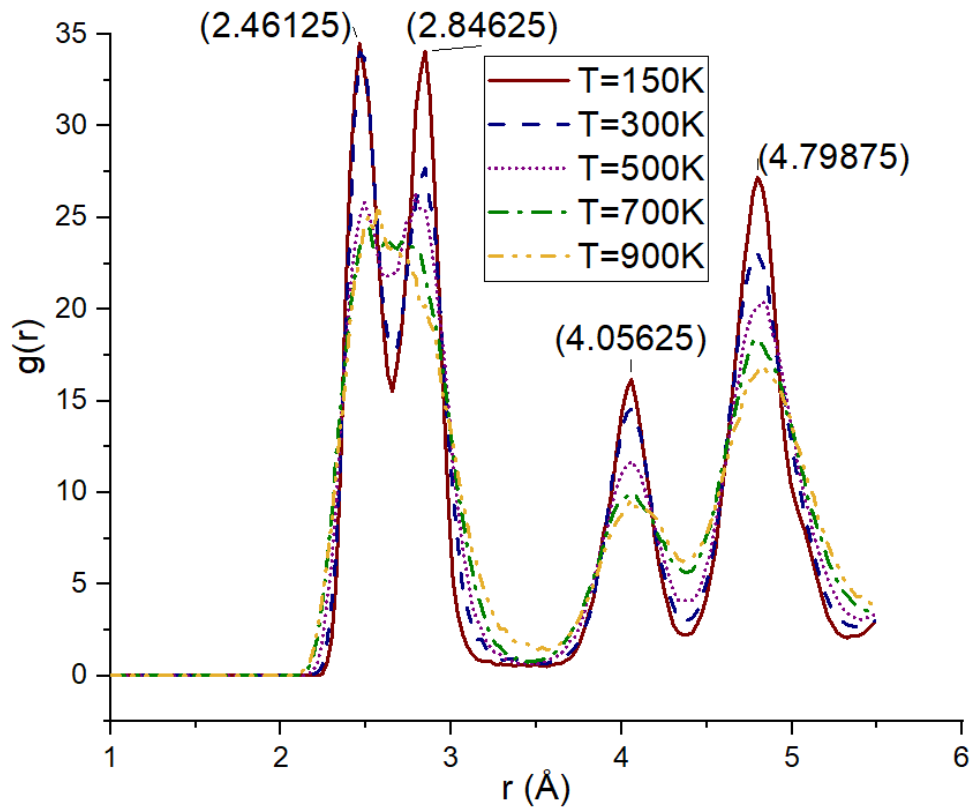
Figure 44 The evolution of the RDF of the interface structure at different temperatures. The first two peaks of the RDF merge into one larger peak due to temperature increasing (T=700K and T=900K). Positions of the first four nearest neighbors are preserved.

Peak positions are investigated at the last step following load application and compared to the initial RDF for T=300K. Figures 45 (a-c) show positions as compared to the original structures of Al and Fe separately. The atomic arrangement at the interface, such as the one shown in Figures 43 (a-f), indicates a transition from a sharp interface into a diffused interphase region with noticeable mixing. The RDF in Figure 44 corroborates these results at different temperatures. This evidence suggests that solid-state mixing is achieved at relatively low temperatures provided the high compression loading. Similar to the findings in Section "C" regarding the effect of temperature on mixing between Al and Fe, RDF showed a structure that is relatively independent of system temperature where the four identified peaks are in accordance with the FeAl intermetallic CsCl crystal structure (Table 15 and Figure 44).

Table 15 The evolution of the first four peaks' positions with respect to temperature. The positions are rather unchanged except for the fourth peak which tends to shift to the right as temperature increases due to the thermal expansion.

	Peak Positions (Å)			
	Peak 1	Peak 2	Peak 3	Peak 4
T=150K	2.482	2.827	4.047	4.801
T=300K	2.478	2.825	4.050	4.811
T=500K	2.464	2.803	4.047	4.830
T=700K	2.445	2.768	4.037	4.833
T=900K	2.467	2.807	4.043	4.849

The RDF is expected to display peaks at positions where a high concentration of atoms is found. These peaks correspond to the 1st, 2nd, and 3rd (…) nearest neighbors (NN) in each crystalline structure. For example, when an atom belongs to an FCC crystalline structure the 1st NN to this atom are expected to appear at a distance of $P_1 = \frac{\sqrt{2}}{2} a_0$, where a_0 is the lattice parameter of the crystalline structure. The 2nd NN would then appear at $P_2 = a_0$ and the 3rd NN at $P_3 = \frac{\sqrt{3}}{2} a_0$. This explains the peaks that appear in the RDF of the Al region which translate an FCC crystalline structure with $a_0 = 4.05$Å (P_1=2.864Å, P_2=4.05Å and P_3=4.96Å). This structure remains unchanged even following the large deformation reached at the end of the simulation. Similarly, in the case of Fe BCC structure, the first three peaks are reported at $P_1 = \frac{\sqrt{3}}{2} a_0 = 2.482$Å, $P_2 = a_0 = 2.867$Å, and $P_3 = \sqrt{2} a_0 = 4.05$Å. The RDF plots suggest that the crystalline structure of Al and Fe is preserved throughout the loading process and that the peak positions correspond to the theoretical calculations (Figure 45a and 45b). The RDF was also plotted (Figure 45c) for the region defined in the script as the 'close interface'. It

represents the neighboring atoms most likely to interact and mix under the given conditions. The RDF found for this region shows four peaks that overlap at some levels. A post-analysis deconvolution demarcates the precise positions of the first four peaks of this RDF as the colored peaks located at r_1, r_2, r_3 and r_4 (values listed in Table 16).

(a)

(b)

(c)
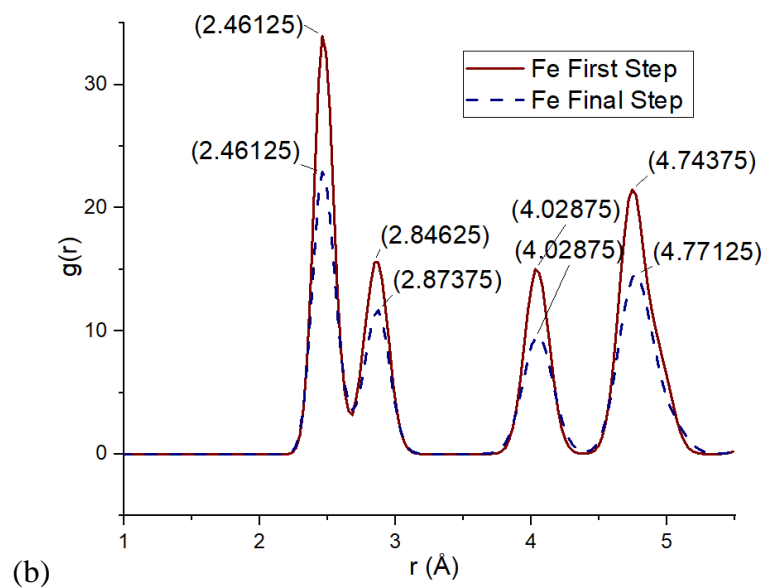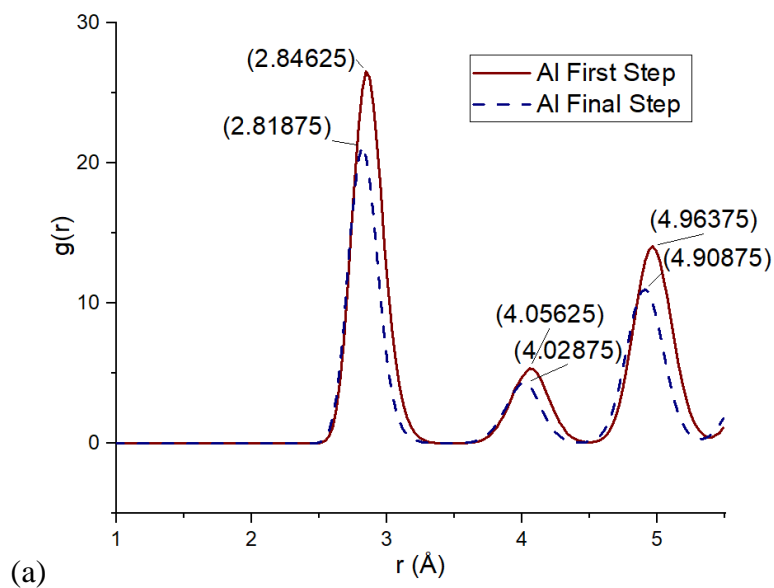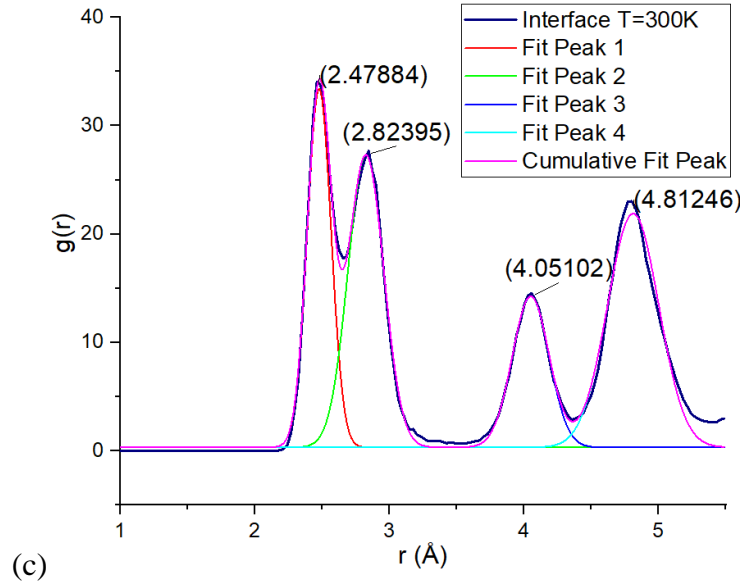
Figure 45 RDF at first and last steps for (a) Al, (b) Fe, and (c) Al/Fe interface (all at T=300K) indicating the preservation of the Al and Fe crystal structure during the entire loading process and showing the structure of the interface reflected by the first four peaks corresponding to the first four nearest neighbors.

Zhang et al. [130] found that the FeAl intermetallic compound has a CsCl structure with a lattice parameter of a_0=2.893Å. Such a structure resembles Fe's BCC structure but contains an aluminum atom in the center of its unit cell instead of an iron atom. The aluminum atom which has larger radius than the iron atom slightly distorts the cell and expands it when compared to the Fe BCC perfect crystal (a_0=2.867Å). Based on the crystal structure of this intermetallic compound, the theoretical positions of the first four peaks of this structure would be located at; P_1=2.505Å, P_2=2.893Å, P_3=4.09Å, P_4=4.797Å. Table 16 lists the positions of the peaks identified from lattice parameter values published by Zhang, et al. [130]. Following slow relaxation of the system and cooling to room temperature, these values compare favorably suggesting that the generated structure at the interface is likely FeAl intermetallic compound.

119

Table 16 Expected peak positions according to Zhang, et al. [130] versus found peaks position (this work). The most likely intermetallic to form is predicted by the positions of the neighboring atoms found following mixing.

Peak Number	Expected position (Å) according to Zhang, et al. [46]	Peak positions (Å) (this work)	Difference %
r_1	2.505	2.478	1.08
r_2	2.893	2.825	2.35
r_3	4.09	4.050	0.98
r_4	4.797	4.811	0.29

These results support the theory which limits the effect of temperature on the structure of the formed intermetallic compound in the case of (1) quench cooling from high temperatures (past melting) and (2) an unstressed (or uncompressed) systems. However, in these simulations, the structure of the intermetallic compound is dominated by the effect of the compressive stress rather than the temperature.

F. DISCUSSION

The same MD simulations were also conducted on other interfaces and yielded similar results in terms of the crystal structure of the intermetallic compound formed. In this second orientation the different atoms were stacked in the z-direction [001] thus creating an interface of this same direction with respect to both materials. The difference in the crystal structures (FCC vs BCC) results in an incoherent Al/Fe interface and the large difference between the Fe and Al lattice parameters (a_0=2.867A [23] and a_0=4.05A [24] respectively) gives rise to artificial internal stresses when periodic boundary conditions are used [22]. In order to minimize the misfit between the

two materials, the aluminium crystal was rotated by 45^0 about the z-axis. The spacing

therefore between the Al atoms was reduced to $\frac{\sqrt{2}}{2} a_0 = 2.864$Å and the lattice

mismatch between Al and Fe was reduced to 0.11%. Due to the minimal mismatch in

the spacing between the interface layers misfit dislocations are not automatically created

and strains need to be added to the different layers in order to create them [25]. After

having taken into account the orientation of the crystals such that the internal stresses

due to the mismatch of the lattices are minimized, the position of the Fe atoms with

respect to the Al atoms was then investigated. This was done using the generalized

stacking fault interface energy as a function of the offset of Fe with respect to Al in the

x and y directions designated by dx and dy respectively [26].

This study was performed as an independent step in one of the simulations prior

to minimization and its results were adopted for the rest of the simulations. The surface

plot presented in Figure 46a indicates that the lowest energy of the interface is obtained

for $dx = dy = 0$ which in other term means that the origin of the Fe lattice should not

be offset and thus the Fe atom would be placed midway between the two neighbouring

Al atoms of the adjacent layer as shown in Figure 46b.
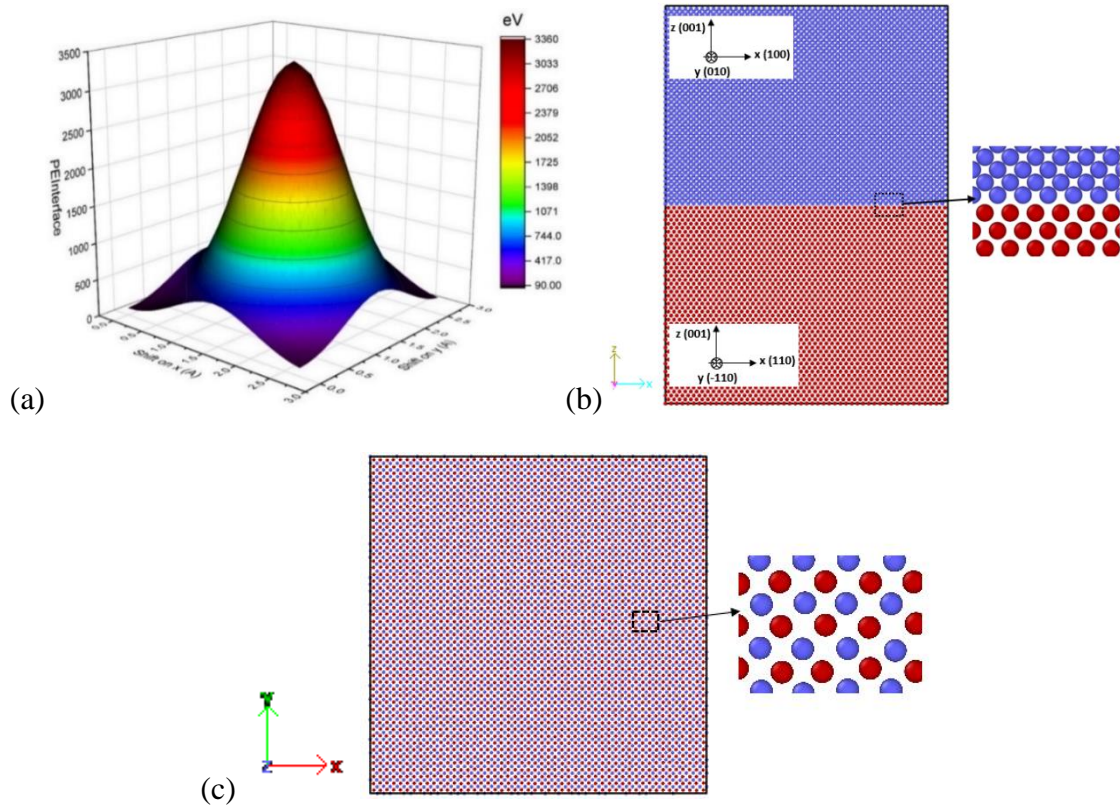
Figure 46 Al (FCC) / Fe (BCC) [001] interface: (a) generalized stacking fault interface energy surface plot showing the most stable position of Fe atoms with respect to Al in terms of dx and dy. The corresponding configuration of Al/Fe system in (b) side view xz plane and (c) top view xy plane.

Unlike in the case of the original KS orientation, the case of the new theoretical interface orientation, and as expected given the minimization of the lattice mismatch, misfit dislocations were not generated in either material and for any of the temperatures tested. The mechanical response of the system also reveals a stress-strain behavior with two relaxation stresses the first one corresponding to the nucleation of dislocations from the bulk in the Al region and the second corresponds to the nucleation of dislocations which took place from the interface in the Fe region.

Also similar to the previously reported simulation results, dislocations on both sides of the solid Al/Fe system are observed to multiply and grow shortly at the same strain levels corresponding to concurrent relaxations in the stress-strain plots. The RDF

122

analysis again indicates that the most favorable positions the mixed Al and Fe atoms

would assume are that of the FeAl intermetallic compound (CsCl crystal structure).

CHAPTER VI

YIELD AND FLOW STRESS MODELS FOR AL/FE INTERFACE SUBJECTED TO EXTREME LOADING AND THERMAL CONDITIONS

In further analysis, MD was again employed to simulate the mechanical response of Al/Fe interface under compression at extreme conditions of seven temperatures and four strain rates ranging between 150K and 900K and $5.0 \times 10^7 \text{s}^{-1}$ and $1.0 \times 10^{10} \text{s}^{-1}$, respectively. Yield and flow stress models are proposed for this range of temperature and strain rate based on the MD generated data. Stress-strain histories show two distinct yield stress points for simulations at temperatures below 500K, which tend to merge into one as the temperature increases. Microstructural analysis show that nucleation of dislocations, which occur in the bulk of the aluminum region, is associated with the first yield point. In the iron region, dislocations nucleate at the Al/Fe interface and are associated with the second yield point. The incoherent interface employed in these simulations contributes to the heterogeneous nucleation in iron by creating a defected area favorable for this nucleation from the aluminum side. The competing mechanisms between dislocation motion and phonon drag driven deformation are also simulated and modeled.

A. SIMULATION SETUP AND POTENTIAL

Similar to the simulations reported in Chapter 3, LAMMPS was employed to investigate the mechanical response of the Al/Fe interface system under extreme conditions of compressive loading with focus on the effect of strain rate and temperature on the mechanical behavior of this mixed system. The interface orientation was chosen such that the difference between the atom spacing in the Al and Fe regions

is minimized. This interface places the z-axis in the [001] direction for both crystals. As elaborated in Chapter 3F, the rotation of the Al crystal by 45° about the z-axis [131] reduces the spacing between the Al atoms to become $\frac{\sqrt{2}}{2}a_0 = 2.864$Å thus resulting in negligible lattice mismatch between Al and Fe of 0.11%. The position of the iron atoms with respect to the aluminum atoms was chosen based on the surface energy calculations as reported previously (Figure 46).

The EAM potential developed by Mendelev et al.[110] was adopted once more during these simulations to describe the Al-Al, Fe-Fe, and Fe-Al interactions. The detailed equations of this potential are all reported in Chapter 3A.2.

B. EFFECT OF TEMPERATURE AND STRAIN RATE ON MECHANICAL RESPONSE OF AL/FE INTERFACE

Figure 47 shows the stress strain behavior of the simulated Al/Fe interface at temperatures of (a) 150K, (b) 300K, (c) 600K, and (d) 800K all at the strain rates 5.0×10^7, 5.0×10^8, 1.0×10^9, and 1.0×10^{10}s^{-1}. Initially, the response is linear elastic with a slope corresponding to the Al/Fe system' "effective" elastic modulus. Fig 47a shows that for deformation temperatures well below the critical temperature (Tc=340K for iron), two distinct yield points are formed. The lower yield point corresponds to the nucleation and generation of dislocations in the Al region leading to stress relaxation as manifested in the change of the slope or the drop in stress. Following that, a strong hardening effect is displayed leading to a large increase in the stress until the nucleation in the Fe region ensues. We can also see that as the strain rate increases, slight increase in the nucleation stress in Al is detected especially for T=150K (Fig 47a) and T=300K (Fig 47b). As the temperature increases, the sensitivity of the first yield stress to strain

rate decreases. However, it appears that at this very low temperature, yielding in Fe is
somewhat strain rate insensitive.
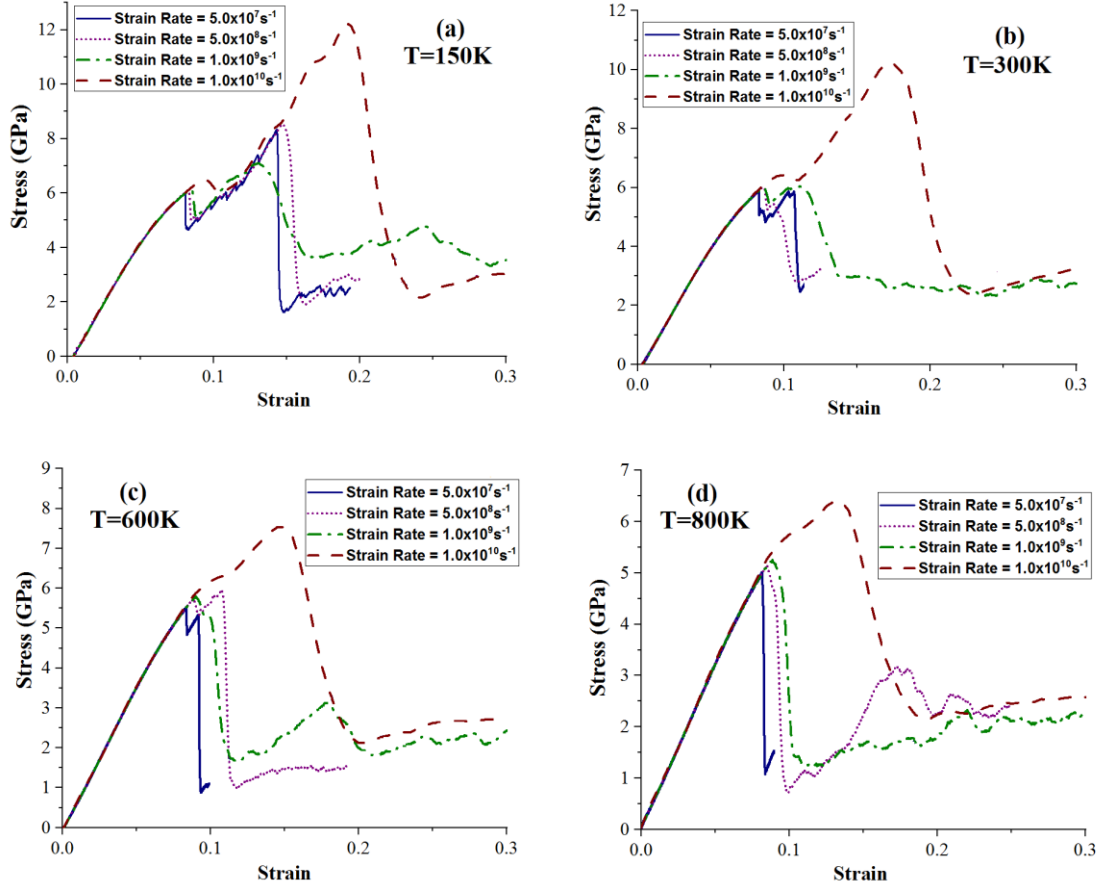
Figure 47 Al/Fe system stress versus strain curves for (a) T=150K, (b) T=300K, (c)
T=600K and (d) T=800K and $\dot{\varepsilon}$= $5.0\times10^7s^{-1}$, $5.0\times10^8s^{-1}$, $1.0\times10^9s^{-1}$, and $1.0\times10^{10}s^{-1}$

The strong hardening behavior in the system is attributed to the dislocation

accumulation at the interface in addition to the ability of the interface to partially absorb

the blocked dislocations[62] leading to their annihilation. This strong hardening

behavior disappears at higher temperatures (greater than 400K). This is depicted in

Figure 47c and 47d where only a single yield point marks the plastic relaxation process

indicating that above the critical temperature of iron, the nucleation stresses in both

metals are very close. To connect the different aspects of the deformation process and

mechanical behavior with the underlying physical phenomenon causing them, detailed

microstructural analysis showing different features of the dislocations' nucleation and interactions are discussed below as obtained from the post-processing tool OVITO [131].

Following the effect of strain rate on the nucleation stress in Al and Fe, the deformation temperature affects the two materials in a very different way. In Figure 47, the nucleation stress in Al decreases from about 6GPa at 150 K to around 5GPa at 800 K indicating a modest temperature sensitivity in Al. This can be explained by the balancing effects of the temperature softening on the barrier energy for bulk nucleation in Al and the opposing temperature hardening effect of phonon drag. Competition between these two factors results in relatively small drop in Al nucleation stress.

For iron, nucleation stress at $5.0\times10^7 s^{-1}$ is found to decrease sharply from 8GPa at 150 K to 6GPa at 300 K. Stress then drops smoothly to 5.5GPa and 5GPa at 600K and 800K respectively. This behavior is attributed to the much more pronounced temperature softening effect on lattice friction commonly reported for BCC, especially at temperature below the critical temperature when compared to a modest temperature hardening effect of phonon drag [46,55,132].

Since the simulations are carried out on pristine Al/Fe interface at extremely high strain rate, elastic overshoot in the stress is unavoidable. Such behavior has been reported for pure metals simulated at wide range of temperatures and strain rates [71]. In pure metals, the elastic overshoot is followed by abrupt drop in stress due to plastic relaxation associated with homogeneous, and a single yield points marks this event. In the case of the simulated Al/Fe interface, the combined effects of temperature, stress, and the presence of the interface itself, add up to a complex picture that requires detailed analyses of the microstructure evolution. Plastic relaxation in such incoherent

interface with no preexisting dislocations may take place by the nucleation of dislocations homogeneously from the bulk, or heterogeneously from the interface. In BCC metals, the core of screw dislocation is compact unlike that of the edge and mixed dislocations. As a result, the lattice friction of screw segments is much larger than that of other dislocations. This behavior changes when the deformation temperature approaches the critical temperature of the material (340 K for iron), where lattice friction for all types of dislocations becomes almost the same, and thus the mobility becomes isotropic [46,132].

Effective modulus values are calculated at all simulated temperatures and stain rates and plotted in Figure 48. The effective elastic modulus decreases with temperature in a linear fashion. This may be attributed to the drop in the atomic bonding strength with temperature allowing easier lattice deformation [133]. The elastic modulus appears to be insensitive to strain rate at all simulated temperatures.
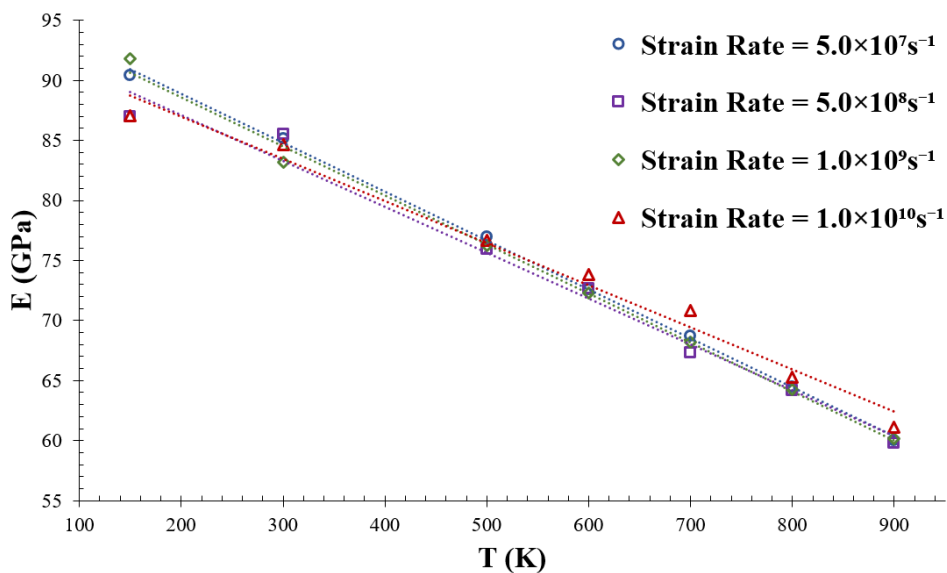
Figure 48 Variation in the effective modulus with temperature at different strain rates

C. Microstructural analysis of dislocations nucleation and evolution in Al/Fe bimetallic system

During the mechanical analysis of the Al/Fe system it was found that, depending on the combination of the strain rate and temperature, two distinct yield points with different magnitudes or a single yield point is formed in the stress strain plots. In order to explain some of the behaviors observed in these plots of Figure 47, the effects of temperature and strain rate on dislocation microstructure evolution in the Al/Fe bimetallic system is investigated.

The large stress required to relax the Fe crystal at temperature below the critical temperature is predominately due to the very low mobility of the screw dislocations at low temperatures. In order for yielding to occur, the applied stress should surpass the nucleation stress. The latter is composed of a thermal part and a constant athermal part (σ_a) as

$$\sigma_{nuc} = \sigma_a + \frac{k_B T}{V^*} \ln \frac{\dot{\varepsilon}}{\dot{\varepsilon}_0(T,V^*)} \qquad (3)$$

where T refers to the temperature (K), k_B is Boltzmann's constant, V^* the activation volume and $\dot{\varepsilon}$ and $\dot{\varepsilon}_0$ the strain rate and reference strain rate respectively. As temperature increases at constant strain rate, the ratio between $\dot{\varepsilon}$ and $\dot{\varepsilon}_0$ decreases and thus the logarithm eventually becomes negative leading, therefore, to a drop in the yield stress with temperature. It is to be noted here, that in this system, dislocations are nucleated in Fe from the interface in Fe, which is expected to be smaller than its homogenous nucleation stress which highlights the effect of interface on the overall yielding behavior. The analysis of the microstructure presented in Figures 49, 50 and 51 illustrates that after relaxation occurs in Al, it becomes rather easier for Fe to follow due

to the creation of favorable nucleation sites located at the interface after dislocations

have accumulated/absorbed from the Al side [131].
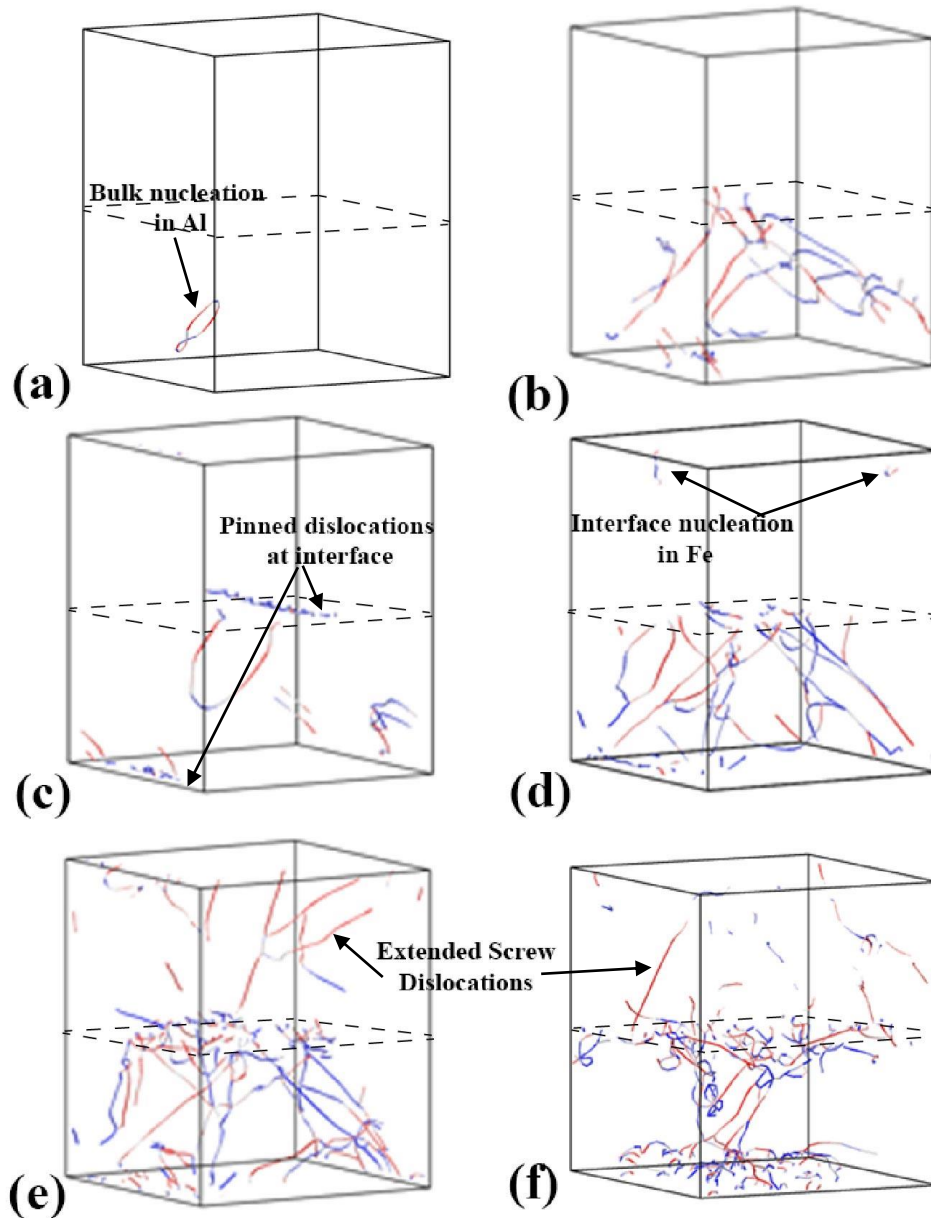
Figure 49 Dislocation microstructure evolution for a strain rate of 5.0×107 and T=150K (a) 8.11% nucleation of the first stable dislocation loop in Al from the bulk (b) 8.13% dislocation multiplication and growth. Screw (red), edge (blue) and mixed (grey) dislocations presence with no preference between the types (c) 8.14% dislocations in Al migrate and get pinned and partially absorbed at the interface (d) 9.90% nucleation of the first stable dislocations in Fe from the incoherent interface (e) 9.98% dislocation growth in both Al and Fe regions with dominant presence of extended screw dislocations in Fe (f) 15% growth and multiplication of dislocations in both regions (Al bottom half; Fe top half)
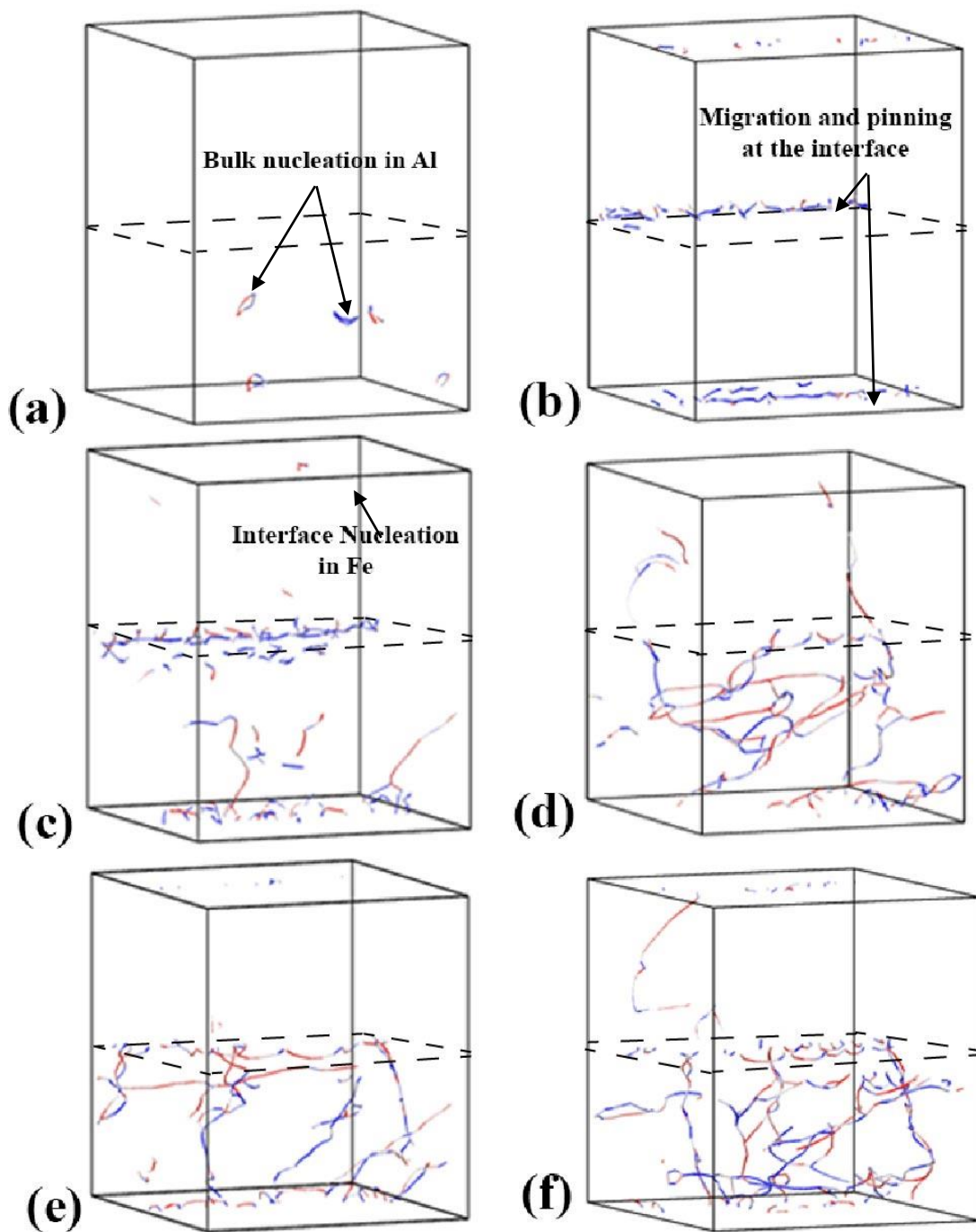
Figure 50 Dislocation microstructure evolution for a strain rate of 5.0×107 and T=500K (a) 8.38% bulk nucleation in Al (b) 8.56% migration and pinning at the interface after getting partially absorbed (c) 10.2% heterogeneous nucleation at the interface in Fe (d) 13.4% multiplication and growth of dislocations (e) 15.6% absorption of dislocations created in the Fe region (f) 18.1% new nucleation and growth in both regions (Al bottom half; Fe top half)

131
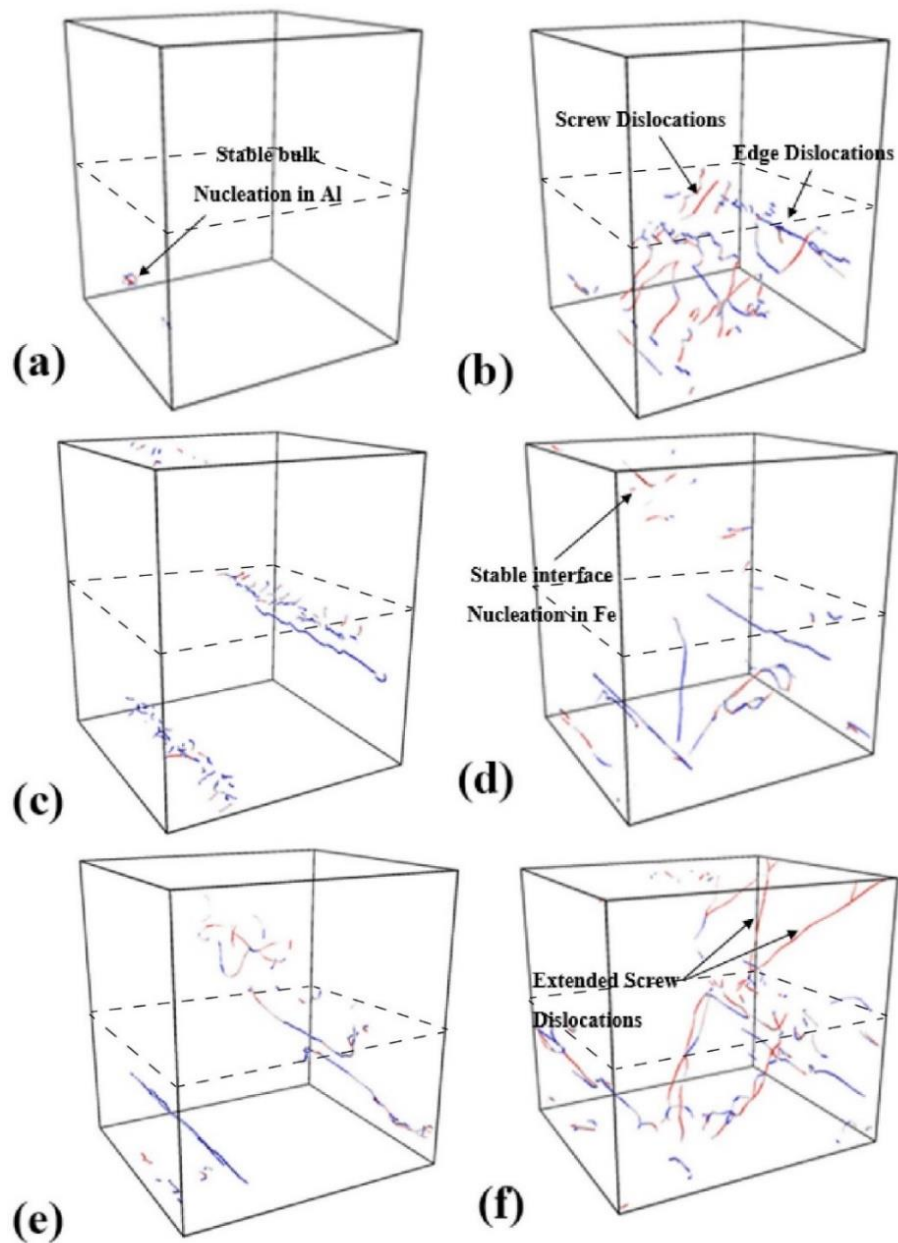
Figure 51 Dislocation microstructure evolution for a strain rate of 5.0×108 and T=500K
(a) 8.35% nucleation of the first stable dislocation loop in Al from the bulk (b) 8.63%
dislocation multiplication and repartition in screw (red), edge (blue) and mixed (grey)
dislocations with no preference between the types (c) 9.88% dislocations in Al migrate
and get pinned and partially absorbed at the interface (d) 11% nucleation of the first
dislocations in Fe from the incoherent interface (e) 13.5% dislocation growth in both Al
and Fe regions (f) 18.8% growth and multiplication of dislocations in both regions with
a clear dominance of extended screw dislocation in the Fe region (Al bottom half; Fe
top half)

Considered are representative cases of strain rates of $5.0 \times 10^7 \text{s}^{-1}$ and $5.0 \times 10^8 \text{s}^{-1}$

and temperatures of 150K and 500K. Figure 49 shows snapshots of the microstructure

formed in a sample subjected to $5.0 \times 10^7 s^{-1}$ at 150K. Dislocation nucleation is initiated in the Al region. Small loops of Shockley partials are nucleated in the Al bulk which soon multiply and migrate immediately after that to the interface (Figs. 49a and 49b). The dislocations appear to be partially absorbed by the incoherent interface leaving behind debris of small dislocation segments and half loops as illustrated in Fig 49c. This leads to the hardening behavior seen in Figure 47a. Once the applied stress becomes high enough, dislocations nucleate in the Fe region from the interface which constitutes a favorable site to this nucleation as seen in Fig 49d.

The hardening behavior observed in the stress strain plots of Figure 47 can also be correlated to the different types of sessile dislocations that are formed in the Al region as depicted in Figs. 52a-d. For the Al/Fe interface system, the figures plot hardening mechanisms and dislocation types such as Stair Rod, Hirth and Frank locks, which limit the movement of the Shockley partials, thus, contributing to stress hardening. Once nucleation stress in Fe is attained, the first dislocation appears in the Fe region from the interface and extended sessile screw dislocations are formed, due to the movement of the highly mobile edge segments (Figs. 49e and 49f). The edge segments get absorbed at the interface and the screw lines remain sessile or slightly moving until the stress becomes sufficiently high to allow them to move.

When deformation temperature increases to 500K, which is above the critical temperature of iron, microstructure evolution in the Al region becomes similar to that observed at 150K. Once the applied stress exceeds the self-stress of the first dislocation loop, the dislocation bows out and expands (Figs. 50a, 50b). In the Fe region extended screw dislocations are no longer present indicating isotropic mobility of edge and screw segments.
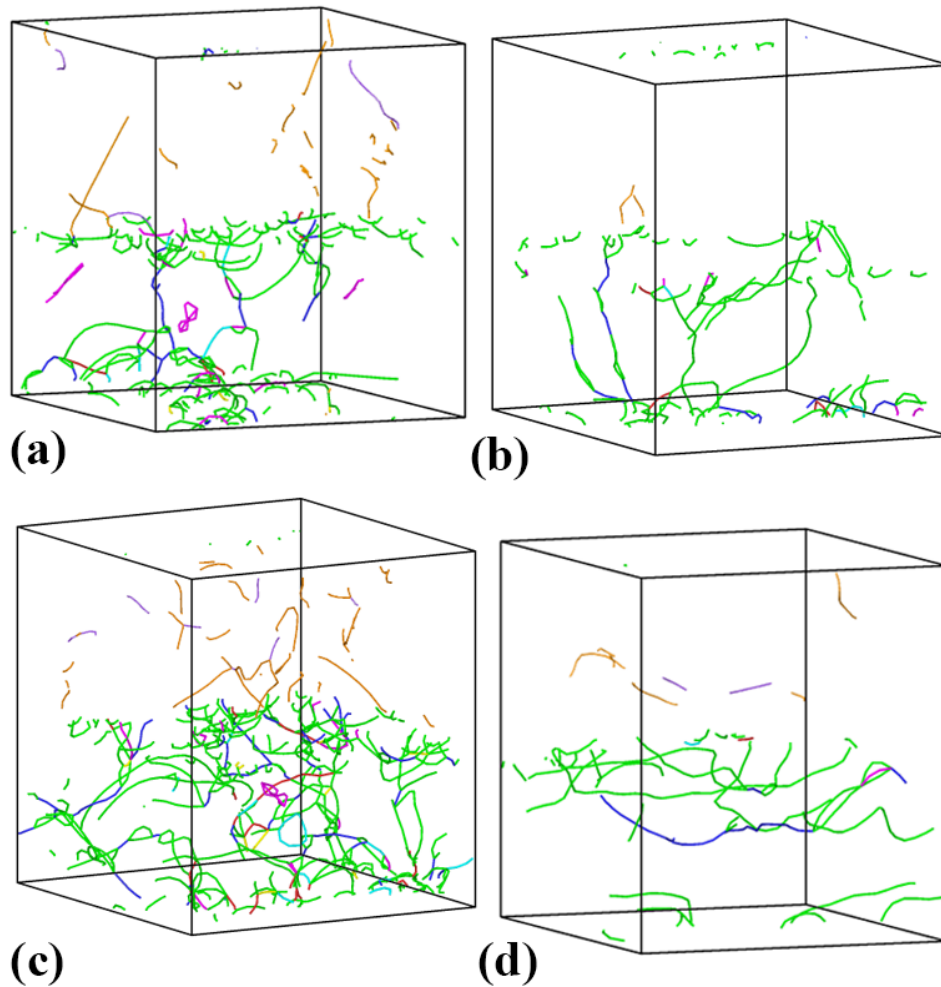
Figure 52 Hardening mechanisms and dislocation types in Al/Fe interface system at (a) $\dot{\varepsilon} = 5.0 \times 10^7 s^{-1}$ and T=150K (b) $\dot{\varepsilon} = 5.0 \times 10^7 s^{-1}$ and T=500K (c) $\dot{\varepsilon} = 5.0 \times 10^8 s^{-1}$ and T=150K and (d) $\dot{\varepsilon} = 5.0 \times 10^8 s^{-1}$ and T=500K and 17% strain. Al region: Perfect dislocations (navy), Shockley partials (green), Stair Rod (pink), Hirth (yellow), Frank (cyan) and Fe region: ½<111> mobile dislocations (orange) and <100> sessile dislocations (purple)

The same process of stable bulk nucleation in Al followed by multiplication and migration of the dislocations to the interface is again observed at a higher strain rate of $5.0 \times 10^8 s^{-1}$ and T=500K (Figs. 51a, 51b and 51c). These dislocations are again partially absorbed by the incoherent interface and thus form a favorable nucleation site to the dislocations in Fe (Fig 51d). The unique effect of the increase in strain rate is observed on the presence of extended screw dislocations in the Fe region even above critical temperature. This is also in accordance with Figure 52 where the quantity of

<100> sessile dislocations in BCC iron increase with increasing strain rate at fixed temperature (Figs. 52a and 52c for T=150K and Figs. 52b and 52d for T=500K). This is not the case for aluminum where the different junctions and jogs are not found to change much with strain rate at fixed temperature.

In addition to the microstructure evolution observed in Figures 49, 50 and 51, another important mechanism is highlighted in Figure 53 where two dislocations in the Fe region with the same burger's vector and opposite line senses annihilate following a double cross slip commonly reported in BCC deformation mechanisms.
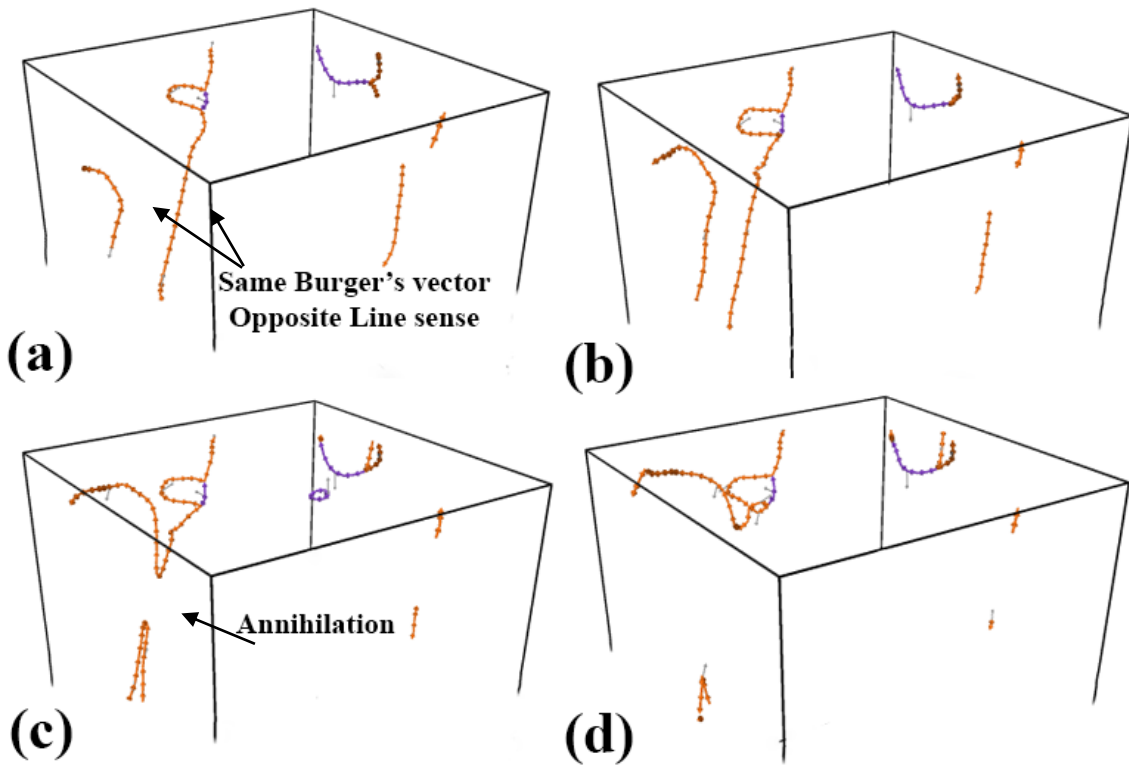
Figure 53 Annihilation mechanism by double cross slip in BCC Fe region at $\dot{\varepsilon} = 5.0 \times 10^8 s^{-1}$ and T = 300K and strain of (a) 12.4%, (b) 12.7 %, (c) 12.8%, and (d) 12.9%

Complementing the microstructure histories evolution and the mechanical response of the Al/Fe interface system, the effect of temperature and strain rate was also considered on the dislocation density evolution in Figure 54 at a constant strain rate and

135

Figure 55 at constant temperature, respectively. Dislocation density, calculated as the ratio between the total dislocation length in both Al and Fe over the system volume at a specific strain level, first takes a positive value for all simulations at strains below 10% when the first dislocations appear in the Al region. As the strain increases the dislocation density also increases before saturating at a plateau after the dislocations have filled both regions of the simulation box. This saturation density was found to be relatively insensitive to the change in temperature (T=150K, T=300K, T=500K, T=700K) at a fixed strain rate of $5.0 \times 10^7 s^{-1}$ (Figure 54). The temperature is however noticed to increase the strain at which the saturation density is attained. This is possibly due to the slight increase in the system volume at increased temperatures in addition to the increase in the drag force which tends to hinder the motion and multiplication of dislocations and thus additional time is needed for the deformation to reach its maximum. In Figure 55, the effect of strain rate ($\dot{\varepsilon} = 5.0 \times 10^7 - 1.0 \times 10^{10} s^{-1}$) was observed on the dislocation density evolution at a fixed temperature of T=300K. As the strain rate increase the maximum dislocation density also increased gradually. This is perhaps due to the increase in nucleation rate along with strain rate and the increase in the average velocity of the dislocations.
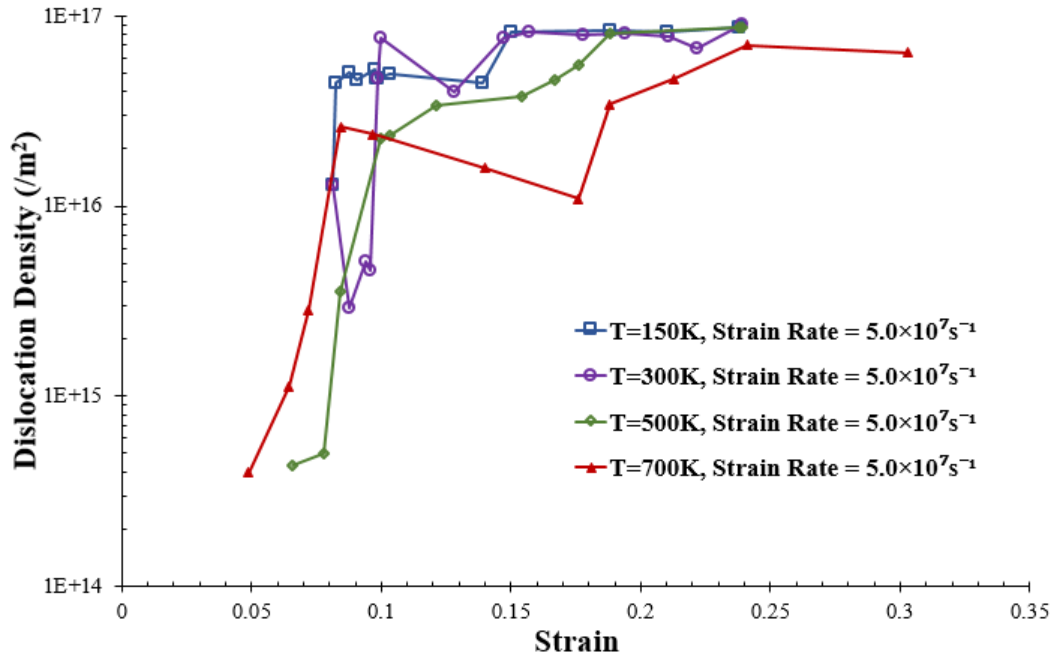
Figure 54 Dislocation density (/m2) evolution at different temperatures function of strain (all at strain rate $= = 5.0 \times 10^7 \ s^{-1}$)
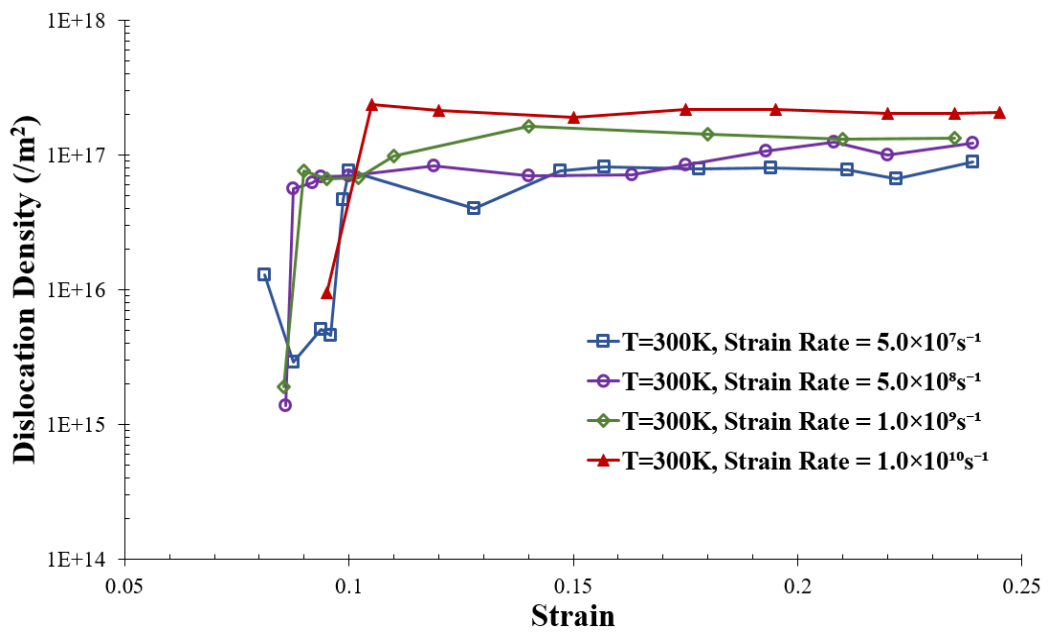
Figure 55 Dislocation density (/m2) evolution at different strain rates function of strain (all at temperature = 300K)

D. PHYSICAL MODELING OF YIELD AND FLOW STRESS

Hereunder, the first, the second and the flow stresses are physically modelled capturing the coupled effects of temperature and strain rate on all three stresses. Phonon

137

drag is the resistance to the motion of dislocations caused by phonon scattering and radiation and by phonon wind effect that are proportional to temperature [46,132]. Strain rate is directly proportional to the mobility of the dislocations through the Orowan equation;

$$\dot{\varepsilon}_{eff} = \frac{1}{\sqrt{3}} \rho_{mob} b v \tag{4}$$

where $\dot{\varepsilon}_{eff}$ is the effective plastic strain rate, $\frac{1}{\sqrt{3}}$ is the conversion factor between shear and plastic strain, ρ_{mob} is the mobile dislocation density, b is the burger vector. The average dislocation glide velocity, v, is described by

$$v = c_t \times \left(1 - \frac{T}{T_{cr}} \times \frac{d_0}{d}\right)^{1/2} \tag{5}$$

where v: glide velocity, c_t: transverse sound velocity, d: drag, d_0: constant, T: temperature, and T_{cr}: critical temperature. Mobility is inversely proportional to the drag (equation 5) which is directly proportional to temperature. The increase of temperature has a positive effect on phonon drag and thus a negative effect on mobility which leads to the thermal hardening mechanism. Drag coefficient also depends on the dislocation character such that for the case of iron and for temperatures below the critical temperature the drag coefficient for a screw dislocation is equal to 100 times the drag for an edge. However, for temperatures beyond T$_{cr}$ the drag coefficient is independent of the dislocation character.

The effect of temperature and strain rate on the first, second yield and flow stresses are shown in Figures 56 (a, b and c), respectively. The commonly reported decrease of lattice friction [55] with increasing temperature, especially below critical

temperature and for BCC metals is observed in the large decrease of the second yield points at the lowest temperature of T=150K (Fig 56b). This thermal softening effect is not limited to the lattice friction decrease but also contributes to the decrease of the ratio in the logarithm of equation 3 as stated previously. Thus the reduction of the first yield point and the flow stress with increasing temperature. All three tested stresses (yield 1, yield 2 and flow) are found to increase linearly with $ln\dot{\varepsilon}$. The two mechanisms, namely the thermal softening and the strain rate and temperature hardening due to the increase in phonon drag and hindering of the dislocation motion on the other, compete intensely in the loading of this interface. Physical modeling of this process is, therefore, desirable.
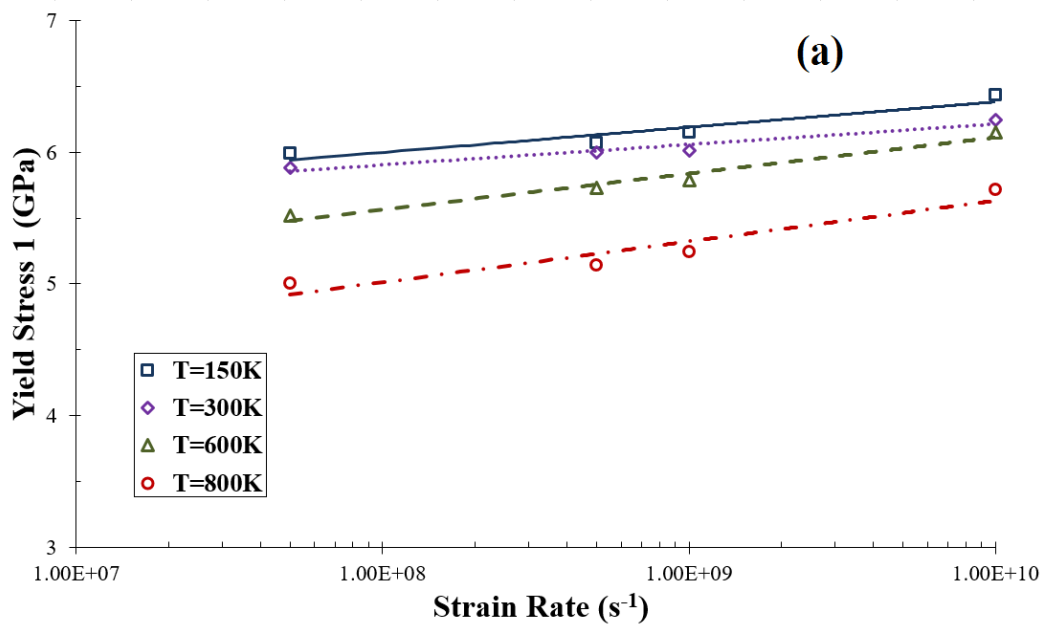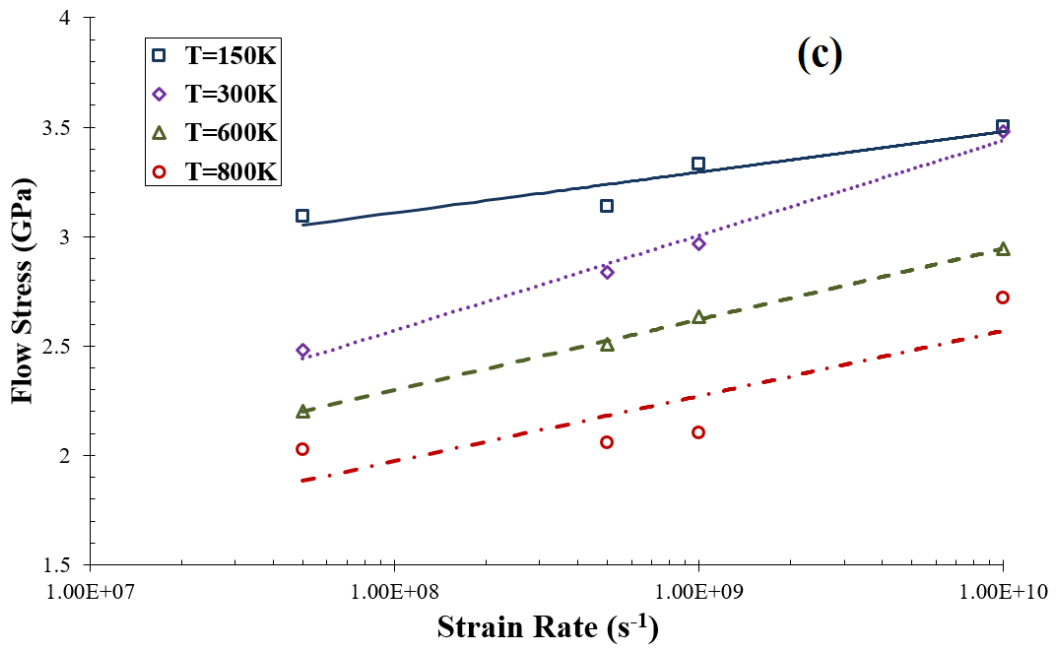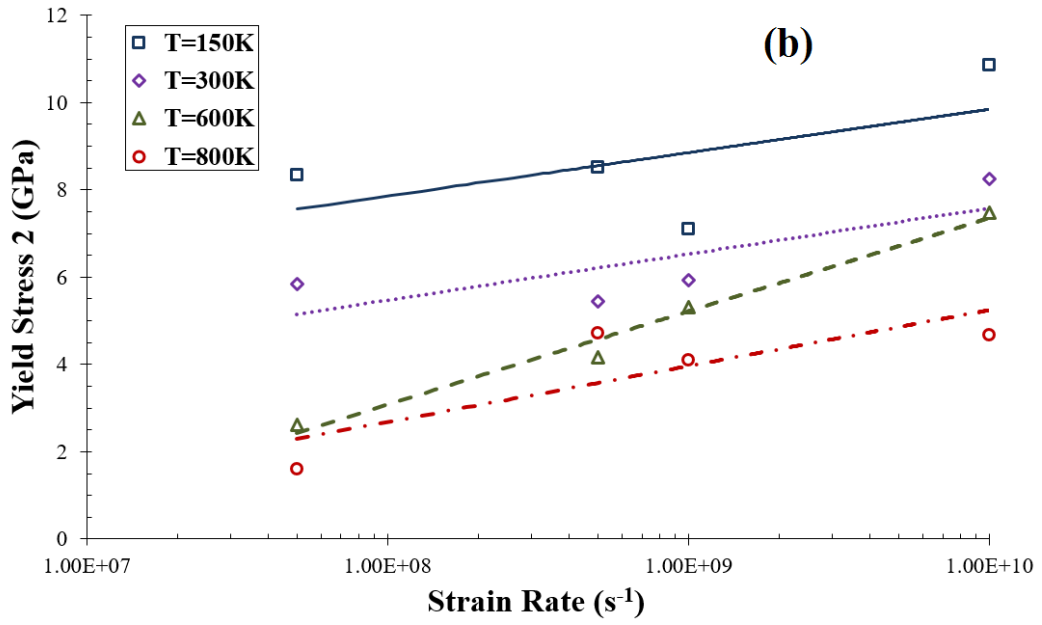
Figure 56 Al/Fe system stress as function of strain rate at different temperatures: (a) first yield (b) second yield, and (c) flow stresses.

All three stresses (yield 1, yield 2, and flow) are found to follow a logarithmic thermally activated model similar to the one proposed by Zhu et al. [134] (Figs. 56a and 56b). Equation 5 describes nucleation stress as the sum of two terms. The first and second terms represent the athermal stress and the thermally activated part of the stress, respectively, as

$$\sigma = \frac{Q^*}{V^*} - \frac{k_B T}{V^*} ln \frac{k_B T N v_0}{E \dot{\varepsilon} V^*} \tag{6}$$

where Q*/V* constitutes the athermal part of the nucleation stress and where V* is the activation volume and is approximated for each of the stresses, temperatures and strain rates [135] as

$$V^* = \sqrt{3} k_B T \frac{ln\dot{\varepsilon}}{\sigma} \tag{7}$$

When plotting stress as a function of strain rate such as in Figures 56a, 56b and 56c, the positive slope of the linear fits would then be equal to $\frac{k_B T}{V^*}$. The intercept of the different fits is equal to $\sigma_a - \frac{k_B T}{V^*} ln\dot{\varepsilon}_0(V^*, T)$, where the athermal stress is constant for all the cases and the second term is both function of the activation volume and the temperature.

For each of the system temperatures, a logarithmic fit was obtained as function of strain rate thus indicating a thermally activated process. The fitting equations and correlation coefficient values are listed in Table 17, Table 18, and Table 19 for yield 1, yield 2 and flow, respectively. Nucleation stresses follow a thermally activated model due to the fact that even in the case of an interface, and not a single crystal material, the first yield point represents the nucleation of dislocations, here in FCC aluminum, and

141

the second in BCC iron. The nucleation of dislocations occurs in the aluminum region with no apparent effect of the interface especially that the nucleation is homogeneous and takes place in the bulk for all temperatures and strain rates. Even though the nucleation process in iron also globally fits the thermal activation model, some minor concerns still rise especially at low temperatures where the lattice friction largely contributes to the overall nucleation stress and thus the low correlation coefficient at T=150K (Table 18). One additional concern is faced in the case of the second yield point, represented by the effect of the interface which was highlighted previously specifically by the heterogeneous nucleation of the dislocations taking place at the interface. Taking this into account, the nucleation stress in both regions can be considered as a thermally activated process guided by dislocation nucleation and motion.

Table 17 Yield 1 stress thermally activated model: fitted equations and correlation coefficients for different temperatures

T (K)	Equation	R^2
150	$0.0836\ln(x) + 4.4587$	0.8968
300	$0.0672\ln(x) + 4.6663$	0.937
600	$0.1193\ln(x) + 3.3673$	0.9681
800	$0.1347\ln(x) + 2.5321$	0.8999

Table 18 Yield 2 stress thermally activated model: fitted equations and correlation coefficients for different temperatures

T (K)	Equation	R^2
150	0.4251ln(x) - 0.0197	0.3601
300	0.4583ln(x) - 2.9697	0.6152
600	0.9284ln(x) - 14.021	0.9823
800	0.5566ln(x) - 7.57	0.6787

Table 19 Flow stress thermally activated model: fitted equations and correlation coefficients for different temperatures

T (K)	Equation	R^2
150	0.0806ln(x) + 1.6248	0.9119
300	0.1886ln(x) - 0.9022	0.9877
600	0.1405ln(x) - 0.2902	0.9968
800	0.1298ln(x) - 0.4191	0.7557

For fitting flow stress values, the thermally activated model was also found to be capable of predicting the obtained MD data points for the strain rates between $5.0\times10^7\text{s}^{-1}$ and $1.0\times10^{10}\text{s}^{-1}$. This may be explained by the fact that the flow stress represents an explicit response of the entire system, or in other terms, a response of both the Al and Fe regions combined with the effect of the incoherent interface between them.

The competition between the hardening and softening effects of temperature and strain rate is once more highlighted in the MD data points of the flow stress; at a fixed strain rate, flow stress was shown to decrease with increasing temperature thus putting forward the softening effect of this parameter previously reported given the

decrease in the lattice friction and of the ratio $\dot{\varepsilon}/\dot{\varepsilon_0}$ which yields a decrease of the overall

stress according to equation 6. At a fixed temperature, the flow stress increases linearly

with $ln\dot{\varepsilon}$. This strain rate hardening can again be associated with the increase of the drag

coefficient with the dislocation glide velocity (Equation 4 & 5). This thermal softening

effect [55] and strain rate hardening effect [76] due to the increase in phonon drag on

the flow stress are both reported in the available models in the literature. In other

presented models for flow stress as a function of strain rate in the case of pure metals, a

strain rate sensitivity exponents ranging from 0.184 to 0.43 is reported [55,76–

78,80,81]. Such a power model did not fit the data points of this study which may be

attributed to the presence of an incoherent interface between the FCC aluminum and

BCC iron which is considered as a barrier to the motion of dislocations and contributes

by itself to the hardening of a system. A linear behavior with the flow stress is reported

in the works of Armstrong and Li [136] for aluminum and Aramco iron.

E. DISCUSSION

The flow stress of the Al/Fe interface system, which is the only indication of

the response of the system as an entirety, was found to follow the same thermally

activated model as the responses of the different metals constituting this system, which

are underlined by the first and second yield points in the range of temperature and strain

rate employed in this study. While nucleation in the "weaker" material (Al) takes place

in the bulk, the mechanism differed when it came to the second "stronger" (Fe) material.

The migration of dislocations from the bulk of the aluminum region to the interface and

their accumulation there favored the nucleation at the interface when it came to the

relaxation in iron. Following the relaxation in aluminum and the drop in the stress,

hardening is observed on the stress strain plots shown in Figure 47. At this strain level the microstructure history evolution of the system displays different types of junctions and jogs analyzed in Figure 52. These sessile dislocations (e.g., Hirth and Frank locks and Stair-Rod) accompanied by the blockage of motion of the dislocations due to the presence of the incoherent interface result in the observed hardening following the relaxation in the aluminum. Evidence of the decrease of the yield stress in iron due to the decrease in lattice friction beyond the critical temperature was also observed on the stress strain plots thus leading to the merging between the first and second yield points as temperature and strain rate increased. Once nucleated, edge and mixed dislocations are more abundant in the aluminum side whereas screw dislocations are found in the iron region. While the density of these dislocations is found to be independent of the temperature, it was found to increase with increasing strain rate which is due to the increase in phonon drag and thus the hindering in the dislocation motion and multiplication.

For all temperatures and strain rates considered here, the first and second yield stresses as well as the flow stress were investigated in order to correlate their behavior to theoretical models. They were all found to follow a thermally activated model. For temperature of 300K, Figures 57a and 57b contrast the behavior of yield stress points 1 and 2, respectively, for the Al/Fe system to the behavior of different Al and Fe crystals reported in the literature.

The thermally activated model for yield 1 indicates the relaxation in the Al region (Figure 57a) of the system in which yield stress increases linearly with $ln\dot{\varepsilon}$ with a slope equal to $\frac{k_B T}{V^*}$. For pure aluminum, power models of yield stress as function of strain rate are reported in the literature (Swegle and Grady [137], Crowhurst [138] and

Smith et al. [76]). MD-generated data values are larger than those obtained in the ramp compression reported by Smith et al. [76] and shock experiments by Swegle and Grady [137] and Crowhurst [138] for aluminum samples. In the case of Smith et al. [76], this could be due to the presence of defects and the preexisting dislocations in the experimental samples versus their absence in the MD system. In comparison the difference between the MD reported data and those from shock experiments (Swegle and Grady [137] and Crowhurst [138]) are due to the difference in the general state of stress with the one used in MD; the shock experiments generate a three dimensional state of stress with very short rise time as compared to the uniaxial compression. This results in yielding of the samples before the maximum stress is reached although it cannot be detected in the stress strain response due to the short rise time. A conversion between the peak stress and the yield stress can be achieved using the maximum shear stress theory. Finally, the effect of the interface in the case of aluminum is not a major factor to be taken into account since the nucleation occurs from the bulk when the nucleation stress is reached.

On the other hand, Figure 57b contrasts the values of the second yield stress from the MD data to different works reported in the literature. Although the nucleation of dislocations in the former takes place heterogeneously from the interface, the proposed model (Equation 4) for the relaxation in the BCC iron region of the system is found to follow the same trend as that advanced by El Ters and Shehadeh [55] for lower strain rates. This is an indication of the similarities between the Al/Fe interface system and the behavior of a pure BCC iron. The MD generated data points are found to fall between the literature models presented by Smith et al. [76]. The lower stress values reported by Smith et al. [76] are likely due to the preexisting dislocations in the Fe

sample tested under ramp compression. In this case too, the effect of the interface is not put forward given the similar response between the work of El Ters and Shehadeh [55] and the one reported in this study.

Finally, in Figure 57c, and since there is no comparable Al/Fe interface work in the literature, the flow stress model proposed for the Al/Fe interface system is compared to other available models in the literature for the flow stress of pure Al and pure Fe separately all taken at 300K. The proposed trend appears parallel to both Zerilli Armstrong (ZA) pure Fe [139] model and ZA- AA5083[140] with values of stress midway between Al- and Fe- materials. This here puts forward the effect of the interface and suggests that the behavior of the Al/Fe system is that of average values to those of pure materials from which it is composed.
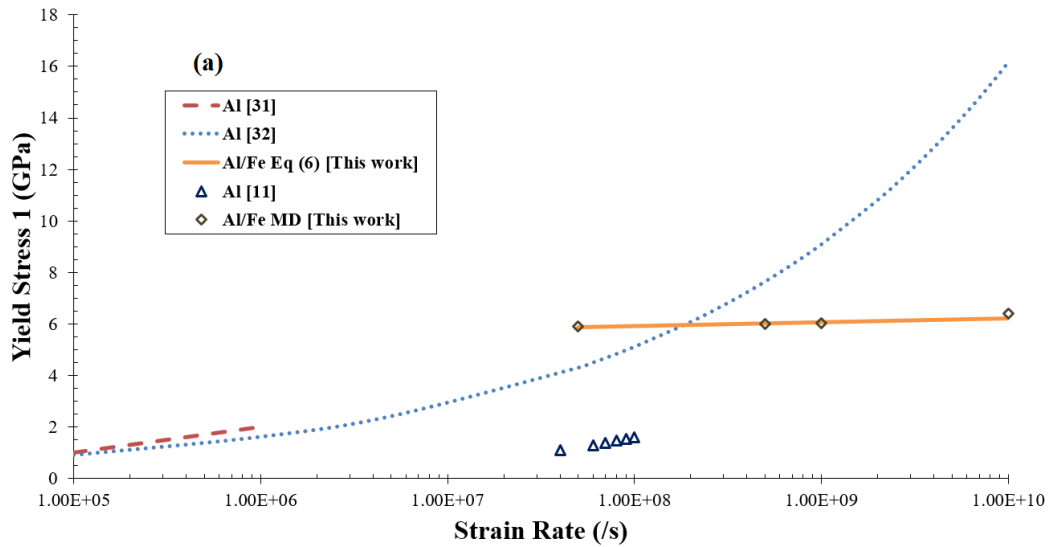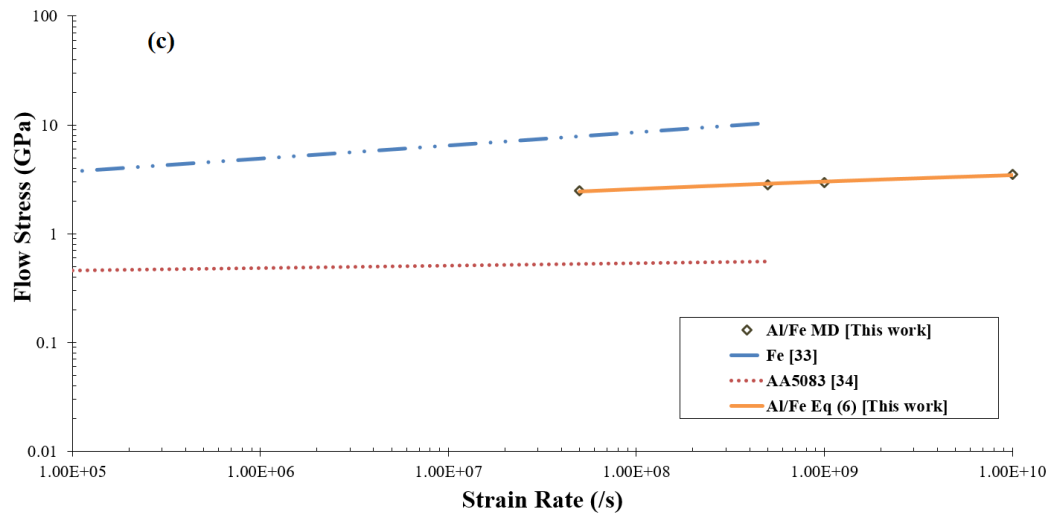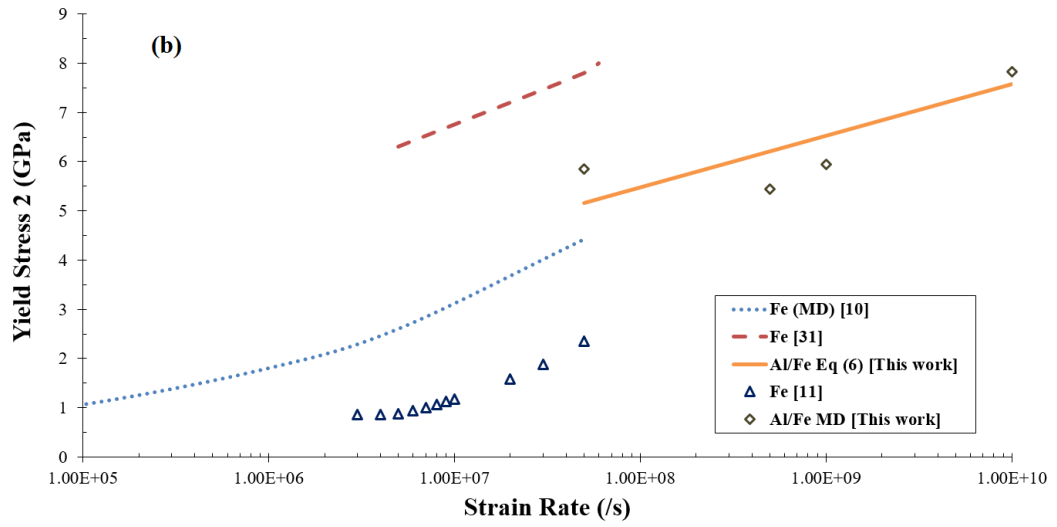
Figure 57 Contrasts of (a) Yield 1, (b) Yield 2, and (c) Flow Stress for Al/Fe system against literature reported for Al and Fe.

CHAPTER VII

MOLECULAR DYNAMICS SIMULATIONS OF MIXING AT AN INCOHERENT INTERFACE CONDUCTED BY A NANOMETRIC TOOL

With an eye on the nano-engineering applications more so developed in the recent years in the scientific world, a numerical approach using MDS is conclusively proposed in the following aiming to model extreme rotational loading conditions similar to those found during FSW and resulting in the mixing at the interface between Al and Fe regions at the nanometric level. This was achieved through the use of a rigid undeformable nanometric tool moving at different process parameters. These simulations derive from the previous study of the behavior of the Al/Fe pristine interface under compressive loading and as a conclusive proposition to the multi-scale analysis of the many state variables found in a FSW process, starting with experimental investigation to molecular dynamics, passing through finite elements modelling.

Moreover, the deformation mechanism at the interface, as a result of the severe plastic work induced by this tool is observed and nucleation of dislocations analyzed along with the structure of the subsequent mixed region between the two materials.

A. METHODOLOGY AND THEORY

A molecular dynamics model under LAMMPS [102] was developed to model the mixing found at the incoherent interface formed by pure Al and pure Fe conducted by the movement of a nanometric tool at different rotational speeds and advancing feeds. The same embedded atom method (EAM) potential proposed by Mendelev [110] is again adopted to simulate the interactions between the Al-Al, Fe-Fe and Al-Fe atoms.

Each of the Al and Fe regions, hereunder referred to as Al and Fe plates, were sized 17 nm x 10.2 nm x 4.3 nm. A rigid undeformable region, with a precise geometry containing both a shoulder and a pin, is proposed as the tool and serves for the mixing between the two plates. The geometry of this tool aims to increase the mixing through mechanical deformation induced by the "threading" imposed to the tool region. The thickness and height of the first blade (the one closest to the shoulder) are larger than the second one which in turn are larger than the third blade. These dimensions were chosen such that the largest thickness (of the first blade) would still be smaller than the potential cutoff so that the two regions (Al and Fe) would not be extremely spaced by the traversing of the tool and would still feel the presence of their respective neighbor after the tool has passed. The crystallographic orientation of the two crystals is chosen such that the atom spacing mismatch between the two lattices is minimized (Chapter 3F- Figure 46). The simulations were conducted in three phases. (1) First, the minimization step where the system energy is brought down to a minimum under 30000 steps at 0K. After that, (2) the system is equilibrated at room temperature over 500000 steps. Finally, the loading step (3) taken from 300K where the rigid tool plunges (in the –z direction) at the interface between the two plates while rotating at 0.01deg/fs (or the equivalent of $1.67*10^{12}$RPM) up until a specified depth of 58Å and then advances with a speed equal to 0.0001 Å/fs (or the equivalent of 600m/min) across the interface (in the –y direction). A simulation timestep equal to 1fs is adopted during all the process. The simulated system is shown in Figure 58.
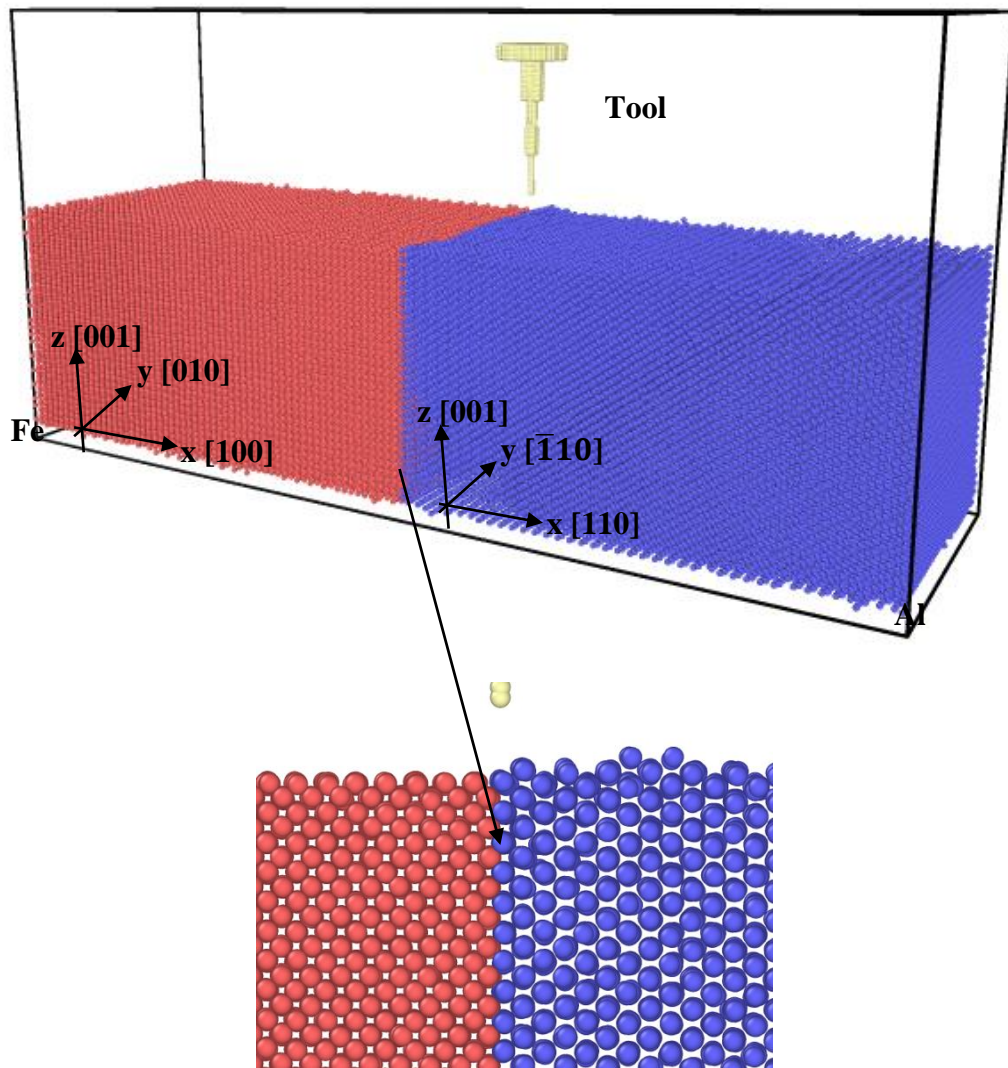
Figure 58 Simulation system and plates orientations

B. RESULTS

1. Dislocation nucleation and growth mechanisms

Following energy minimization and equilibrium of the system at room temperature, misfit dislocations were detected in the aluminum FCC region at the interface between the two regions. The stress field applied to the system is generated solemnly by the tool; this was reflected in the concentration of the dislocations around the pin of this tool which penetrated between the two regions. These dislocations which

first appeared at the interface in the FCC region only were capable of transmitting into the BCC region following the rotational movement of the tool. Figure 59 show the progression and propagation of the dislocations from the FCC region to the BCC region around the pin of the tool.
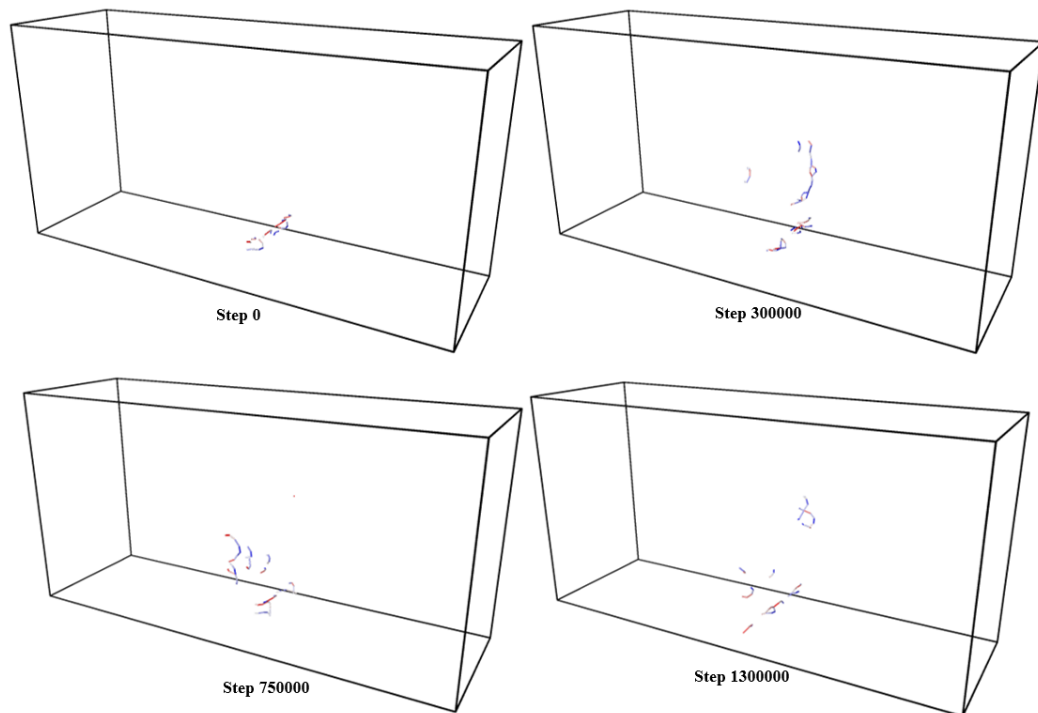
Figure 59 Dislocation progression around the tool

2. *RDF and mixing at the interface*

The RDF represents the primary method to evaluate the resultant structure potentially formed after the mixing lead by the tool. It was found that following the passage of the tool little difference could be recognized between the RDF of the interface. Figures 60, 61 and 62 show three RDFs; the first one (Figure 60) represents the entire interface over a range of x=-15 to 15Å which constitutes mainly the width of the shoulder of the tool. Figure 61 focuses on the mixing resulting from the effect of the shoulder alone; in this plot the width of the shoulder is considered (-12 to 12Å in the x

direction) and a very thin layer on the top of the surface (~5Å thick layer in the z

direction). In the final plot (Figure 62) the effect of the pin is shown. In this last plot, the

considered width of the interface is restrained to that of the upper blades more or less (-

5 to 5Å in the x direction).
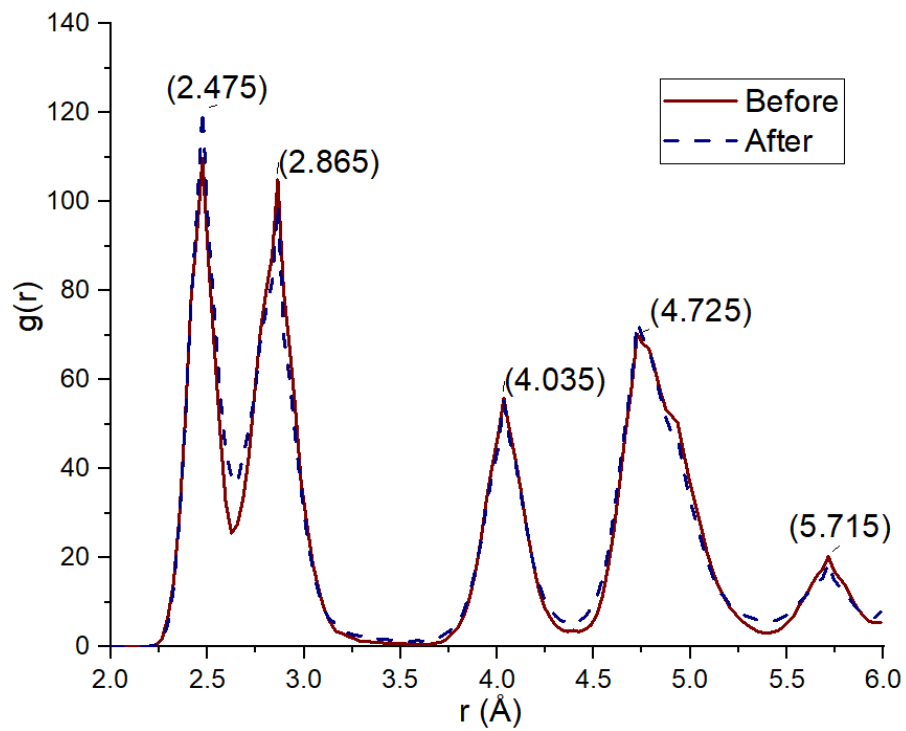
Figure 60 RDF of the interface (from -15Å to 15Å in the x direction) before and after
passage of the tool
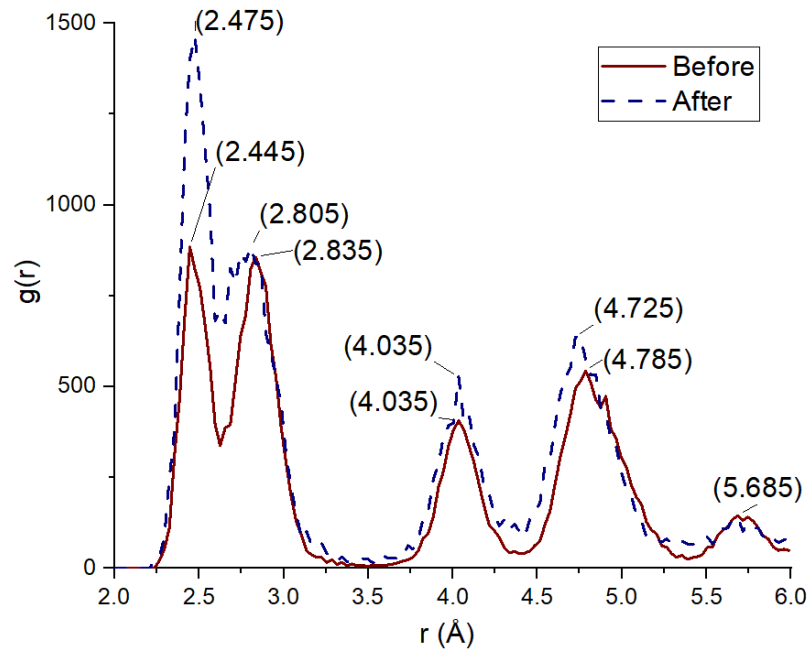
Figure 61 Effect of the tool shoulder as found from the RDF
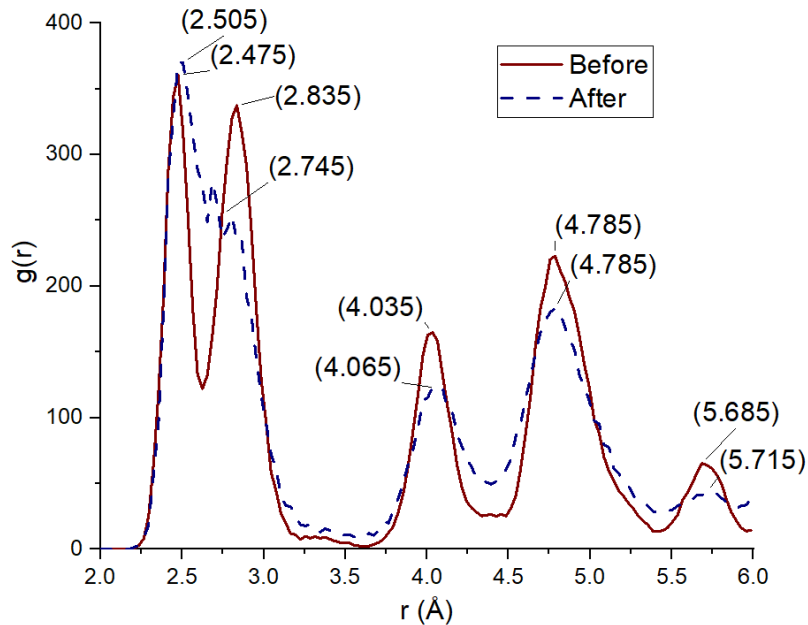
Figure 62 Effect of the pin as found from the RDF

Based on the RDF results, it can be deduced that no intermetallic compounds were created at the interface following the passing of the rigid tool. This was previously insinuated by the limited dislocation movement shown in Figure 59. Additionally, the absence of creation of any intermetallic compound can be explained by the geometrically narrow region to which the deformation is imposed through the encounter

with the tapered tool. Another reason for these results can be explained by the very high speed of deformation imposed through the movement of the tool and which does not give the structure enough time to form.

On the other hand, the mixing between the two regions, namely Al and Fe, is evaluated using the scatter plot modifications from OVITO. This plot shown in Figures 63a and 63b reveals the scattered positions of the aluminum and iron atoms across the interface before (Figure 63a) and after (Figure 63b) the tool has passed thus showing the amount of mixing that has taken place between the two regions. It can be seen that originally the interface was set precisely at 0 and the aluminum atoms (blue) were distributed in the positive range (from 0 to 175 on the position X scale) and the iron atoms (red) were distributed in the negative region (from -175 to 0 on the position X scale). At the end of the simulation, it can be noticed that the aluminum atoms (placed in the advancing side) have penetrated the iron region by a distance of approximately 24Å, whereas the iron atoms have penetrated the aluminum region by close to 18Å. This is also observed in experimental FSW where the advancing side material is found to penetrate more in the retreating side than the other way around. These results imply that the tool contributed to the deformation of the pristine interface by mixing the atoms together even though a predefined compound structure could not be defined as it was mentioned earlier.
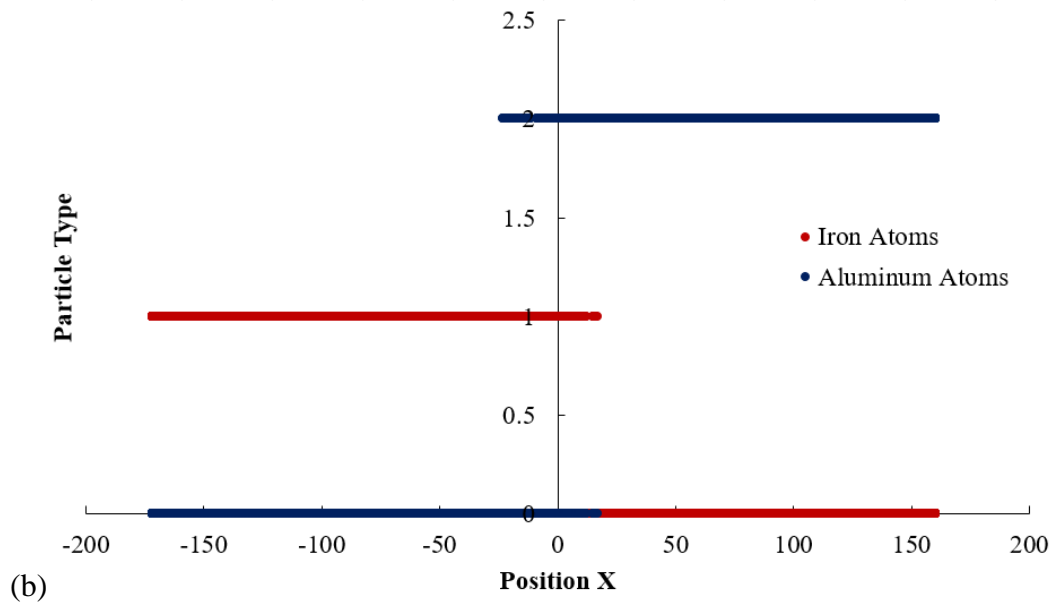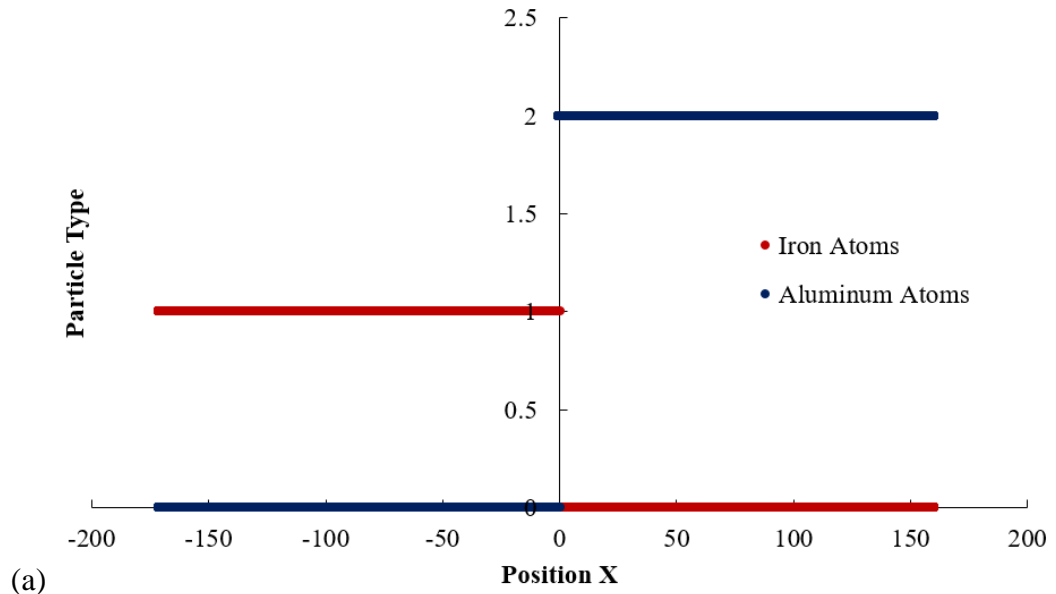
Figure 63 Scatter plot of the Aluminum and Iron atoms across the interface (a) before and (b) after the passage of the tool.

This simulation resulted in the surface mesh shown in Figure 64. The gap between the two materials was remarkably decreased, as compared to preliminary simulations, and a satisfactory mixing between the atoms was observed.
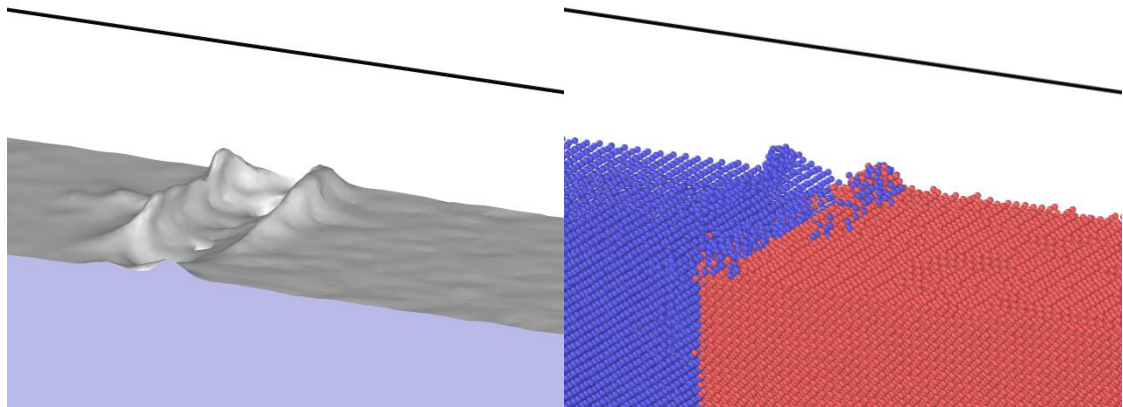
Figure 64 Surface mesh after the end of the simulation

C. DISCUSSION

Although the presented simulation still lacks some improvements, it has shown mixing and movement of the atoms from the AS to the RS, and vice versa, as a result of the rotation of a rigid tool at its interface. A stable structure between the mixed atoms was not detected at the end of the simulation. One of the main reasons behind this is the very short total computational time which does not give the structure enough time to form or the atoms to be placed at specific locations. Additionally, the tool's rotational speed and advancing also could also be another reason to the lack of formation of the intermetallic compound. However, the presence of misfit dislocations is detected even prior to the start of the process and therefore contribute to the deformation mechanism and facilitate the movement of the atoms out of their stable positions. It was found that the dislocations are reduced to the pin area which was always presented as the highest deformation area during the process.

157

CHAPTER VIII

CONCLUSIONS

In this dissertation, a multiscale approach to resolving the challenges arising from the FSW process are investigated and presented. First experimentally, many intermetallic compounds were detected between the dissimilar materials welded using this process. The mechanical properties of these compounds confirm their contribution to the weakening of the strength of the welds when formed. Given the presence of these IMCs, the different joints were assessed mechanically in tension and impact and compared to the un-welded original metals that form them. Secondly, the process of FSW was reproduced numerically using the FEM tool Deform; this allowed the execution of several simulations in time and cost effective manners. In addition, the proposed simulations allowed the investigation of different state variables in the weld nugget, usually very hard to do experimentally. The validation of the simulation was performed by comparing the temperature profiles of reference points in the system to their experimentally measured temperatures. Improvements to these simulations could be realized especially in the resulting volume fraction of the weld line; this could be achieved through the creation of user sub routines that take into account continuous transformation and temperature plots between the two materials (or phases) that are being welded using this technique. Such plots could also lead to the exact location of the detected IMCs and thus a set of process parameters can be proposed such that they are reduced to a minimum in order to improve on the mechanical properties of the joints.

On the other hand, MD simulations are conducted to study the mechanical response, interfacial mixing, and evolved intermetallic structure(s) in a solid-state Al (FCC) / Fe (BCC) system under uniaxial compression applied at a constant strain rate of 5×10^7 s^{-1} and five temperatures ranging from 150K to 900K. At this molecular scale, misfit dislocations were identified at the interface in the aluminium region. These contribute to the deformation mechanism and present a favourable site to the propagation of extended dislocations in the bulk of the two regions. The mechanical response of the system validates this theory with a multiple relaxation stresses behaviour. One stress peak is attributed to the nucleation of dislocations from the misfit dislocation sites in aluminium. These dislocations are considered high distortion regions around the interface. Other stress is attributed to bulk nucleation in aluminium and to interface nucleation of dislocations from the interface in iron. These three specific stresses are all found to decrease with increasing temperatures. Moreover, observed interfacial mixing is evaluated using the Mean Squared Displacement (MSD) method in LAMMPS. Dislocations on both sides of the solid Al/Fe system are observed to multiply and grow shortly at the same strain levels corresponding to concurrent relaxations in the stress-strain plots. Under the prescribed conditions of compression stress and temperatures, the radial distribution function (RDF) analysis of the atomic disposition of Al and Fe atoms indicates that the most favourable positions these atoms would assume are that of the FeAl intermetallic compound (CsCl crystal structure).

Adopting another Al-FCC configuration, another MD study reports on the mechanical response of this Al/Fe interface subject to compression at wide ranging conditions of temperature and strain rates between 150K and 900K and between 5.0×10^7 s^{-1} and 1.0×10^{10} s^{-1}, respectively. For the specific orientation of the two crystals,

the simulations generated stress strain data which were used to extract the yield and flow stresses. Thermally activated empirical equations are then recommended for the prediction of these stresses whereby $\sigma_{nuc} = \sigma_a + \frac{k_B T}{V^*} ln \frac{\dot{\varepsilon}}{\dot{\varepsilon}_0(T,V^*)}$. The first component of this equation being (sigma athermal) independent of both temperature and strain rate, the overall nucleation stress was found to decrease with increasing temperature due to the increase of $\dot{\varepsilon}_0$. Thus two competing mechanisms are faced during the loading at these extreme conditions namely temperature softening and strain rate hardening. A decrease of the lattice friction favors the thermal softening up until the critical temperature in iron faced by an increase in phonon drag with $ln\dot{\varepsilon}$. Dislocation density plots generated from the simulations confirms the effect of strain rate on this model with an increase in the saturation density with increasing strain rate in accordance with the increase in phonon drag. The relaxation in the Fe region of the Al/Fe interface system, highlighted by the behavior of the second yield point, showed similar results to a pure Fe system unlike what was reported in the literature for the case of an aluminum sample under shock compression which showed lower values of stress than the MD-generated data. This is likely due to the presence of the incoherent interface and the preexisting dislocations in the shocked samples as opposed to their absence in the MD simulations. The flow stress model of the interface was found to fall midway between ZA models for pure iron and AA5083 aluminum indicating an equally mixed behavior of the interface between the two single materials constituting it.

Finally, the results and conclusions of the previous simulations were reorganized in an effort to propose a preliminary simulation that models the mixing at an incoherent interface as which results from the passing of a rigid tool between the dissimilar regions at the molecular level. Such a simulation aims to shed light on the deformation

mechanism found under this complex state of stress. The first dislocations detected at this interface were again misfit dislocations due to the difference between the atomic spacing and structures of the Al and Fe crystals. It was found that these dislocations were at all-time concentrated around the pin of the tool and were able to cross the opaque interface, from the FCC region where they were first created to the BCC region, through the movement of this rigid body.

APPENDIX

ABBREVIATIONS

FSW	Friction stir welding
DFSW	Dissimilar Friction Stir Welding
FSP	Friction Stir Processing
HAZ	Heat affected zone
SZ	Stirring zone
EDX	Energy Dispersive X-ray
XRD	X-ray Diffraction
MD	Molecular dynamics
MDS	Molecular Dynamics Simulations
WP	Workpiece
BP	Backing plate
FE	Finite elements
FEM	Finite elements modelling
IMC	Intermetallic compound
CNC	Computer numerical control
LAMMPS	Large atomic/molecular massive parallel simulations
FGM	Functionally graded materials
RDF	Radial Distribution function
ALE	Arbitrary Lagrangian-Eulerian
CEL	Coupled Eulerian-Lagrangian
IR	Infrared
CS	Cross-section
VM	Von-Mises
JC	Johnson-Cook
ST	Sellars-Tegart
ZA	Zerilli-Armstrong

BIBLIOGRAPHY

[1]   W.M. Thomas, E.D. Nicholas, J.C. Needham, M.G. Murch, P. Templesmith, C.J. Dawes, Friction Stir Welding, PCT/GB92/02203-No. 9125978.8., 1991.

[2]   DAWES, C. J., Friction Stir Joining of Aluminium Alloys, Bulletin. 6 (1995). http://ci.nii.ac.jp/naid/10006401749/en/ (accessed February 13, 2020).

[3]   M. Zaenudin, M.N. Abdulrazaq, S.S. Al-Zubaidi, Molecular dynamics simulation of welding and joining processes: An overview, Int. J. Eng. Technol. 7 (2018) 3816–3825. https://doi.org/10.14419/ijet.

[4]   A.H. Kheireddine, A.H. Ammouri, R.F. Hamade, G.T. Kridli, Fem analysis of the effects of cooling techniques on the microstructure of aluminum 7075 friction stir welded joints, ASME Int. Mech. Eng. Congr. Expo. Proc. 3 (2012) 913–917. https://doi.org/10.1115/IMECE2012-88943.

[5]   A.H. Ammouri, H. Achdjian, A. Dorbane, G. Ayoub, G.T. Kridli, R.F. Hamade, Characterization of optimized friction stir welded twin roll cast AZ31B sheets, in: Int. Mech. Eng. Congr. Expo., Montreal, Canada, 2014.

[6]   A. Dorbane, G. Ayoub, B. Mansoor, R.F. Hamade, G. Kridli, R. Shabadi, A. Imad, Microstructural observations and tensile fracture behavior of FSW twin roll cast AZ31 Mg sheets, Mater. Sci. Eng. A. 649 (2016) 190–200. https://doi.org/10.1016/j.msea.2015.09.097.

[7]   S. Ugender, A. Kumar, A.S. Reddy, Microstructure and Mechanical Properties of AZ31B Magnesium Alloy by Friction Stir Welding, Procedia Mater. Sci. 6 (2014) 1600–1609. https://doi.org/10.1016/j.mspro.2014.07.143.

[8]   A. Esmaeili, H.R. Zareie Rajani, M. Sharbati, M.K.B. Givi, M. Shamanian, The role of rotation speed on intermetallic compounds formation and mechanical behavior of friction stir welded brass/aluminum 1050 couple, Intermetallics. 19 (2011) 1711–1719. https://doi.org/10.1016/j.intermet.2011.07.006.

[9]   V. Firouzdor, S. Kou, Al-to-Mg friction stir welding: Effect of material position, travel speed, and rotation speed, Metall. Mater. Trans. A Phys. Metall. Mater. Sci. 41 (2010) 2914–2935. https://doi.org/10.1007/s11661-010-0340-1.

[10]   P. Pourahmad, M. Abbasi, H.A. Mehrabi, Bimetal Friction Stir Welding of Aluminum to Magnesium, 1 (2013) 27–38.

[11]   Y.S. Sato, S.H.C. Park, M. Michiuchi, H. Kokawa, Constitutional liquation during dissimilar friction stir welding of Al and Mg alloys, Scr. Mater. 50 (2004) 1233–1236. https://doi.org/10.1016/j.scriptamat.2004.02.002.

[12]   A.C. Somasekharan, L.E. Murr, Microstructures in friction-stir welded dissimilar magnesium alloys and magnesium alloys to 6061-T6 aluminum alloy, Mater.

Charact. 52 (2004) 49–64. https://doi.org/10.1016/j.matchar.2004.03.005.

[13] M.A. Mofid, F.M. Ghaini, The effect of water cooling during dissimilar friction stir welding of Al alloy to Mg alloy, Mater. Des. 36 (2012) 161–167. https://doi.org/10.1016/j.matdes.2011.11.004.

[14] M. Dehghani, A. Amadeh, S.A.A. Akbari Mousavi, Investigations on the effects of friction stir welding parameters on intermetallic and defect formation in joining aluminum alloy to mild steel, Mater. Des. 49 (2013) 433–441. https://doi.org/10.1016/j.matdes.2013.01.013.

[15] W. Liu, J. Ma, M. Mazar Atabaki, R. Kovacevic, Joining of advanced high-strength steel to AA 6061 alloy by using Fe/Al structural transition joint, Mater. Des. 68 (2015) 146–157. https://doi.org/10.1016/j.matdes.2014.12.028.

[16] C.M. Chen, R. Kovacevic, Joining of Al 6061 alloy to AISI 1018 steel by combined effects of fusion and solid state welding, Int. J. Mach. Tools Manuf. 44 (2004) 1205–1214. https://doi.org/10.1016/j.ijmachtools.2004.03.011.

[17] X. Liu, S. Lan, J. Ni, Analysis of process parameters effects on friction stir welding of dissimilar aluminum alloy to advanced high strength steel, Mater. Des. 59 (2014) 50–62. https://doi.org/10.1016/j.matdes.2014.02.003.

[18] K. Kimapong, T. Watanabe, Friction stir welding of aluminum alloy to steel, Weld. J. (Miami, Fla). 83 (2004) 277–282.

[19] H. Uzun, C. Dalle Donne, A. Argagnotto, T. Ghidini, C. Gambaro, Friction stir welding of dissimilar Al 6013-T4 To X5CrNi18-10 stainless steel, Mater. Des. 26 (2005) 41–46. https://doi.org/10.1016/j.matdes.2004.04.002.

[20] T. Tanaka, T. Morishige, T. Hirata, Comprehensive analysis of joint strength for dissimilar friction stir welds of mild steel to aluminum alloys, Scr. Mater. 61 (2009) 756–759. https://doi.org/10.1016/j.scriptamat.2009.06.022.

[21] Y.N. Zhang, X. Cao, S. Larose, P. Wanjara, Review of tools for friction stir welding and processing, Can. Metall. Q. 51 (2012) 250–261. https://doi.org/10.1179/1879139512Y.0000000015.

[22] S. Rajakumar, C. Muralidharan, V. Balasubramanian, Influence of friction stir welding process and tool parameters on strength properties of AA7075-T6 aluminium alloy joints, Mater. Des. 32 (2011) 535–549. https://doi.org/10.1016/j.matdes.2010.08.025.

[23] S. Malarvizhi, V. Balasubramanian, Influences of tool shoulder diameter to plate thickness ratio (D/T) on stir zone formation and tensile properties of friction stir welded dissimilar joints of AA6061 aluminum-AZ31B magnesium alloys, Mater. Des. 40 (2012) 453–460. https://doi.org/10.1016/j.matdes.2012.04.008.

[24] Y.H. Zhao, S.B. Lin, L. Wu, F.X. Qu, The influence of pin geometry on bonding and mechanical properties in friction stir weld 2014 Al alloy, Mater. Lett. 59

(2005) 2948–2952. https://doi.org/10.1016/j.matlet.2005.04.048.

[25]   M. Simoncini, A. Forcellese, Effect of the welding parameters and tool configuration on micro- and macro-mechanical properties of similar and dissimilar FSWed joints in AA5754 and AZ31 thin sheets, Mater. Des. 41 (2012) 50–60. https://doi.org/10.1016/j.matdes.2012.04.057.

[26]   N. Dialami, M. Cervera, M. Chiumenti, C. Agelet de Saracibar, A fast and accurate two-stage strategy to evaluate the effect of the pin tool profile on metal flow, torque and forces in friction stir welding, Int. J. Mech. Sci. 122 (2017) 215–227. https://doi.org/10.1016/j.ijmecsci.2016.12.016.

[27]   P. Motalleb-nejad, T. Saeid, A. Heidarzadeh, K. Darzi, M. Ashjari, Effect of tool pin profile on microstructure and mechanical properties of friction stir welded AZ31B magnesium alloy, Mater. Des. 59 (2014) 221–226. https://doi.org/10.1016/j.matdes.2014.02.068.

[28]   L. Long, G. Chen, S. Zhang, T. Liu, Q. Shi, Finite-element analysis of the tool tilt angle effect on the formation of friction stir welds, J. Manuf. Process. 30 (2017) 562–569. https://doi.org/10.1016/j.jmapro.2017.10.023.

[29]   F. Al-Badour, N. Merah, A. Shuaib, A. Bazoune, Coupled Eulerian Lagrangian finite element modeling of friction stir welding processes, J. Mater. Process. Technol. 213 (2013) 1433–1439. https://doi.org/10.1016/j.jmatprotec.2013.02.014.

[30]   C. Blignault, D.G. Hattingh, M.N. James, Optimizing Friction Stir welding via statistical design of tool geometry and process parameters, J. Mater. Eng. Perform. 21 (2012) 927–935. https://doi.org/10.1007/s11665-011-9984-2.

[31]   C.S. Wu, W. Bin Zhang, L. Shi, M.A. Chen, Visualization and simulation of plastic material flow in friction stir welding of 2024 aluminium alloy plates, Trans. Nonferrous Met. Soc. China (English Ed. 22 (2012) 1445–1451. https://doi.org/10.1016/S1003-6326(11)61339-3.

[32]   K. Li, D.K. Aidun, P. Marzocca, Modeling of the mixed weld zone of dissimilar metals joint by functionally graded materials, STEEL GRIPS J. Steel Relat. Mater. 6 (2008) 58–68.

[33]   K. Li, D. Aidun, P. Marzocca, No Title3-D thermo-mechanical analysis of Friction Stir Welding of dissimilar metals using functionally graded material concept, in: ASM Proc. Int. Conf. Trends Weld. Res., 2009: pp. 726–730.

[34]   K. Li, D. Aidun, P. Marzocca, Time-varying Functionally Graded Material thermal modeling of friction stir welding joint of dissimilar metals, in: ASM Proc. Int. Conf. Trends Weld. Res., 2009: pp. 731–735.

[35]   S. Xu, X. Deng, A.P. Reynolds, T.U. Seidel, Finite element simulation of material flow in friction stir welding, Sci. Technol. Weld. Join. 6 (2001) 191–193. https://doi.org/10.1179/136217101101538640.

[36] H. Schmidt, J. Hattel, A local model for the thermomechanical conditions in friction stir welding, Model. Simul. Mater. Sci. Eng. 13 (2005) 77–93. https://doi.org/10.1088/0965-0393/13/1/006.

[37] H. Jamshidi Aval, S. Serajzadeh, A.H. Kokabi, Evolution of microstructures and mechanical properties in similar and dissimilar friction stir welding of AA5086 and AA6061, Mater. Sci. Eng. A. 528 (2011) 8071–8083. https://doi.org/10.1016/j.msea.2011.07.056.

[38] B.B. and K.G.K.M. M Satya Narayana Gupta, FINITE ELEMENT MODELING AND THERMO- MECHANICAL ANALYSIS OF FRICTION STIR WELDED Al / Cu BIMETALLIC LAP JOINTS, Int. J. Mech. Eng. Robot. Res. 1 (2012) 165–173.

[39] R. Hamilton, D. Mackenzie, H. Li, Multi-physics simulation of friction stir welding process, Eng. Comput. (Swansea, Wales). 27 (2010) 967–985. https://doi.org/10.1108/02644401011082980.

[40] E. zhi GAO, X. xing ZHANG, C. zhong LIU, Z. yi MA, Numerical simulations on material flow behaviors in whole process of friction stir welding, Trans. Nonferrous Met. Soc. China (English Ed. 28 (2018) 2324–2334. https://doi.org/10.1016/S1003-6326(18)64877-0.

[41] A.H. Ammouri, R.F. Hamade, A relation between grain size and process parameters in friction stir processing of AZ31B, Int. J. Appl. Eng. Res. 8 (2013) 977–982.

[42] C.I. Chang, C.J. Lee, J.C. Huang, Relationship between grain size and Zener-Holloman parameter during friction stir processing in AZ31 Mg alloys, Scr. Mater. 51 (2004) 509–514. https://doi.org/10.1016/j.scriptamat.2004.05.043.

[43] A.H. Ammouri, R.F. Hamade, On the selection of constitutive equation for modeling the friction stir processes of twin roll cast wrought AZ31B, Mater. Des. 57 (2014) 673–688. https://doi.org/10.1016/j.matdes.2014.01.057.

[44] Z. Zhang, H.W. Zhang, Numerical studies on controlling of process parameters in friction stir welding, J. Mater. Process. Technol. 209 (2009) 241–270. https://doi.org/10.1016/j.jmatprotec.2008.01.044.

[45] A.H. Ammouri, R.F. Hamade, Comparison of material flow stress models toward more realistic simulations of friction stir processes of Mg AZ31B, Adv. Mater. Res. 922 (2014) 18–22. https://doi.org/10.4028/www.scientific.net/AMR.922.18.

[46] B. Gurrutxaga-Lerma, M.A. Shehadeh, D.S. Balint, D. Dini, L. Chen, D.E. Eakins, The effect of temperature on the elastic precursor decay in shock loaded FCC aluminium and BCC iron, Int. J. Plast. 96 (2017) 135–155. https://doi.org/10.1016/j.ijplas.2017.05.001.

[47] M.H. Enayati, M. Salehi, Formation mechanism of Fe3Al and FeAl intermetallic compounds during mechanical alloying, J. Mater. Sci. 40 (2005) 3933–3938.

https://doi.org/10.1007/s10853-005-0718-4.

[48]   G. Temizel, M. Özenbaş, Intermetallic phase formation at Fe-Al film interfaces, Turkish J. Eng. Environ. Sci. 31 (2007) 71–78. https://doi.org/10.3906/tar-1204-38.

[49]   C.Y. Chung, Y.C. Chung, Molecular dynamics simulation of nano-scale Fe-Al thin film growth, Mater. Lett. 60 (2006) 1063–1067. https://doi.org/10.1016/j.matlet.2005.10.088.

[50]   P. Süle, D. Kaptás, L. Bujdosó, Z.E. Horváth, A. Nakanishi, J. Balogh, Chemical mixing at "al on Fe" and "fe on Al" interfaces, J. Appl. Phys. 118 (2015). https://doi.org/10.1063/1.4932521.

[51]   E. Fonda, A. Traverse, Evidence of intermixing at the Fe/Al interface in multilayers produced by metal vapor deposition at room temperature, J. Magn. Magn. Mater. 268 (2004) 292–297. https://doi.org/10.1016/S0304-8853(03)00537-7.

[52]   H. Hao, D. Lau, Atomistic modeling of metallic thin films by modified embedded atom method, Appl. Surf. Sci. 422 (2017) 1139–1146. https://doi.org/10.1016/j.apsusc.2017.05.011.

[53]   M. Liao, B. Li, M.F. Horstemeyer, Interaction between prismatic slip and a Mg17Al12 precipitate in magnesium, Comput. Mater. Sci. 79 (2013) 534–539. https://doi.org/10.1016/j.commatsci.2013.07.016.

[54]   L. Chang, C.Y. Zhou, H.X. Liu, J. Li, X.H. He, Orientation and strain rate dependent tensile behavior of single crystal titanium nanowires by molecular dynamics simulations, J. Mater. Sci. Technol. 34 (2018) 864–877. https://doi.org/10.1016/j.jmst.2017.03.011.

[55]   P. El Ters, M.A. Shehadeh, Modeling the temperature and high strain rate sensitivity in BCC iron: Atomistically informed multiscale dislocation dynamics simulations, Int. J. Plast. 112 (2019) 257–277. https://doi.org/10.1016/j.ijplas.2018.09.002.

[56]   A. Hassani, A. Makan, K. Sbiaai, A. Tabyaoui, A. Hasnaoui, Molecular dynamics study of growth and interface structure during aluminum deposition on Ni(1 0 0) substrate, Appl. Surf. Sci. 349 (2015) 785–791. https://doi.org/10.1016/j.apsusc.2015.05.076.

[57]   B. Wu, J. Zhou, C. Xue, H. Liu, Molecular dynamics simulation of the deposition and annealing of NiAl film on Ni substrate, Appl. Surf. Sci. 355 (2015) 1145–1152. https://doi.org/10.1016/j.apsusc.2015.07.208.

[58]   S.P. Kiselev, E. V. Zhirov, Molecular-dynamics simulation of the synthesis of intermetallic Ti-Al, Intermetallics. 49 (2014) 106–114. https://doi.org/10.1016/j.intermet.2014.01.008.

[59] S. Shao, H.M. Zbib, I.N. Mastorakos, D.F. Bahr, Deformation mechanisms, size effects, and strain hardening in nanoscale metallic multilayers under nanoindentation, J. Appl. Phys. 112 (2012). https://doi.org/10.1063/1.4748149.

[60] S.D. Chen, Y.K. Zhou, A.K. Soh, Molecular dynamics simulations of mechanical properties for Cu(0 0 1)/Ni(0 0 1) twist boundaries, Comput. Mater. Sci. 61 (2012) 239–242. https://doi.org/10.1016/j.commatsci.2012.04.035.

[61] X.W. Zhou, J.A. Zimmerman, E.D. Reedy, N.R. Moody, Molecular dynamics simulation based cohesive surface representation of mixed mode fracture, Mech. Mater. 40 (2008) 832–845. https://doi.org/10.1016/j.mechmat.2008.05.001.

[62] R.G. Hoagland, J.P. Hirth, A. Misra, On the role of weak interfaces in blocking slip in nanoscale layered composites, Philos. Mag. 86 (2006) 3537–3558. https://doi.org/10.1080/14786430600669790.

[63] N. Abdolrahim, H.M. Zbib, D.F. Bahr, Multiscale modeling and simulation of deformation in nanoscale metallic multilayer systems, Int. J. Plast. 52 (2014) 33–50. https://doi.org/10.1016/j.ijplas.2013.04.002.

[64] J. Wang, R.F. Zhang, C.Z. Zhou, I.J. Beyerlein, A. Misra, Interface dislocation patterns and dislocation nucleation in face-centered-cubic and body-centered-cubic bicrystal interfaces, Int. J. Plast. 53 (2014) 40–55. https://doi.org/10.1016/j.ijplas.2013.07.002.

[65] Y. Chen, S. Shao, X.Y. Liu, S.K. Yadav, N. Li, N. Mara, J. Wang, Misfit dislocation patterns of Mg-Nb interfaces, Acta Mater. 126 (2017) 552–563. https://doi.org/10.1016/j.actamat.2016.12.041.

[66] V. Vítek, Intrinsic stacking faults in body-centred cubic crystals, Philos. Mag. 18 (1968) 773–786. https://doi.org/10.1080/14786436808227500.

[67] V. Vitek, THEORY OF THE CORE STRUCTURES OF DISLOCATIONS IN BODY-CENTERED-CUBIC METALS, Cryst Lattice Defects. 5 (1974) 1–34.

[68] A.P. Gerlich, L. Yue, P.F. Mendez, H. Zhang, Plastic deformation of nanocrystalline aluminum at high temperatures and strain rate, Acta Mater. 58 (2010) 2176–2185. https://doi.org/10.1016/j.actamat.2009.12.003.

[69] P. Gupta, N. Yedla, Strain Rate and Temperature Effects on the Strength and Dissipative Mechanisms in Al-Cu50Zr50 Interface Model: Molecular Dynamics Simulation Study, Procedia Eng. 184 (2017) 631–636. https://doi.org/10.1016/j.proeng.2017.04.128.

[70] A. Dutta, Compressive deformation of Fe nanopillar at high strain rate: Modalities of dislocation dynamics, Acta Mater. 125 (2017) 219–230. https://doi.org/10.1016/j.actamat.2016.11.062.

[71] M. Yaghoobi, G.Z. Voyiadjis, The effects of temperature and strain rate in fcc and bcc metals during extreme deformation rates, Acta Mater. 151 (2018) 1–10.

https://doi.org/10.1016/j.actamat.2018.03.029.

[72]   G. Sainath, B.K. Choudhary, T. Jayakumar, Molecular dynamics simulation
        studies on the size dependent tensile deformation and fracture behaviour of body
        centred cubic iron nanowires, Comput. Mater. Sci. 104 (2015) 76–83.
        https://doi.org/10.1016/j.commatsci.2015.03.053.

[73]   G. Sainath, B.K. Choudhary, Molecular dynamics simulations on size dependent
        tensile deformation behaviour of [110] oriented body centred cubic iron
        nanowires, Mater. Sci. Eng. A. 640 (2015) 98–105.
        https://doi.org/10.1016/j.msea.2015.05.084.

[74]   G. Sainath, B.K. Choudhary, Orientation dependent deformation behaviour of
        BCC iron nanowires, Comput. Mater. Sci. 111 (2016) 406–415.
        https://doi.org/10.1016/j.commatsci.2015.09.055.

[75]   M. Tang, J. Marian, Temperature and high strain rate dependence of tensile
        deformation behavior in single-crystal iron from dislocation dynamics
        simulations, Acta Mater. 70 (2014) 123–129.
        https://doi.org/10.1016/j.actamat.2014.02.013.

[76]   R.F. Smith, J.H. Eggert, R.E. Rudd, D.C. Swift, C.A. Bolme, G.W. Collins, High
        strain-rate plastic flow in Al and Fe, J. Appl. Phys. 110 (2011).
        https://doi.org/10.1063/1.3670001.

[77]   B.A. Remington, P. Allen, E.M. Bringa, J. Hawreliak, D. Ho, K.T. Lorenz, H.
        Lorenzana, J.M. McNaney, M.A. Meyers, S.W. Pollaine, K. Rosolankova, B.
        Sadik, M.S. Schneider, D. Swift, J. Wark, B. Yaakobi, Material dynamics under
        extreme conditions of pressure and strain rate, Mater. Sci. Technol. 22 (2006)
        474–488. https://doi.org/10.1179/174328406X91069.

[78]   T. De Rességuier, M. Hallouin, Stress relaxation and precursor decay in laser
        shock-loaded iron, J. Appl. Phys. 84 (1998) 1932–1938.
        https://doi.org/10.1063/1.368322.

[79]   R. Becker, A. Arsenlis, G. Hommes, J. Marian, M. Rhee, L.H. Yang, A tantalum
        strength model using a multiscale approach : version 2, Livermore, CA, 2009.

[80]   H. Shu, X. Huang, H. Pan, J. Ye, F. Zhang, G. Jia, Z. Fang, Y. Tu, Z. Xie, S. Fu,
        Plastic behavior of steel and iron in high strain rate regime, Int. J. Fract. 206
        (2017) 81–93. https://doi.org/10.1007/s10704-017-0202-6.

[81]   R.W. Armstrong, W. Arnold, F.J. Zerilli, Dislocation mechanics of copper and
        iron in high rate deformation tests, J. Appl. Phys. 105 (2009) 1–8.
        https://doi.org/10.1063/1.3067764.

[82]   R.T. Howe, R.S. Muller, K.J. Gabriel, W.S.N. Trimmer, Silicon
        Micromechanics: Sensors and actuators on a chip, IEEE Spectr. 27 (1990) 29–35.

[83]   K.J. Gabriel, Engineering microscopic machines, Sci. Am. 273 (1995) 150–153.

[84]   T. Çağin, J. Che, M.N. Gardos, A. Fijany, W.A. Goddard, Simulation and experiments on friction and wear of diamond: A material for MEMS and NEMS application, Nanotechnology. 10 (1999) 278–284. https://doi.org/10.1088/0957-4484/10/3/310.

[85]   A.K. Bhattacharya, W.D. Nix, Analysis of elastic and plastic deformation associated with indentation testing of thin films on substrates, Int. J. Solids Struct. 24 (1988) 1287–1298. https://doi.org/10.1016/0020-7683(88)90091-1.

[86]   A.K. Bhattacharya, W.D. Nix, Finite element simulation of indentation experiments, Int. J. Solids Struct. 24 (1988) 881–891. https://doi.org/10.1016/0020-7683(88)90039-X.

[87]   M.F. Doerner, D.S. Gardner, W.D. Nix, Plastic properties of thin films on substrates as measured by submicron indentation hardness and substrate curvature techniques, J. Mater. Res. 1 (1986) 845–851. https://doi.org/10.1557/JMR.1986.0845.

[88]   B. Bhushan, X. Li, Nanomechanical characterisation of solid surfaces and thin films, Int. Mater. Rev. 48 (2003) 125–164. https://doi.org/10.1179/095066003225010227.

[89]   B. Bhushan, A. V. Kulkarni, W. Bonin, J.T. Wyrobek, Nanoindentation and picoindentation measurements using a capacitive transducer system in atomic force microscopy, Philos. Mag. A Phys. Condens. Matter, Struct. Defects Mech. Prop. 74 (1996) 1117–1128. https://doi.org/10.1080/01418619608239712.

[90]   B. Bhushan, V.N. Koinkar, Nanoindentation hardness measurements using atomic force microscopy, Appl. Phys. Lett. 64 (1994) 1653–1655. https://doi.org/10.1063/1.111949.

[91]   A.Y. Nikonov, I.S. Konovalenko, A.I. Dmitriev, Molecular dynamics study of lattice rearrangement under mechanically activated diffusion, Phys. Mesomech. 19 (2016) 77–85. https://doi.org/10.1134/S1029959916010082.

[92]   A.I. Dmitriev, E.A. Kolubaev, A.Y. Nikonov, V E Rubstob, S.G. Psakhie, Study patterns of microstructure formation during friction stir welding, Proc. XLII Int. Summer Sch. APM 2014. (2014) 10–16.

[93]   M. Zaenudin, A.H. Abd Gaffar, M.N. Mohammed, M.A.M. Ali, O. Ismael Al-Sanjary, S. Al-Zubaidi, Study the Effect of Temperature on the Diffusion Bonding of Cu-Al by Using Molecular Dynamics Simulation, 2019 IEEE Int. Conf. Autom. Control Intell. Syst. I2CACIS 2019 - Proc. (2019) 345–348. https://doi.org/10.1109/I2CACIS.2019.8825068.

[94]   M. Zaenudin, M.N. Mohammed, S. Al-Zubaidi, Atomistic Investigation on Diffusion Bonding between Al and Ni using Molecular Dynamics Simulation, ICSGRC 2019 - 2019 IEEE 10th Control Syst. Grad. Res. Colloquium, Proceeding. (2019) 213–218. https://doi.org/10.1109/ICSGRC.2019.8837051.

[95] B. Crossland, A.S. Bahrani, Fundamentals, of explosive welding, Contemp. Phys. 9 (1968) 71–87. https://doi.org/10.1080/00107516808204394.

[96] D. Kim, H. Badarinarayan, J.H. Kim, C. Kim, K. Okamoto, R.H. Wagoner, K. Chung, Numerical simulation of friction stir butt welding process for AA5083-H18 sheets, Eur. J. Mech. A/Solids. 29 (2010) 204–215. https://doi.org/10.1016/j.euromechsol.2009.10.006.

[97] G. Buffa, L. Fratini, R. Shivpuri, CDRX modelling in friction stir welding of AA7075-T6 aluminum alloy: Analytical approaches, J. Mater. Process. Technol. 191 (2007) 356–359. https://doi.org/10.1016/j.jmatprotec.2007.03.033.

[98] I.S. Konovalenko, S.G. Psakhie, Molecular dynamics modeling of bonding two materials by atomic scale friction stir welding at different process parameters, in: AIP Conf. Proc., 2017: pp. 1–5. https://doi.org/10.1063/1.5013774.

[99] I.S. Konovalenko, I.S. Konovalenko, S.G. Psakhie, Molecular dynamics modeling of bonding two materials by atomic scale friction stir welding, in: AIP Conf. Proc., 2017: pp. 1–5. https://doi.org/10.1063/1.5013773.

[100] I. Konovalenko, I. Konovalenko, A. Dmitriev, S. Psakhie, E. Kolubaev, Mass transfer at atomic scale in md simulation of friction stir welding, Key Eng. Mater. 683 (2016) 626–631. https://doi.org/10.4028/www.scientific.net/KEM.683.626.

[101] O. Kayode, O.A. Olufayo, E.T. Akinlabi, Preliminary studies on molecular dynamics simulation of friction stir processing of aluminium alloys, Key Eng. Mater. 796 (2019) 155–163. https://doi.org/10.4028/www.scientific.net/KEM.796.155.

[102] S. Plimpton, A. Thompson, S. Moore, A. Kohlmeyer, R. Berger, LAMMPS Molecular Dynamics Simulator, (2001). https://lammps.sandia.gov/index.html.

[103] Efunda, Efunda: The ultimate online reference for engineers, (n.d.). www.efunda.com.

[104] Y. Morisada, H. Fujii, Y. Kawahito, K. Nakata, M. Tanaka, Three-dimensional visualization of material flow during friction stir welding by two pairs of X-ray transmission systems, Scr. Mater. 65 (2011) 1085–1088. https://doi.org/10.1016/j.scriptamat.2011.09.021.

[105] M.M. Atabaki, M. Nikodinovski, P. Chenier, R. Kovacevic, Welding of aluminum alloys to steels: an overview, 2013.

[106] A.H. Ammouri, A.H. Kheireddine, G.T. Kridli, R.F. Hamade, FEM OPTIMIZATION OF PROCESS PARAMETERS AND IN-PROCESS COOLING IN THE FRICTION STIR PROCESSING OF MAGNESIUM ALLOY AZ31B, in: IMECE2013, San Diego, California, USA, 2013.

[107] R. Kohlhaas, P. Dunner, N. Schmitz-Pranghe, Uber die temperaturabhangigkeit der gitterparameter von eisen, kobalt und nickel im bereich hoher temperaturen,

Zeitschrift Fur Angew. Phys. 23 (1967) 245–249.

[108] W. Witt, Absolute Präzisionsbestimmung von Gitterkonstanten an Germanium-und Aluminium-Einkristallen mit Elektroneninterferenzen, Zeitschrift Fur Naturforsch. - Sect. A J. Phys. Sci. 22 (1967) 92–95. https://doi.org/10.1515/zna-1967-0115.

[109] I.N. Mastorakos, A. Bellou, D.F. Bahr, H.M. Zbib, Size-dependent strength in nanolaminate metallic systems, J. Mater. Res. 26 (2011) 1179–1187. https://doi.org/10.1557/jmr.2011.120.

[110] M.I. Mendelev, D.J. Srolovitz, G.J. Ackland, S. Han, Effect of Fe segregation on the migration of a non-symmetric ∑5 tilt grain boundary in Al, J. Mater. Res. 20 (2005) 208–218. https://doi.org/10.1557/JMR.2005.0024.

[111] J. Vallin, M. Mongy, K. Salama, O. Beckman, Elastic constants of aluminum, J. Appl. Phys. 35 (1964) 1825–1826. https://doi.org/10.1063/1.1713749.

[112] E. Goens, E. Schmid, Elastische Untersuchungen an Eisen-Einkristallen, Zeitschrift Für Elektrochemie Und Angew. Phys. Chemie. 37 (1931) 539–540.

[113] Z.G. El Chlouk, M.A. Shehadeh, R.F. Hamade, The Effect of Strain Rate and Temperature on the Mechanical Behavior of Al/Fe Interface Under Compressive Loading, Metall. Mater. Trans. A Phys. Metall. Mater. Sci. (2020). https://doi.org/10.1007/s11661-020-05709-0.

[114] R.F. Zhang, J. Wang, I.J. Beyerlein, T.C. Germann, Dislocation nucleation mechanisms from fcc/bcc incoherent interfaces, Scr. Mater. 65 (2011) 1022–1025. https://doi.org/10.1016/j.scriptamat.2011.09.008.

[115] W. Yang, G. Ayoub, I. Salehinia, B. Mansoor, H. Zbib, Deformation mechanisms in Ti/TiN multilayer under compressive loading, Acta Mater. 122 (2017) 99–108. https://doi.org/10.1016/j.actamat.2016.09.039.

[116] I. Salehinia, S. Shao, J. Wang, H.M. Zbib, Plastic Deformation of Metal/Ceramic Nanolayered Composites, Jom. 66 (2014) 2078–2085. https://doi.org/10.1007/s11837-014-1132-7.

[117] M.S. Talaei, N. Nouri, S. Ziaei-Rad, Grain boundary effects on nanoindentation of Fe bicrystal using molecular dynamic, Mech. Mater. 102 (2016) 97–107. https://doi.org/10.1016/j.mechmat.2016.08.016.

[118] L. Kubin, Dislocations, Mesoscale Simulations and Plastic Flow, OUP Oxford, Oxford, 2013.

[119] M.M.W. Dogge, R.H.J. Peerlings, M.G.D. Geers, Interface modeling in continuum dislocation transport, Mech. Mater. 88 (2015) 30–43. https://doi.org/10.1016/j.mechmat.2015.04.007.

[120] M.R. Gilbert, P. Schuck, B. Sadigh, J. Marian, Free energy generalization of the

Peierls potential in iron, Phys. Rev. Lett. 111 (2013) 1–5. https://doi.org/10.1103/PhysRevLett.111.095502.

[121] K. Kang, V. V. Bulatov, W. Cai, Singular orientations and faceted motion of dislocations in body-centered cubic crystals, Proc. Natl. Acad. Sci. U. S. A. 109 (2012) 15174–15178. https://doi.org/10.1073/pnas.1206079109.

[122] Z.M. Chen, M. Mrovec, P. Gumbsch, Atomistic aspects of 〈1 1 1〉 screw dislocation behavior in α-iron and the derivation of microscopic yield criterion, Model. Simul. Mater. Sci. Eng. 21 (2013). https://doi.org/10.1088/0965-0393/21/5/055023.

[123] C. Domain, G. Monnet, Simulation of screw dislocation motion in tron by molecular dynamics simulations, Phys. Rev. Lett. 95 (2005) 16–19. https://doi.org/10.1103/PhysRevLett.95.215506.

[124] M.R. Gilbert, S. Queyreau, J. Marian, Stress and temperature dependence of screw dislocation mobility in α-Fe by molecular dynamics, Phys. Rev. B - Condens. Matter Mater. Phys. 84 (2011) 1–11. https://doi.org/10.1103/PhysRevB.84.174103.

[125] D. Caillard, On the stress discrepancy at low-temperatures in pure iron, Acta Mater. 62 (2014) 267–275. https://doi.org/10.1016/j.actamat.2013.10.007.

[126] R.W. Armstrong, S.M. Walley, High strain rate properties of metals and alloys, Int. Mater. Rev. 53 (2008) 105–128. https://doi.org/10.1179/174328008X277795.

[127] B. Gurrutxaga-Lerma, D.S. Balint, D. Dini, D.E. Eakins, A.P. Sutton, Attenuation of the dynamic yield point of shocked aluminum using elastodynamic simulations of dislocation dynamics, Phys. Rev. Lett. 114 (2015) 1–5. https://doi.org/10.1103/PhysRevLett.114.174301.

[128] J.P. Hirth, Theory of dislocations, 2nd ed., Wiley, 1982.

[129] J.P. Hirth, H.M. Zbib, J. Lothe, Forces on high velocity dislocations, Model. Simul. Mater. Sci. Eng. Sci. Eng. 6 (1998) 165–169.

[130] C.H. Zhang, S. Huang, J. Shen, N.X. Chen, Structural and mechanical properties of Fe-Al compounds: An atomistic study by EAM simulation, Intermetallics. 52 (2014) 86–91. https://doi.org/10.1016/j.intermet.2014.04.002.

[131] Z. El Chlouk, W. Kassem, M. Shehadeh, R.F. Hamade, On the mechanical response and formation of FeAl intermetallic compound: Molecular Dynamics Analyses, Philos. Mag. Unpublishe (2020).

[132] S. Queyreau, J. Marian, M.R. Gilbert, B.D. Wirth, Edge dislocation mobilities in bcc Fe obtained by molecular dynamics, Phys. Rev. B - Condens. Matter Mater. Phys. 84 (2011) 1–7. https://doi.org/10.1103/PhysRevB.84.064106.

[133] L. Liu, Q. Deng, M. Su, M. An, R. Wang, Strain rate and temperature effects on

tensile behavior of Ti/Al multilayered nanowire: A molecular dynamics study, Superlattices Microstruct. 135 (2019) 106272. https://doi.org/10.1016/j.spmi.2019.106272.

[134] T. Zhu, J. Li, A. Samanta, A. Leach, K. Gall, Temperature and strain-rate dependence of surface dislocation nucleation, Phys. Rev. Lett. 100 (2008) 1–4. https://doi.org/10.1103/PhysRevLett.100.025502.

[135] D. Caillard, J.L. Martin, Thermally Activated Mechanisms in Crystal Plasticity, 1st ed., Elsevier Science, 2003.

[136] R.W. Armstrong, Q. Li, Dislocation Mechanics of High-Rate Deformations, Metall. Mater. Trans. A Phys. Metall. Mater. Sci. 46 (2015) 4438–4453. https://doi.org/10.1007/s11661-015-2779-6.

[137] J.W. Swegle, D.E. Grady, Shock viscosity and the prediction of shock wave rise times, J. Appl. Phys. 58 (1985) 692–701. https://doi.org/10.1063/1.336184.

[138] J.C. Crowhurst, M.R. Armstrong, K.B. Knight, J.M. Zaug, E.M. Behymer, Invariance of the dissipative action at ultrahigh strain rates above the strong shock threshold, Phys. Rev. Lett. 107 (2011) 1–5. https://doi.org/10.1103/PhysRevLett.107.144302.

[139] F.J. Zerilli, R.W. Armstrong, Dislocation-mechanics-based constitutive relations for material dynamics calculations, J. Appl. Phys. 61 (1987) 1816–1825. https://doi.org/10.1063/1.338024.

[140] G.T. Gray, S.R. Chen, W. Wright, M.F. Lopez, Constitutive equations for annealed metals under compression at high strain rates and high temperatures, New Mex. Los Alamos Natl. Lab. (1994) 21–28.